ROTORDYNAMIC PERFORMANCE OF A ROTOR SUPPORTED ON BUMP-TYPE FOIL BEARINGS: EXPERIMENTS AND PREDICTIONS

A Thesis

by

DARIO RUBIO TABARES

Submitted to the Office of Graduate Studies of
Texas A&M University
in partial fulfillment of the requirements for the degree of

MASTER OF SCIENCE

May 2006

Major Subject: Mechanical Engineering

ROTORDYNAMIC PERFORMANCE OF A ROTOR SUPPORTED ON BUMP-TYPE FOIL BEARINGS: EXPERIMENTS AND PREDICTIONS

A Thesis

by

DARIO RUBIO TABARES

Submitted to the Office of Graduate Studies of
Texas A&M University
in partial fulfillment of the requirements for the degree of

MASTER OF SCIENCE

Approved by:

Chair of Committee,	Luis San Andrés
Committee Members,	Dara Childs
	Othon Rediniotis
Head of Department,	Dennis O'Neal

May 2006

Major Subject: Mechanical Engineering

ABSTRACT

Rotordynamic Performance of a Rotor Supported on Bump-Type
Foil Bearings: Experiments and Predictions. (May 2006)
Dario Rubio Tabares, B.S., Universidad Simón Bolívar
Chair of Advisory Committee: Dr. Luis San Andrés

Gas foil bearings (*GFB*) appear to satisfy most requirements for oil-free turbomachinery, i.e. relatively simple in construction, ensuring low drag friction and reliable high speed operation. However, *GFB*s have a limited load capacity and minimal amounts of damping. A test rig for the rotordynamic evaluation of gas foil bearings was constructed. A DC router motor, 25 krpm max speed, drives a 1.02 kg hollow rotor supported on two bump-type foil gas bearings ($L = D = 38.10$ mm). Measurements of the test rotor dynamic response were conducted for increasing mass imbalance conditions. Typical waterfalls of rotor coast down response from 25 krpm to rest evidence the onset and disappearance of severe subsynchronous motions with whirl frequencies at ~ 50% of rotor speed, roughly coinciding with the (rigid mode) natural frequencies of the rotor-bearing system. The amplitudes of motion, synchronous and subsynchronous, increase (non) linearly with respect to the imbalance displacements. The rotor motions are rather large; yet, the foil bearings, by virtue of their inherent flexibility, prevented the catastrophic failure of the test rotor. Tests at the top shaft speed, 25 krpm, did not excite subsynchronous motions. In the experiments, the subsynchronous motion speed range is well confined to shaft speeds ranging from 22 krpm to 12 krpm. The experimental results show the severity of subsynchronous motions is related to the amount of imbalance in the rotor. Surprisingly enough, external air pressurization on one side of the foil bearings acted to reduce the amplitudes of motion while the rotor crossed its critical speeds. An air-film hovering effect may have enhanced the sliding of the bumps thus increasing the bearings' damping action. The tests also demonstrate that increasing the gas feed pressure ameliorates the amplitudes of subsynchronous motions due to the axial flow retarding the circumferential flow velocity development. A finite element rotordynamic analysis models the test rotor and uses predicted bearing force coefficients from the static equilibrium *GFB* load analysis. The rotordynamic analysis predicts critical speeds at ~8 krpm and ~9 krpm, which correlate well with test critical speeds. Predictions of rotordynamic stability are calculated for the test speed range (0 to 25 krpm), showing unstable operation for the rotor/bearing system starting at 12 krpm and higher. Predictions and experimental results show good agreement in terms of critical speed correlation, and moderate displacement amplitude discrepancies for some imbalance conditions. Post-test inspection of the rotor evidenced sustained wear at the locations in contact with the bearings' axial edges. However, the foil bearings are almost in pristine condition; except for top foil coating wear at the bearing edges and along the direction of applied static load.

DEDICATION

To mom and dad,
for the love, dedication and guidance in every aspect of my life
To my sisters, my beautiful nieces and brother in law,
for being an inspiration to accomplish my goals
To my close friends,
for the great and unforgettable moments during the past two years
To my alma mater, Universidad Simon Bolivar, and my home country, Venezuela
for providing me with the tools to succeed in my professional career

ACKNOWLEDGMENTS

I sincerely thank Dr. Luis San Andrés for his guidance, technical support and financial contribution along the course of this research project. Thanks to Dr. Dara Childs and Dr. Othon Rediniotis for their participation and interests on my research work. I also acknowledge the assistance of Mr. Eddy Denk. Thanks to Taeho Kim for his participation on the experimental and analytical work on this project. The great technical support from my friends, Adolfo Delgado, Juan Carlos Rivadeneira, Arun Surayanaranan and Zach Zutevarn, is very much appreciated. Sincere thanks to Jose Garcia, Justin Allen and Anthony Breedlove for their assistance in setting up the experimental facility. This material is based upon work supported by the National Science Foundation under Grant 0322925. I also acknowledge the support of the TAMU Turbomachinery Research Consortium (TRC).

TABLE OF CONTENTS

Page

ABSTRACT……………………………………………………………… iii

DEDICATION…………………………………………………………… v

ACKNOWLEDGMENTS…………………………………………………... vi

TABLE OF CONTENTS…………………………………………………… vii

LIST OF FIGURES………………………………………………………. x

LIST OF TABLES……………………………………………………….. xvii

NOMENCLATURE……………………………………………………… xviii

CHAPTER I. INTRODUCTION……………………………………….... 1

CHAPTER II. LITERATURE REVIEW ON GAS FOIL BEARINGS STRUCTURAL PARAMETERS AND ROTORDYNAMIC PERFORMANCE….. 5

CHAPTER III. DESCRIPTION OF TEST FOIL BEARINGS AND EXPERIMENTAL ROTOR/BEARING FACILITY……………………….. 15

- Description of Test Foil Bearings…………………………………… 15
- Description of Experimental Facility……………………………….. 17
- Nominal Imbalance Condition of Test Rotor……………………….. 24

CHAPTER IV. ROTORDYNAMIC PERFORMANCE OF A ROTOR SUPPORTED ON THE TEST FOIL GAS BEARINGS – EXPERIMENTAL RESULTS…………………………………………………………….... 30

- Estimation of Clearance in Foil Bearings and Static Load Distribution in Test Foil Bearings…………………………………………………… 30
- Imbalance Response Tests…………………………………………... 35
- Rotor/Bearing System (Non) Linearity……………………………... 44
- Waterfall Analysis of Coastdown Rotor Responses………………… 47
- Rotor Motion Orbits at Various Shaft Speeds………………………. 52
- Effect of Air Pressurization on Imbalance Response and System Stability… 55
- Time for Rotor to Coastdown……………………………………….. 61

Page

Damping Ratios………………………………………………………….. 62

CHAPTER V. ROTORDYNAMIC ANALYSIS OF TEST ROTOR SUPPORTED ON GAS FOIL BEARINGS – PREDICTIONS VERSUS EXPERIMENTAL RESULTS……………………………………………………………………… 65

Predicted Bearing Performance…………………………………………... 65
Journal Eccentricity and Attitude Angle…………………………………. 68
Predicted Bearing Force Coefficients…………………………………….. 72
Predicted Rotor/Bearing Performance……………………………………. 75
Damped Natural Frequencies and Damping Ratios……………………… 79
Response to Imbalance: Comparison between Predictions and Experimental Results…………………………………………………………………. 82

CHAPTER VI. TEST FOIL BEARING AND ROTOR SURFACE CONDITIONS. 85

CHAPTER VII. CONCLUSIONS……………………………………………….. 90

REFERENCES………………………………………………………………… 93

APPENDIX A. IDENTIFICATION OF FB STRUCTURAL DYNAMIC COEFFICIENTS FROM RAP TESTS ON ROTOR…………………………….. 98

APPENDIX B. ELECTROMAGNETIC LOAD ACTUATOR DESCRIPTION….. 102

APPENDIX C. WATERFALL PLOTS OF BASELINE ROTOR RESPONSE AT THE FREE END, HORIZONTAL AND VERTICAL DIRECTIONS…………….. 105

APPENDIX D. SYNCHRONOUS AND DIRECT ROTOR RESPONSES FOR IMBALANCE DISPLACEMENTS A2, B1 AND B3…………………………… 107

APPENDIX E. SYNCHRONOUS RESPONSE AND PHASE ANGLE FOR IMBALANCE TESTS A IN THE VERTICAL DIRECTION AT THE DRIVE AND FREE ROTOR ENDS……………………………………………………… 110

APPENDIX F. SYNCHRONOUS RESPONSE AND PHASE ANGLE FOR TESTS B IN THE HORIZONTAL DIRECTION AT THE DRIVE AND FREE ROTOR ENDS………………………………………………………………… 112

APPENDIX G. AXIAL BEARING FLOW PARAMETER CALCULATION……. 114

Page

APPENDIX H. BENDING MODE SHAPES OF TEST ROTOR ALONE AND TEST ROTOR WITH THE CONNECTING SHAFT………………………………. 116

APPENDIX I. DEFLECTED ROTOR SHAPES AT SELECTED SHAFT SPEEDS FOR THE LARGEST IMBALANCE MASS CONFIGURATION……… 118

APPENDIX J. COMPARISON BETWEEN EXPERIMENTAL AND PREDICTED RESPONSE TO IMBALANCE FOR IMBALANCE TEST A2 AND B2…………………………………………………………………….... 121

VITA………………………………………………………………………… 123

LIST OF FIGURES

FIGURE Page

I-1 Schematic representation of a bump-type gas foil bearing……………….. 1

III-1 Test bump type foil bearings……………………………………….…..... 16

III-2 Detailed view of test foil bearing components…………………………...... 17

III-3 Test Rig for rotordynamic experiments of rotor supported on FBs……….. 19

III-4 Geometry of test rotor (0.98 kg, 2.12 lb)……………………………….. 20

III-5 Test rotor and test foil bearings for rotordynamic tests…………………… 20

III-6 Miniature flexible coupling geometry and specifications. Source: R+W Coupling website. http://www.rw-couplings.com...................................... 22

III-7 Picture of the instrumentation rack used for FB testing…………………… 24

III-8 Data acquisition system for measurement and recording of rotor vibration, applied electromagnet force and rotor speed………………………………. 25

III-9 Correction weight magnitudes and angular positions at the balancing planes……………………………………………………………………. 26

III-10 Amplitude of direct displacement response of rotor baseline condition for air supply pressure at 34.4 kPa [5 psig]………………………………… 27

III-11 Amplitude of synchronous displacement responses of the rotor baseline condition for air supply pressure at 34.4 kPa [5 psig]……………………... 27

III-12 Waterfall plot of baseline rotor coastdown at drive end, horizontal plane (X_{DE}). Air pressure at 34.4 kPa [5 psig]………………………………… 28

III-13 Waterfall plot of baseline rotor coastdown at drive end, vertical plane (Y_{DE}). Air pressure at 34.4 kPa [5 psig]…………………………………. 29

IV-1 Rotor displacement at the free end and drive end bearings for increasing applied electromagnetic loads…………………………………………...… 31

FIGURE Page

IV-2 Schematic view of acting forces on test rotor for static conditions……….. 32

IV-3 Effect of coupling load on the reacting bearing loads…………………….... 33

IV-4 Schematic view of coupling deflection when connecting motor………….. 33

IV-5 Schematic view of the imbalance mass location for Test A and B………... 36

IV-6 Direct and synchronous coastdown response for an imbalance displacement of u = 7.4 μm (in phase, Test A1). Air pressure at 34.4 kPa [5 psig]…………………………………………………………………... 38

IV-7 Direct and synchronous coastdown response without baseline subtraction for an imbalance displacement of u = 10.5 μm (in phase, Test A3). Air pressure at 34.4 kPa [5 psig]……………………………………………. 39

IV-8 Direct and synchronous coastdown response without baseline subtraction for an imbalance displacement of u = 5.2 μm (out of phase, test B2). Air pressure at 34.4 kPa [5 psig]……………………………………………. 41

IV-9 Synchronous rotor response amplitude with baseline subtraction and phase angle for imbalance tests A. Air pressure at 34.4 kPa [5 psig]. Measurements taken at drive end, horizontal direction (X_{DE})……………... 42

IV-10 Synchronous rotor response amplitude with baseline subtraction and phase angle for imbalance tests A. Air pressure at 34.4 kPa [5 psig]. Measurements taken at free end, horizontal direction (X_{FE})……………… 42

IV-11 Synchronous rotor response amplitude and phase angle for imbalance tests B. Air pressure at 34.4 kPa [5 psig]. Measurements taken at drive end, vertical direction (Y_{DE})…………………………………………….. 43

IV-12 Synchronous rotor response amplitude and phase angle for imbalance tests B. Air pressure at 34.4 kPa [5 psig]. Measurements taken at free end, vertical direction (Y_{FE})………………………………………………...…… 43

IV-13 Amplitude ratio (AR) of rotor synchronous response at the measurement planes for in-phase imbalance conditions. (Remnant imbalance response subtracted)……………………………………………………………. 45

FIGURE Page

IV-14 Amplitude ratio (*AR*) of rotor synchronous response at the measurement planes for out-of-phase imbalance conditions. (Remnant imbalance response subtracted)………………………………………………….. 46

IV-15 Waterfall plot of coastdown response for imbalance displacement u = 7.4 μm (in phase, Test A1). Air pressure at 34.4 kPa [5 psig] and measurements at rotor free end, vertical plane (Y_{FE})……………………… 48

IV-16 Filtered components of synchronous and subsynchronous vibrations and whirl frequency ratio for imbalance displacement u = 7.4 μm (in phase, test A1). Air pressure at 34.4 kPa [5 psig] and measurements at rotor free end, vertical plane (Y_{FE})………………………………………………… 48

IV-17 Waterfall plot of coastdown response for imbalance displacement u = 10.5 μm (in phase, test A3). Air pressure at 34.4 kPa [5 psig] and measurements at rotor free end, vertical plane (Y_{FE})……………………… 49

IV-18 Filtered components of synchronous and subsynchronous vibrations and whirl frequency ratio for imbalance displacement u = 10.5 μm (in phase, test A3). Air pressure at 34.4 kPa [5 psig] and measurements at rotor free end, vertical plane (Y_{FE}) …………………………………………………... 49

IV-19 Waterfall plot of coastdown response for imbalance displacement u = 7.4 μm (out of phase, test B2). Air pressure at 34.4 kPa [5 psig] and measurements at rotor free end, vertical plane (Y_{FE})……………………… 50

IV-20 Filtered components of synchronous and subsynchronous vibrations and whirl frequency ratio for imbalance displacement u = 7.4 μm (out of phase, test B2). Air pressure at 34.4 kPa [5 psig] and measurements at rotor free end, vertical plane (Y_{FE})……………………………………… 50

IV-21 Subsynchronous amplitudes and frequencies of occurrence for imbalance u = 10.5 μm (in phase) and u = 7.4 μm (out of phase)…………………….. 51

IV-22 Synchronous and direct motion orbits at the drive and free rotor ends for an imbalance u = 10.5 μm (in phase). A) Rotor speed 3.8 krpm, B) 8.2 krpm and C) 16.7 krpm………………………………………………… 53

IV-23 Synchronous and direct motion orbits at the drive and free rotor ends for an imbalance u = 7.4 μm (out of phase). A) Rotor speed 4.7 krpm, B) 9.1 krpm and C) 16.4 krpm………………………………………………… 54

FIGURE Page

IV-24 Synchronous vibrations at 8.4 krpm for increasing air supply pressures. Measurements taken at the four eddy current sensors……………………... 56

IV-25 Synchronous vibrations at 15.2 krpm for increasing air supply pressures. Measurements taken at the four eddy current sensors……………………... 56

IV-26 Schematic representation of air axial flow through test foil bearings……... 57

IV-27 FFTs of steady state time responses at 15,200 rpm for three increasing air supply pressures; 40.8 kPa, 204 kPa and 340 kPa. Measurements taken at the drive end, horizontal direction (X_{DE})………………………………... 58

IV-28 FFTs of steady state time responses at 15,200 rpm for three increasing air supply pressures; 40.8 kPa, 204 kPa and 340 kPa. Measurements taken at the drive end, vertical direction (Y_{DE})……………………………..…. 60

IV-29 Coastdown speed versus time for rotor baseline condition and increasing air feed pressures. Logarithmic scale……………………………………… 61

IV-30 Notation for estimating system viscous damping ratio using the Q factor method…………………………………………………………………....... 64

V-1 Coordinate systems for analysis of gas foil bearing performance………… 66

V-2 Predicted journal eccentricity ratios versus rotational speed. Drive end FB static load = 4.2 N and free end FB static load = 4.5 N…………………… 69

V-3 Predicted attitude angle versus rotational speed. Drive end FB static load = 4.2 N and free end FB static load = 4.5 N……………………………….. 69

V-4 Predicted minimum film thickness versus a percent of the measured drive end bearing clearance (c = 50 μm). Load fixed at 4.2 N…………………... 70

V-5 Predicted drag torque versus a percent of the measured drive end bearing clearance (c = 50 μm). Load fixed at 4.2 N……………………………….. 71

V-6 Predicted synchronous stiffness coefficients for free end foil bearing. Radial clearance of 45 μm and static load 4.5 N…………………………... 72

V-7 Predicted synchronous stiffness coefficients for drive end foil bearing. Radial clearance of 50 μm and static load 4.2 N…………………………... 73

FIGURE Page

V-8 Predicted synchronous damping force coefficients for free end foil bearing. Radial clearance of 45 μm and static load 4.5 N………………… 74

V-9 Predicted synchronous damping force coefficients for drive end foil bearing. Radial clearance of 50 μm and static load 4.2 N………………… 74

V-10 Finite element model of test rotor (with connecting shaft and flexible coupling included)……………………………………………………… 76

V-11 Measured and predicted free-free mode shapes of test rotor with the connecting shaft and flexible coupling…………………………………….. 78

V-12 Undamped critical speed map of the test rotor with the connecting shaft and flexible coupling……………………………………………………. 79

V-13 Damped natural frequency map of the FB rotor/bearing system………….. 80

V-14 Predicted rotordynamic stability map of the FB rotor/bearing system……. 81

V-15 Predicted and experimental response to imbalance at the drive end and free end location for an imbalance displacement of u = 10.5 μm (in phase, Test A3)……………………………………………………………. 83

V-16 Predicted and experimental response to imbalance at the drive end and free end location for an imbalance displacement of u = 7.4 μm (out-of-phase, Test B3)…………………………………………………………….. 84

VI-1 Test rotor surface condition before and after rotordynamic experiments…. 86

VI-2 Test foil bearing surface condition after rotordynamic experiments……… 87

A1 Time dependant impact force and rotor displacements for load excitations at the A) center of gravity and B) the motor end………………………….. 99

A2 Impact forces, A) at the rotor center of gravity and B) at the motor end, and calculated C) rotor center of gravity displacement and D) angular deflections varying with frequencies………………………………………. 100

A3 Identified stiffness and damping coefficients versus frequency………….... 100

B1 Schematic view of the electromagnetic actuator installed on the test rig…. 102

FIGURE Page

C1 Waterfall plot of baseline rotor response at free end, horizontal location (X_{FE}). Air pressure at 34.4 kPa [5 psig]…………………………………… 105

C2 Waterfall plot of baseline rotor response at the free end, vertical location (Y_{FE}). Air pressure at 34.4 kPa [5 psig]……………………………………. 106

D1 Direct and synchronous rotor response for an imbalance u = 9.5 μm (in phase, Test A2). Air pressure at 34.4 kPa [5 psig]……………………….. 107

D2 Direct and synchronous rotor response for an imbalance u = 3.7 μm (out of phase, Test B1). Air pressure at 34.4 kPa [5 psig]…………………….. 108

D3 Direct and synchronous rotor response for an imbalance u = 7.4 μm (out of phase, Test B3). Air pressure at 34.4 kPa [5 psig]…………………….. 109

E1 Synchronous rotor response and phase angle for imbalance tests A (in phase). Air pressure at 34.4 kPa [5 psig]. Measurements taken at drive end, vertical direction (Y_{DE}). With baseline subtractions………………….. 110

E2 Synchronous rotor response and phase angle for imbalance tests A (in phase). Air pressure at 34.4 kPa [5 psig]. Measurements taken at free end, vertical direction (Y_{FE}). With baseline subtractions……………………….. 111

F1 Synchronous rotor response and phase angle for imbalance tests B (out of phase) Air pressure at 34.4 kPa [5 psig]. Measurements taken at drive end horizontal direction (X_{DE}). With baseline subtractions……………………. 112

F2 Synchronous rotor response and phase angle for imbalance tests B (out of phase). Air pressure at 34.4 kPa [5 psig]. Measurements taken at free end horizontal direction (X_{FE}). With baseline subtractions…………………….. 113

H1 Measured and predicted free-free mode shapes of test rotor without the connecting shaft and flexible coupling…………………………………….. 116

H2 Measured and predicted free-free mode shapes of test rotor with connecting shaft (no flexible coupling)……………………………………. 117

I1 Deflected shapes of test rotor with connecting shaft and flexible rotor at 5,000 rpm and 7,000 rpm for an in-phase imbalance of u = 10.7 μm……... 118

I2 Deflected shapes of test rotor with connecting shaft and flexible rotor at 9,000 rpm and 15,000 rpm for an in-phase imbalance of u = 10.7 μm…… 119

FIGURE Page

I3 Deflected shapes of test rotor with connecting shaft and flexible rotor at 25,000 rpm for an in-phase imbalance of u = 10.7 μm…………………… 120

J1 Predicted and experimental response to imbalance at the drive end and free end location for an imbalance of u = 9.5 μm (in phase, test A2)……... 121

J2 Predicted and experimental response to imbalance at the drive end and free end location for an imbalance of u = 5.2 μm (out-of-phase, test B2).... 122

LIST OF TABLES

TABLE Page

II-1 List of references on experimental investigations on FB rotordynamic performance and major findings………………………………………… 9

III-1 Nominal dimensions and parameters of test bump foil bearings………... 18

III-2 Summary of rotor geometry characteristics and inertia properties……… 21

III-3 Instrumentation installed in the FB test rig for electromagnet calibration and rotordynamic experiments……………………………………….... 23

IV-1 Estimated radial clearances and static loads for test foil bearings……… 34

IV-2 Imbalance mass magnitudes and locations………………………………. 36

IV-3 Calculated mass flow rate, mean velocity and Reynolds number for the axial bearing flow……………………………………………………….... 59

IV-4 Damping ratios of rotor/bearing system obtained from synchronous coastdown responses…………………………………………………….. 63

V-1 Geometry for analysis of gas bearing performance……………………... 67

V-2 Operating conditions for analysis of gas bearing performance………….. 67

V-3 Measured and predicted bending mode frequencies…………………….. 77

VI-1 Test rotor and bump foil material properties…………………………….. 85

VI-2 Test foil bearing diameters before and after the measurements…………. 87

VI-3 Test rotor diameters before and after the measurements………………… 88

VI-4 Calculated radial clearances based on the final diameters of the test rotor and foil bearings………………………………………………………. 89

A1 Identified FB parameters from linear and exponential curve fit of rotor transient response…………………………………………………….... 101

B1 Electromagnet material properties, physical dimensions and main characteristics…………………………………………………………… 103

NOMENCLATURE

A	Axial coupling length [mm]
c	Radial clearance [μm]
c	Estimated foil bearing radial clearance [μm]
C_{EQ}	Equivalent viscous damping [N-s/m]
c_{nom}	Nominal foil bearing radial clearance [μm]
C_{xx}, C_{yy}	Direct synchronous damping coefficients along the X and Y coordinated [kN/m]
C_{xy}, C_{yx}	Cross-coupled synchronous damping coefficients along the X and Y coordinated [kN/m]
D	Bearing inner diameter [mm]
D_j	Journal diameter [mm]
E	Bump modulus of elasticity [Pa]
f	Excitation frequency [Hz]
F_C	Coupling static force [N]
$F_{DE,}$ F_{FE}	Static bearing force at the drive end and free end bearing [N]
h	Bump height [mm]
h_{min}	Minimum film thickness [μm]
ID	Inner diameter of FB [mm]
I_P	Polar moment of inertia [kg/m^2]
I_T	Transverse rotor moment of inertia [kg/m^2]
K	Dimensional stiffness
K_C	Coupling lateral stiffness [MN/m]
$K_{F,}$ K_W	Free ends and free end -fixed end bump stiffnesses per unit area [N/m^3]
K_{xx}, K_{yy}	Direct synchronous stiffness coefficients along the X and Y coordinated [MN/m]
K_{xy}, K_{yx}	Cross-coupled synchronous stiffness coefficients along the X and Y coordinated [MN/m]

L	Axial bearing length [mm]
l_o	Bump length [mm]
L_S	Bearing span distance [mm]
L_T	Rotor total length [mm]
m	Imbalance mass [kg]
$\dot{m}_z$	$\dot{m}_z = \dot{M}_z \cdot \pi \cdot D$, Total axial flow rate [kg/s]
M, M_B	Rotor mass and bearing mass [kg]
$\dot{M}_z$	$\dot{M}_z = \frac{c^3}{24 \cdot \mu_V \cdot R_g \cdot T} \frac{\left(P_s^2 - P_a^2\right)}{L}$, Mass flow rate per bearing circumferential length [kg/m.s]
N_1, N_2	Rotational Speed at 0.707 of the amplitude at the critical speed [rpm]
N_B	Number of bumps
N_n	Critical speed [rpm]
OD	Outer FB diameter [mm]
p	Bump pitch [mm]
P_a	Ambient pressure, 1.01 bar
P_s	Supply pressure [Pa]
Q	Q factor, $Q = \frac{N_n}{N_2 - N_1}$
R	Bearing radius [mm]
r_e	Radius for insertion of imbalance mass [mm]
Re_A	$Re_A = \frac{\dot{M}_z}{\mu_V}$, Axial flow Reynolds Number
Re_C	$Re_A = \frac{\rho \cdot \Omega \cdot R \cdot c}{\mu_V}$, Circumferential flow Reynolds Number
Re_C^*	$Re_C^* = Re_C \frac{c}{R}$, Modified Reynolds Number
R_g	Gas constant [J/kg.K]

t	Foil thickness [mm]
T	Temperature across the bearing axial length [K]
t_f	Foil thickness [mm]
u	Imbalance displacement [μm]
V_z	Flow velocity across the axial bearing length [m/s]
W	Rotor weight [N]
w	$w = \frac{W_n}{P_a \cdot L \cdot D}$, Load coefficient
W_n	Bearing load [N]
X, Y	Horizontal and vertical rotor displacements
x_G	Distance between the rotor CG to the free end [mm]
z	Damping ratio
κ	$\kappa = \frac{K}{E(T) \cdot t}$. FB dimensionless stiffness coefficient
Λ	$\Lambda = \frac{6\mu\Omega}{P_a}\left(\frac{R}{C}\right)^2$. Bearing speed number
ΔP	Pressure drop across the bearing axial length [kPa]
Ω	Rotational speed [rpm]
δ_C	Coupling lateral deflection [μm]
ε	Eccentricity [μm]
ϕ	Angle of imbalance mass insertion [deg]
$\phi D_{1,2}$	Flexible coupling bore diameters [mm]
γ	Structural loss factor
φ	Attitude angle [deg]
μ	Dry friction coefficient
μ_v	Gas viscosity [c-Poise]
θ	Pad angular coordinate [deg]
ρ	Rotor density [kg/m^3]
ρ_E	Electromagnet density [kg/m^3]

υ	Poisson's ratio

Subscript

DE	Drive end
FE	Free end

CHAPTER I

INTRODUCTION

High performance oil-free turbomachinery implements gas foil bearings *(GFB*s*)* to improve mechanical efficiency in compact units. *GFBs* fulfill most of the requirements of novel oil-free turbomachinery by increasing tenfold their reliability in comparison to rolling elements bearings, for example [1]. Foil bearings are made of one or more compliant surfaces of corrugated metal and one or more layers of top foil surfaces. The compliant surface, providing structural stiffness, comes in several configurations such as bump-type (see Figure I-1), leaf-type and tape-type, among others. *GFB*s operate with nominal film thicknesses larger than those found in a geometrically identical rigid surface bearing, for example, since the hydrodynamic film pressure generated by rotor spinning "pushes" the *GFB* compliant surface [2, 3].

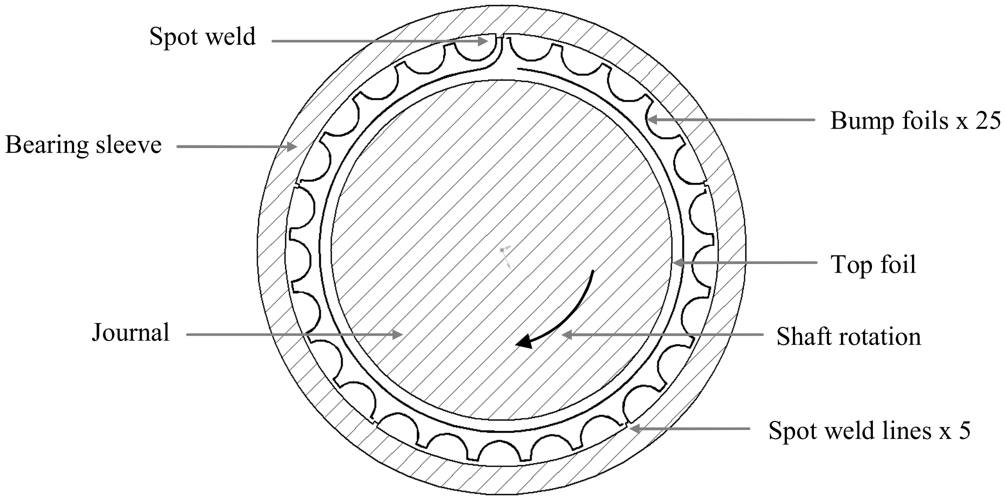

Figure I-1 Schematic representation of a bump-type gas foil bearing

---

This thesis follows the style of the Journal of Engineering for Gas Turbines and Power.

*GFB*s enable high speed operation and large load capacity; in particular in third generation configurations [4] the underlying compliant structure provides a tunable structural stiffness [5 - 8]. In *GFB*s, Coulomb type damping arises due to the relative motion between the bumps and the top foil, and between the bumps and the bearing support wall [9, 10].

In bump-type foil bearings, the top foil supported by compliant bumps, deforms elastically under the pressure field created by the hydrodynamic film. The bearing stiffness combines that resulting from the deflection of the bumps and also by the hydrodynamic film generated when the shaft rotates. Damping arises due to the relative motion between the bumps and the top foil or between the bumps and the bearing wall, i.e. Coulomb type damping [5]. The gas foil bearing design constrains the direction of shaft rotation to only one direction. Due to the hydrodynamic film created by rotor spinning, the top foil expands resulting in a larger film thickness than in a rigid bearing, for example. At start up, the back of the foil is in contact with the bump foils and the outer side of the foil is in contact with the journal. As the rotor spins to a sufficiently high speed (i.e. when lift off occurs), the top foil contracts as air is dragged into a thin annular film between the foil and the shaft.

Gas foil bearings have been applied successfully to a wide range of high-speed rotating machinery such as air cycle machines (ACMs), auxiliary power units (APUs), and cryogenic turbocompressors, among others [11]. Field experience with gas foil bearing commenced in the mid 60’s by introducing the first production air cycle machines (ACM) using foil gas bearings [1]. The air cycle machines are the heart of the environmental control system (ECM) used in aircraft to control cooling, heating and pressurization of aircraft. These units, developed for the DC-10 ECM, proved to be far more reliable than previous ball bearing units. Further research and experimentations continued in the 70’s to increase load capacity and damping capability. Based on the successful performance, ACMs for other aircraft such as in the EMB-120, ATR-42 and Boeing 767/757, started to implement foil gas bearings. For instance, the foil bearing air cycle machine on the 747 aircraft demonstrated a mean time between failures (MTBF) in excess of 100,000 hours. Recently, the latest ECS system for the Boeing aircraft 777 uses a four-wheel foil gas bearing ACM. This unit has passed 36,000 start-stop cycles, which is equivalent to 30 years life of the machine.

For over three decades gas foil bearings have been successfully applied in ACMs used for aircraft cabin pressurization. These turbomachines utilize "Generation I" gas foil bearings along with conventional polymer solid lubricant [12]. Based on the technical and commercial success of ACMs; oil-free technology moves into gas turbine engines. The first commercially available Oil-free gas turbine was the 30 kW Capstone microturbine conceived as a power plant for hybrid turbine electric automotive propulsion system [12]. This microturbine utilizes patented foil gas bearings categorized as "Generation III" bearings. In addition, future applications of oil-free turbomachinery using foil bearing include large Regional Jet engines and supersonic Business Jet engines. For these applications, the system benefits include, among others, weight and maintenance reduction.

Remarkable improvements in high temperature limits are obtained by using coatings (solid lubricants). Process gases can operate at very high temperatures without chemically breaking down as opposed to conventional lubricant oils. In addition, oil lubricants lead to larger power losses due to friction at the interface between the fluid and bearing shell. Having established good reliability records in many high-speed turbomachinery at extreme temperatures, *GFBs* show great credentials to replace ball bearings in cryogenic fluid turbomachinery [13]. Applications of gas foil bearing in process fluid turbocompressors have been also noted in the open literature. Chen et al. [14] present an application example of the successful replacement of a tape-type foil bearing with a bump-type foil bearing in a helium turbocompressor. Both bearing types are described, as are the steps involved in the design and fabrication of the foil bump bearing, and results of a comparison in performance tests for the original and replacement foil bearings. Methods to analyze bump-type foil bearing with commercially available software are reviewed to further emphasize the inherent simplicity of *GFBs*. The frictional torque of foil bearings is greater when the rotor starts up and decreases when the rotor speed is high enough to generate a hydrodynamic film. The same characteristic is observed from the coastdown response of the rotor. Steady state and speed transient tests show that the implementation of the bump-type foil bearing increased the critical speed of the original system because the bearing stiffness is likely to be greater than that of the previous design (tape-type foil bearings).

Despite the level of progress advanced in recent years, foil bearing design is still largely empirical due to its mechanical complexity. As part of the current research on gas foil bearing at Texas A&M University, this report provides an experimental investigation of the rotordynamic performance of a light rotor supported on two bump-type gas foil bearings. The results serve as benchmark for calibration of analytical tools under development at TAMU.

CHAPTER II

LITERATURE REVIEW ON GAS FOIL BEARINGS STRUCTURAL PARAMETERS AND ROTORDYNAMIC PERFORMANCE

This chapter presents a review of technical publications related to foil bearings (*FB*), detailing the most relevant findings obtained in each of the studies. An extensive part of the literature on foil gas bearings relates to their structural characteristics, namely structural stiffness, dry friction coefficient and equivalent viscous damping. The compliant structural elements in *FB*s constitute the most significant aspect on their design process. With proper selection of foil and bump materials and geometrical parameters, the desired stiffness, damping and friction forces can be achieved. Ku and Heshmat [5] first developed a theoretical model of the corrugated foil strip deformation used in foil bearings. The model introduces local interaction forces, the friction force between the bump foils and the bearing housing or top foil, and the effect of bump geometry on the foil strip compliance. Theoretical results under constant and variable (triangular) load distribution profiles indicate that bumps located at the fixed end of a foil strip provide higher stiffness than those located at its free end. Higher friction coefficients tend to increase bump stiffness and may lock-up bumps near the fixed end. Similarly, the bump thickness has a small effect on the local bump stiffness, but reducing the bump pitch or height significantly increases the local bump stiffness.

In a follow-up paper, Ku and Heshmat [6] present an experimental procedure to investigate the foil strip deflection under static loads. Identified bump stiffnesses in terms of bump geometrical parameters and friction coefficients corroborate the theoretical results presented in [5]. Through an optical track system, bump deflection images are captured indicating that the horizontal deflection of the segment between bumps is negligible compared to the transversal deflection of the bumps. The identification of bump strip stiffness, from the load-versus-deflection curves, indicates that the existence of friction forces between the sliding surfaces causes the local stiffness to be dependant on the applied load and ensuing deformation.

Rubio and San Andrés [8] further develop the structural stiffness dependency on applied load and displacement. An experimental and analytical procedure aims to identify the structural stiffness for an entire bump-type foil bearing. A simple static loader set up allows observing the *FB* deflections under various static loads. Three shafts of increasing diameter induce a degree of preload into the *FB* structure. Static measurements show nonlinear *FB* deflections, varying with the orientation of the load relative to the foil spot weld. Loading and unloading tests evidence hysteresis. The *FB* structural stiffness increases as the bumps-foil radial deflection increases (hardening effect). The assembly preload results in notable stiffness changes, in particular for small loads. A simple analytical model assembles individual bump stiffnesses and renders predictions for the *FB* structural stiffness as a function of the bump geometry and material, dry-friction coefficient, load orientation, clearance and preload. The model predicts well the test data, including the hardening effect. The uncertainty in the actual clearance (gap) upon assembly of a shaft into a *FB* affects most the predictions.

Similarly, Ku [15] describes an experimental investigation to characterize the structural dynamic force coefficients of corrugated bumps used in foil bearings. Dynamic force perturbations are imposed to a six-bump strip under different test conditions and various bump geometrical configurations. Test results show that dynamic structural stiffnesses decrease with the amplitude of motion and increase with the static load. The friction coefficient for various surface coatings are determined empirically by matching the values of the dynamic structural stiffness with analytical predictions developed in [5]. The dynamic structural stiffness best correlates with theoretical values when selecting dry friction coefficients ranging from 0.4 to 0.6, depending on the surface coating.

The structural damping mechanism in foil bearings is yet not well known. Various investigations have focused into this *FB* structural characteristic. Heshmat and Ku [16] develop an experimental procedure to identify the structural stiffness and equivalent viscous damping coefficient by exciting, with two electromagnetic shakers, a non-rotating shaft supported on *FB*s. Structural dynamic coefficients, determined from a force equilibrium on the *FB* housing, indicate that the direct stiffness and equivalent viscous damping decrease with increasing dynamic load amplitudes. In addition, an increase in the excitation frequency decreases the direct viscous damping and increases the direct stiffness. An analytical model, advanced in [9, 10], accounting for the bumps curvature effect, force interaction between bumps, and dry friction coefficient under sliding conditions, provides predictions of dynamic force coefficients in foil bearings. The analytical model in [9] determines dynamic structural stiffness based on the perturbation motion of the journal center with respect to its static equilibrium position. Equivalent viscous damping coefficients are extracted from the hysteresis loop area enclosed by the journal center locus undergoing dynamic motions. Dynamic force coefficients are found to be in agreement with experimental results using a constant dry friction coefficient ranging from 0.4 to 0.6 for the model predictions. Also, the identified dynamic force coefficients are anisotropic and highly non linear with respect to the amplitude of displacement perturbation.

Recently, Salehi et. al [17] perform dynamic forced tests on corrugated metal sheets (bump foil strips) affixed within an arcuate surface. Dynamic force excitations are exerted on the bump strip using an electromagnetic shaker at various load and frequency conditions. Equivalent viscous damping coefficients and dry friction forces are extracted from the resulting hysteresis loops (force versus displacement) for various test conditions. In addition, bump foil stiffness and viscous damping coefficients are identified from the complex mechanical impedance formulation using a single degree of freedom model. Experimental results of dynamic force coefficients for the bump strips are used to develop a parametric (dimensionless) relationship between frictional damping and test conditions of load (W_n), amplitude of motion (X) and frequency (f). Based on experimental results, the parametric relationship of viscous damping is found to decrease with increasing frequencies, $C_{EQ} \propto 1/f$, and amplitude of motions, $C_{EQ} \propto 1/X$, while increasing with the magnitude of dynamic load, $C_{EQ} \propto W_n$. In terms of dry friction coefficients (μ), a parametric relationship is also found based on the experimental results. Experimental results of dry friction coefficients render values ranging from 0.1 to 0.4 for increasing excitation frequencies from ~ 0 Hz to ~ 600 Hz. The literature concerned with the rotordynamic characteristics of foil bearings is quite limited. The results achieved in previous works represent important background for the current research project. Table II-1 summarizes the major findings in experimental investigations of foil bearing rotordynamic performance.

Heshmat [18] performed high-speed tests using a journal foil bearing to establish the rotor-bearing stability characteristics and speed performance. Increasing load conditions and large unbalance magnitudes were applied to the test rotor. The rotating system did not evidence harmful synchronous amplitudes due to the increase in the residual unbalance throughout the entire speed range (up to 132,000 rpm). On the other hand, load capacity tests consisted of applying a load to a center bearing at an arbitrary speed until a high-speed rub between the mating surfaces of the shaft and foil occurred. Unlike rigid wall bearings, the foil air bearings exhibited eccentricity displacements (e) larger than their nominal clearance due to the compliance of the bump foils. Precisely, these larger eccentricity displacements lead to significant enhancements on the load capacity coefficient (W_n)[1]. In general, the load capacity coefficients (W_n) and eccentricity displacements (e) present little variance at low values of bearing speed parameter ($\Lambda <$ 1.5)2. After that point, W_n and e rise at a steep rate with an increase in Λ. Experimental data collected from the rotor/bearings system shows relatively large subsynchronous vibration components in comparison to the synchronous component. However, the rotating system reached a limit cycle amplitude and operated safely for a large period of time.

---

[1] Load capacity coefficient defined as $w = W_n / P_a L D$, where W_n is bearing load, P_a is ambient pressure, L and D are bearing length and diameter, respectively.

[2] Bearing speed parameter defined as $\Lambda = 6 \mu_c \Omega R^2 / P_a c^2$, where μ_v is gas viscosity, Ω is rotor speed, R is bearing radius, and C is radial clearance.

Table II-1 List of references on experimental investigations on FB rotordynamic performance and major findings

Authors	Test Apparatus	Type of Rotordynamic Experiments	Observations
1994 Heshmat, H. Ref [18]	Rotor (1.52 kg) supported on foil journal bearings and driven by an integral impulse-type air turbine.	Coastdown tests from 132,000 rpm above first two rigid body mode frequencies.	Major frequencies are subsynchronous vibrations associated to rotor rigid body frequencies (cylindrical and conical). Increasing FB eccentricity displacements, larger than the nominal clearance, lead to significant enhancements on load capacity.
2000 Heshmat, H. Ref [19]	Flexible rotor (3.9 kg) supported on foil journal bearings	Coastdown tests from 45,000 rpm above first two rigid body mode frequencies and first bending mode.	No subsynchronous vibrations experienced until reaching the bending critical speed where rigid body frequencies dominated rotor response.
2001 Howard, S., et. al Ref [20]	Not specified	Steady state tests at 30,000 rpm. Applied bearing load varies from 11 to 89 N and temperature ranges from 25º to 538ºC	Steady-state stiffness does not vary with temperature until the temperature reaches ~538ºC where stiffness drops due to foil material's loss of strength. Effect of temperature on stiffness is larger at high loads than at low loads. No subsynchronous vibrations acknowledged.
2002 Walton, J., and Heshmat, H. Ref [21]	Air cycle machine simulator supported on "third generation" foil journal bearings.	Coastdown tests from 61,000 rpm	Steady state motions at subsynchronous rigid body mode frequencies limited in magnitude. Similar dynamic performance of the rotor system for vertical and horizontal operations.
2002 Swason E., et. al Ref [22]	Rotor (54.5 kg) supported on active magnetic bearings and compliant foil bearings.	Coastdown tests from 16,000 rpm with foil bearing alone.	Heaviest shaft to be supported on foil bearings. Steady state vibrations at subsynchronous rigid body mode frequencies small in magnitude.
2003 Lee, Y.B., et. al Ref [23]	Two-stage centrifugal compressor supported on conventional bump foil journal bearing and viscoelastic foil journal bearing	Steady state tests at compressor operating speed 32,000 rpm	Used first generation FBs, subsynchronous vibrations associated with rigid mode frequencies of the shaft prevailed over the synchronous motions Using viscoelastic layer FBs, subsynchronous motions are reduced.
2004 Hou, Y., et. al Ref [24]	Rotor supported on two foil journal bearing with elastic support	Run-up tests to 151,000 rpm	Subsynchronous vibrations are small compared to synchronous component throughout the whole operating region.

Heshmat [19] also investigates the foil bearing performance in a test rotor operating above its bending critical speed. Free-free rap test on the long test rotor allows identifying the bending natural frequencies and corresponding nodes of the test rotor. Based on the bending-mode nodes, three different locations for the foil bearing pedestal are examined to determine an optimum position for operations above the rotor bending critical speed. Locating the bearing pedestals at the furthest position from the mode nodes allows super bending critical operations of the rotor/bearing system (2.5 times the first bending critical speed). Operation beyond the first bending critical speed presents small synchronous vibration amplitudes throughout entire speed range. However, large subsynchronous components are observed, at the first rigid body mode and its harmonics, when crossing the first bending critical speed. The subsynchronous components reached limit cycle amplitude typical of dry friction damped systems.

DellaCorte and Valco [25] introduce a simple "rule of thumb" method to estimate the load capacity in foil gas journal bearings. The method relates the bearing load capacity to the bearing size and the speed through an empirically based load capacity coefficient, D. Based on previous experiments; DellaCorte and Valco determine that the load capacity is a linear function of the surface velocity and bearing projected area. Three generations of foil bearings are selected to validate this method. First generation foil bearings developed in the 70's reach a load capacity coefficient of $D = 0.4$. However, latest foil bearing designs have an improved load capacity with a D coefficient up to 1.4.

A comprehensive analytical model of the foil bearing rotordynamic performance is essential to reproduce experimental investigations and to assure a proper design and implementation of foil gas bearings in novel turbomachinery applications. Peng and Carpino [26] develop a finite difference formulation, coupling hydrodynamic and elastic foundation effects, to calculate stiffness and damping force coefficients in foil bearings. The model is simply described as impedances in series representing the structural and hydrodynamic support forces. The results from the analytical procedure show that the bearing direct stiffness increases with rotor speed and generally decreases with increased bump compliance. At low rotor speeds, the compliance of the bearing depends primarily on the gas film, which is relatively soft compared to the stiffness of the elastic foundation. In contrast, at high speed operations, the stiffness of the gas film is large compared to the stiffness of the foundation and the compliance of the bearing depends primarily on its elastic foundation. Although these results do not include damping resulting from Coulomb friction, the dynamic force coefficients are significantly reduced due to the elastic foundation in comparison to plain journal bearing coefficients.

San Andrés [27] presents a coupled turbulent bulk-flow and simple structural analysis of a three pad foil bearing for cryogenic fluid applications. The foil structure model consists of a complex structural stiffness with a loss factor, η, denoting hysterical damping, whereas the fluid film contribution is assessed using an isothermal analysis for turbulent bulk-flow of variable liquid properties. The calculated foil bearing force coefficients, namely "viscous" damping and stiffness, show a strong dependency with excitation frequency. The loss factor, η, reduces the direct stiffness coefficients and increases the cross coupled stiffness. A strong effect of the dry friction on the "viscous" damping coefficients at low frequencies is evident while at high frequencies the effect of structural damping is less significant.

The successful integration of foil bearings into oil-free turbomachinery applications must address to higher load capacities and more damping capability. Lee et al. [28, 29] introduce a viscoelastic material to enhance the damping capacity of foil bearings. The rotordynamic characteristics of a conventional foil bearing and a viscoelastic foil bearing are compared in a rotor operating beyond the bending-critical speed. Experimental results for the vibration orbit amplitudes show a considerably reduction at the critical speed by using the viscoelastic foil bearing. Furthermore, the increased damping capability due to the viscoelasticity allows the suppression of nonsynchronous motion for operation beyond the bending critical speed. In term of structural dynamic stiffness, the viscoelastic foil bearings provide similar dynamic stiffness magnitudes in comparison to the conventional foil bearings.

Foil gas bearings require solid lubrication (coatings) to prevent wear and reduce friction at start-up and shut-down prior to the development of the hydrodynamic gas film. Earlier investigations have revealed that with proper selection of solid lubricants the bearing rotordynamic performance can be significantly improved. DellaCorte et al. [30] present an experimental procedure to evaluate the effects of solid lubricants applied to the shaft and top foil surface on the load capacity of a generation III foil gas bearing. The temperature conditions for the load capacity tests ranged from 25°C to 650°C. A baseline coating of PS304 is plasma sprayed to the test shaft while various foil coatings, such as cured polyimide and chatodic arc aluminum bronze, aim to improve friction and wear properties. The PS304 coating is a plasma spray composite made from a power blend of NiCr, Cr_2O_3, Ag, BaF_2/CaF_2. Each constituent in the PS304 performs a unique function; see reference [30] for details. Sacrificial solid lubricants (polyimide, MoS_2), are overcoated to the PS304 shaft coatings in order to provide low friction during low temperature operations while at high temperature they burn away leaving the PS304 as the primary coating. Experimental results show that the best bearing performance (maximum load capacity) is achieved when the foil and the shaft have good solid film lubricant characteristics. The presence of the non-galling PS304 coating on the shaft and Al-Cu on the top foil also enhances the bearing performance. Based on the test results, the best performance upon installation is achieved using an effective sacrificial solid lubricant film such as MoS_2.

FB rotordynamic performance can be also compromised by the selection of the bearing preload. For instance, foil bearings with large preloads are susceptible to excessive thermal effects and high lift-off torques. Whereas *FB*s subjected to small preloads exhibit a decrease in load capacity coefficients [20]. Radil et al. [31] study the effect of radial clearance on the *FB* performance. The authors follow an empirical procedure to estimate the linear region of *FB* structural deflection, and define this overall displacement as the *FB* clearance. This ad-hoc practice does not necessarily provide the actual foil bearing clearance since the *FB* structural deflection is highly nonlinear with respect to the applied static load. In the same paper the authors evaluate the influence of radial clearance on the bearing load capacity coefficient. Two foil bearings are tested at different initial radial clearances, below and above the nominal radial clearance (obtained experimentally). Modification to the radial clearance is accomplished by incrementally reducing the outside diameter of the mating journal using an in-place grinding. The experimental results evidence a strong effect of radial clearance on the foil bearing load capacity coefficients. Both foil bearings exhibit an optimum radial clearance that produced a maximum load capacity coefficient. Based on the experimental results of load capacity versus radial clearance, the authors conclude that relative to the optimum clearance (maximum load capacity) there are two distinct regimes, i.e. heavily and lightly preloaded zones.

To date there are no archival publications showing the experimental identification of the complete set of rotordynamic coefficients in a gas foil bearings. Only Howard et. al [20] forward an experimental procedure to identify steady state direct stiffness in *FB*s operating at elevated temperatures. Cross-coupled stiffness coefficients were not identified in this experimental procedure. The experiments consisted of running the *FB* at constant speed while applying a constant load. Steady-state stiffness coefficients (κ)[3] are found to increase with the applied load and to decrease with shaft speed. Also, steady-state stiffness does not vary with temperature until reaching ~538 ºC, where the stiffness drops due to the foil material loss of mechanical strength.

Howard et. al [32] characterize *FB* dynamic direct stiffness and damping at various temperatures, loads and speed conditions from impact excitations exerted to a test *FB*. A two-degree of freedom system models the ensuing *FB* transient response and compares experimental data to both exponential (viscous damping) and linear (Coulomb damping) decay trends. The method provides a better understanding of the dominating energy dissipation mechanism for all test regions. The identified dynamic stiffness varies as much as 200% with large changes in load and speed. Experimental results also

---

[3] Dimensionless FB stiffness coefficient defined as, $\kappa = K / E(T).t$, where K is the dimensional stiffness, E is the young modulus of the foil material, T is the temperature and t is the foil thickness.

indicate that at high temperatures and low active loads, the gas film is soft compared to the foil structure, i.e. viscous damping behavior. Conversely, for high loads and low temperatures, the bearing behaves like a dry friction damped system with the gas film being stiffer than the foil structure.

CHAPTER III

DESCRIPTION OF TEST FOIL BEARINGS AND EXPERIMENTAL ROTOR/BEARING FACILITY

This chapter describes the test foil bearings and the experimental facilities used for the rotordynamic tests. A detailed overview of the main dimensions and material properties of the test foil bearings are presented as well as the nominal imbalance condition of the test rotor. Also, the test rig facility for rotordynamic experiments is described including its main components such as the drive motors and the electromagnet load actuator. A detailed exposition of the calibration procedure for the electromagnetic load actuator is presented. The test rig described herein is located in the Turbomachinery Laboratory of Texas A&M University.

Description of Test Foil Bearings

Figure I-1 shows a schematic view of a bump-type foil bearing support. The test bump-type foil bearing configuration consists of four bump strips, each with five bumps, aligned axially. The end of a strip is welded to the bearing sleeve while the other end is free. A total of five bump strips are placed around the bearing sleeve, each of them welded at one end and free at the other. The test foil bearings have a total of twenty five bumps around the bearing sleeve. Top foil, coated with a spray-on coating Emralon 333 of thickness 25.4 μm, consists of a thin metal sheet welded at the bearing sleeve at one end (spot weld) and free at the other end.

The test foil bearing design corresponds to a "second generation" foil bearing with stiffness characteristics of the foil structure varying either axially along the bearing length or in the circumferential direction [25]. In the case of the test foil bearing, the structural stiffness characteristics vary in the circumferential orientation as shown by Rubio and San Andrés [8]. However, due to the bump configuration in the axial direction, i.e. bump strips aligned and equally spaced, the structural stiffness does not have significant variations along the bearing axial length. In addition, static load measurements on the test foil bearings show nonlinear deflections, varying strongly with the orientation of the load relative to location of the foil spot weld [8].

In general, the static structural deformation of the top and bump foils depends on the design dimensional parameters, bearing preload magnitudes and test conditions under which the *FB* is excited such as load, frequency, amplitude of vibration, among others. Specifically, for the current test foil bearings, the static structural behavior is well-known from static load versus deflection experiments performed by Rubio and San Andrés [8].

The test *FB*s were acquired from Foster-Miller Technologies in 2002. The *FB* manufacturer numbers are 047 and 043; and hereby referred as *FB1* and *FB2*, respectively. Figure III-1 shows a photograph of the test foil bearing and Figure III-2 portrays a detailed view of the test foil bearing components. Table III-1 below presents the *FBs* main dimensions and geometry characteristics. The free-free and fixed-free bump stiffnesses are estimated using Iordanoff formulae [33].

Figure III-1 Test bump type foil bearings

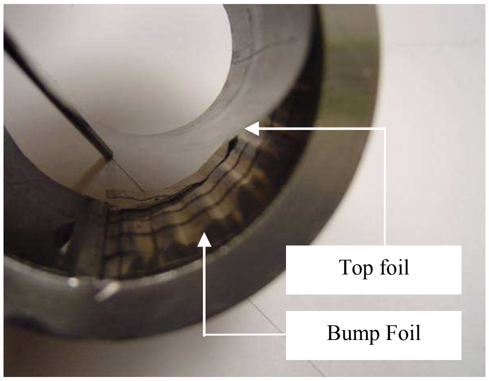

Figure III-2 Detailed view of test foil bearing components

Description of Experimental Facility

Figure III-3 shows the test rig for rotordynamic experiments of a hollow rotor supported on foil gas bearings. The test rig consists of a hollow rotor supported on two bump-type foil bearings. A massive steel housing holds the test foil bearings in place and contains an internal duct to supply air pressure up to 0.70 MPa (100 psig) for cooling the test foil bearings while operating the test rig, if needed. The bearing housing also provides a direct access to the test rotor center location through a wide lateral groove. This feature allows the installation of an electromagnet (EM) load mechanism acting vertically at the test rotor center location. The function of the EM actuator is to apply a non-contacting load to the test rotor. Typical air gaps between EM tip and the test rotor vary from 0.25 mm (10 mil) to 0.50 mm (20 mil). The upper disk on the electromagnet mount allows a controlled vertical movement of the electromagnet to create various air gaps. As described in a later section, the EM actuator consists of a slender shaft made up of a high magnetic permeability material. The resulting non-contacting load originates from various currents passing through copper wires wounded over the magnetic material. The following section of this report details more on the electromagnet load mechanism and its functioning.

The test rotor, made of steel AISI 4140, consists of a hollow shaft of length 209.55 mm [8.25 in] and diameter at the bearing locations of 38.10 mm [1.500 in]. A

TDC (thin dense chrome) coating, of thickness 25.4 μm [0.001 in], is applied to the test rotor surface at the bearing locations to reduce friction and wear at the rotor/foil interface. Figure III-4 shows details of the test rotor and main dimensions and Figure III-5 shows a picture of the test rotor and foil bearings.

Table III-2 presents a summary of the rotor inertia properties and geometry. The motor end has an internal thread to allow a coupling connection to the drive motor. Both rotor drive and free ends have 8 threaded holes where imbalance masses are attached at 15.11 mm (0.595 in) radius.

Table III-1 Nominal dimensions and parameters of test bump foil bearings

Parameters	SI Units	English Units
Inner diameter, D	38.10 mm	1.50 in
Outer diameter, OD	50.80 mm	2.00 in
Axial bearing length, L	38.10 mm	2.00 in
Radial nominal clearance[4], c_{nom}	0.0355 mm	0.0014 in
Number of bumps, N_B	25	
Bump pitch, p	4.572 mm	0.18 in
Bump length, l_o	4.064 mm	0.16 in
Foil thickness, t	0.102 mm	0.004 in
Bump height, h	0.381 mm	0.015 in
Poisson's ratio, υ	0.29	0.29
Bump modulus of elasticity, E	213 GPa	31,000 ksi
Bearing mass, M_B	0.27 kg	0.61 lb
Free-free end bump stiffness[5], K_F	0.526 MN/m	3.04 lb/mil
Free-fixed bump stiffness[5], K_W	0.876 MN/m	5.06 lb/mil

---

[4] Manufacturer nominal clearance for a 38.10 mm [1.500 in] diameter journal

[5] Bump stiffnesses are estimated using Iordanoff formulae [33].

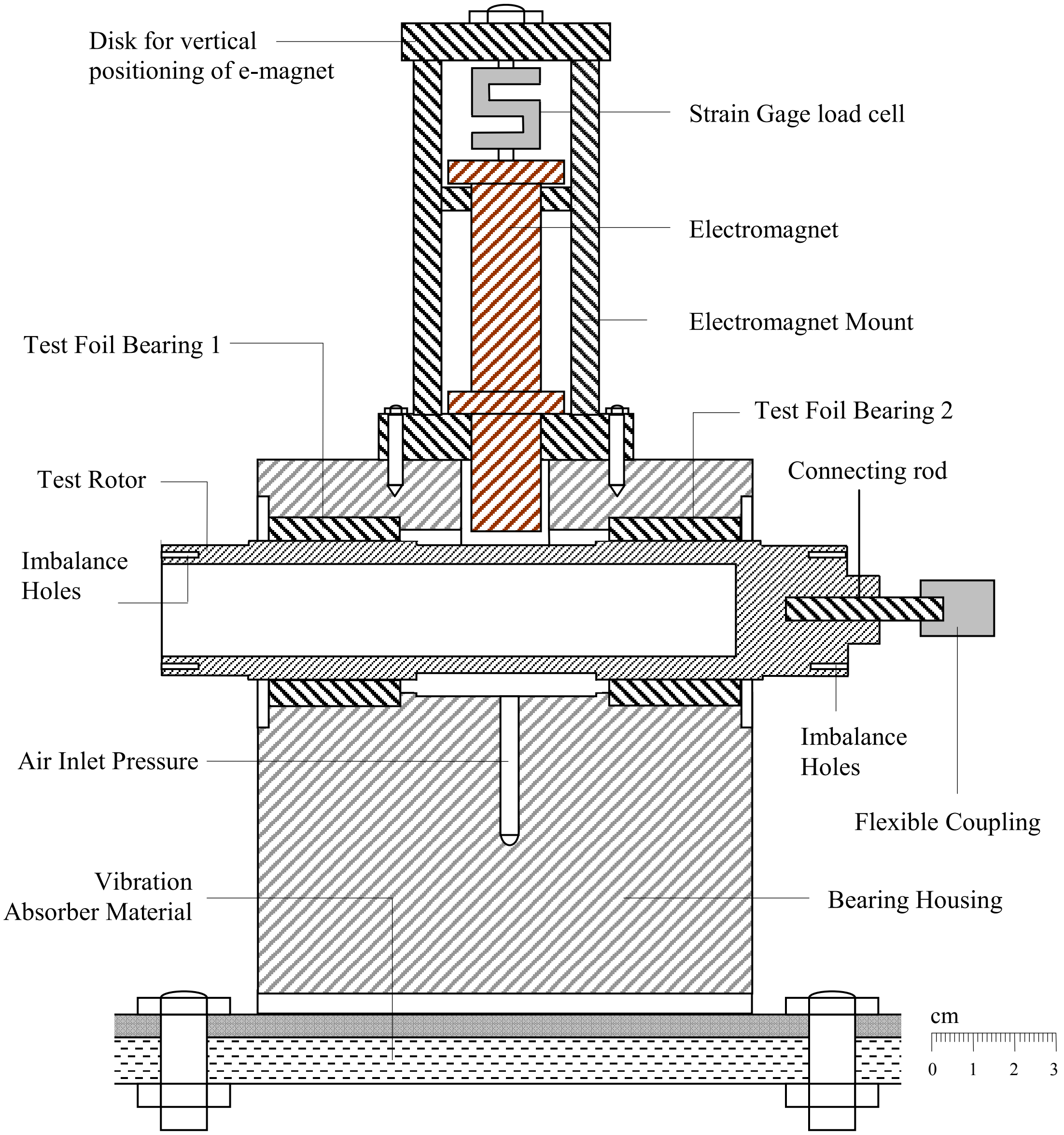

Figure III-3 Test Rig for rotordynamic experiments of rotor supported on FBs

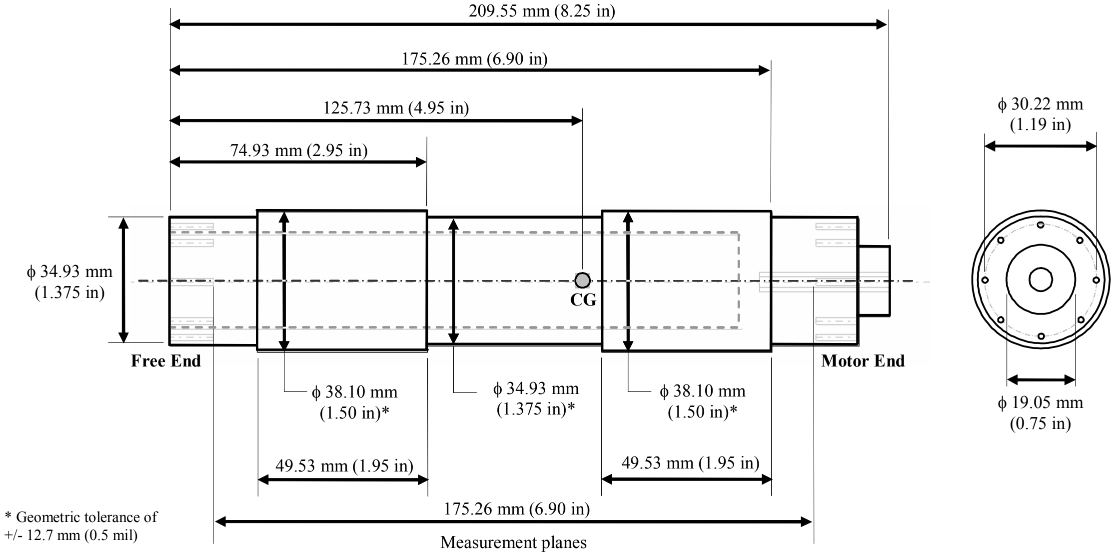

Figure III-4 Geometry of test rotor (0.98 kg, 2.12 lb)

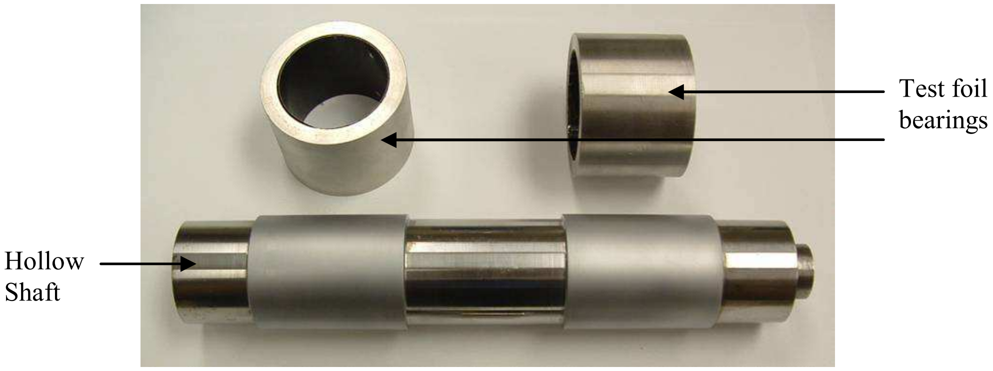

Shaft length = **209.5 mm** Shaft diameter at bearing locations =**38.10mm**

Figure III-5 Test rotor and test foil bearings for rotordynamic tests

Chapter V details the experimental and analytical procedure to determine free-free natural frequencies and modes shapes of the test rotor. On the other hand, rigid body natural frequencies without the connecting shaft and the flexible coupling are estimated through rap tests on the rotor supported on the test foil bearing. Appendix A explains the experimental procedure to estimate the rigid body natural frequencies and to identify structural bearing parameters.

Table III-2 Summary of rotor geometry characteristics and inertia properties

Parameters	SI Units	English Units
Modulus of elasticity E	193 GPa	28,000 ksi
Material density, ρ	7830 kg/m^3	0.282 lb/in^3
Total mass[6], M	0.98 kg	2.2 lb
Diameter at the bearing locations[6], D_j with thin chrome coating	38.20 mm	1.5002 in
Total length[2], L_T	209.55 mm	8.25 in
Distance between bearing locations[6], L_S	100.58 mm	3.95 in
Distance between the rotor CG to the free end, x_G	125.73 mm	4.95 in
Transverse moment of inertia, I_T	3.71 E^{-3} kg.m^2	12.67 lb.in^2
Polar moment of inertia, I_P	2.24 E^{-4} kg.m^2	0.76 lb.in^2

A Router motor, 1.49 kW [2.0 HP], drives the test rotor up to a top speed of 25,000 rpm[7]. The coupling connection for this motor/ test rotor configuration is through a miniature flexible coupling and a connecting shaft, see Figure III-3. The connecting shaft, made of steel AISI 4140, comprises a threaded segment of length 38.1 mm [1.5 in] and a plain segment of length 12.7 mm [0.5 in] and diameter 5.08 mm [0.2 in]. The threaded segment connects with the test rotor while the plain section inserts into the flexible coupling. Figure III-6 shows the single-disc flexible coupling geometry and major specifications.

Measurements of the test rotor displacements are taken with two pairs of eddy current sensors located at the both rotor ends. The eddy current sensors measure vertical and horizontal displacements at the rotor measurement planes; see Figure III-4. Vibration signals from the eddy current sensors connect to a signal conditioner to bias the DC offset levels and then into a commercial data acquisition system for industrial

---

[6] The uncertainties on physical dimensions of the test rotor are within 3%.

[7] Attempts to operate the test rig with an air turbine (max speed 50 krpm) failed due to installation difficulties.

machinery monitoring and diagnostic (Bently Nevada, Adre DAQ system®). Table III-3 summarizes the instrumentation sensors used for the rotordynamic test and the corresponding sensitivities. A two-channel dynamic signal analyzer displays the frequency content of the selected signals, and an analog oscilloscope displays the unfiltered rotor orbits in real time.

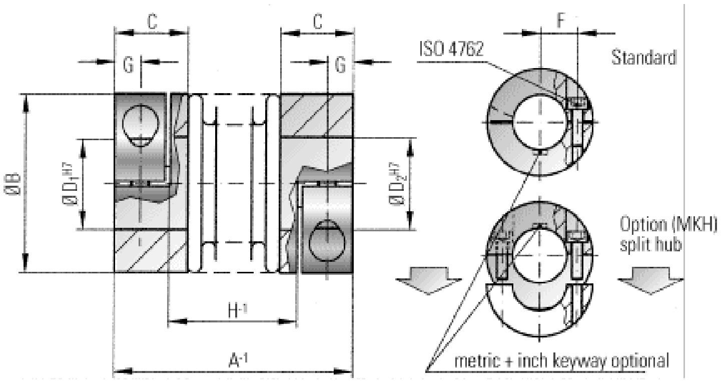

Parameters		SI Units	English Units
Bores, ϕD_1 and ϕD_2		5.08 mm	0.20 in
Axial coupling length, *A*		31.00 mm	1.22 in
Hub length, *C*		9.00 mm	0.35 in
Hub major diameter, ϕ_B		15.00 mm	0.59 in
Transverse moment of inertia		3.0 gr.cm^2	1.02E^{-3} lb.in^2
Weight		9.0 gr	0.31 oz
Torsional stiffness		170 Nm/rad	15.2 lb.in/rad
Lateral stiffness[8]	$\delta_C < 25$ µm	0.163 MN/m	940.9 lb/in
	$\delta_C > 25$ µm	4.5 kN/m	25.9 lb/in
Maximum speed		26,000 rpm	

Figure III-6 Miniature flexible coupling geometry and specifications. Source: R+W Coupling website. http://www.rw-couplings.com

---

[8] Lateral stiffness is experimentally identified by recording the coupling lateral deflection (δ_C) for increasing static loads applied on the coupling. The identified stiffness shows two regions of high and low stiffness depending on the coupling lateral deflection (δ_C), thus showing nonlinearity.

Figure III-7 shows a picture of the instrumentation rack used to monitor and record test data of the test rig. The strain gage force sensor connects the electromagnetic actuator to a fixed vertical-positioning disk, see Figure III-3. Therefore, the strain gage meter readings represent electromagnetic forces acting on the test rotor. An optical sensor aligned along the horizontal direction provides a reference signal for measurement of the phase angle and rotor speed. A personal computer receives the measured signal data and runs the signal processing and analysis software.

Table III-3 Instrumentation installed in the FB test rig for electromagnet calibration and rotordynamic experiments

Measured magnitude	Instrument	Gain
Force, (F_y), vertical	Strain gage sensor	7.04 mV/N (31.0 mV/lb)
Displacement (X_{FE}), Free end horizontal	Eddy current sensor	7.84 mV/micron (199.2 mV/mil)
Displacement (X_{DE}), Drive end horizontal	Eddy current sensor	7.80 mV/micron (198.3 mV/mil)
Displacement (Y_{FE}), Free end vertical	Eddy current sensor	7.48 mV/micron (190.2 mV/mil)
Displacement (Y_{DE}), Drive end vertical	Eddy current sensor	7.88 mV/micron (200.3 mV/mil)

While operating the test rig, the temperatures on the outer surface of the test foil bearings are monitored, as shown in Figure III-8. Also, as a result of the continuous current through the electromagnet cables, heat is generated and temperature on the electromagnet surface rises. A thermocouple monitors the temperature variation on the electromagnet surface. Due to excessive temperature rise on the electromagnet surface a cooling system is implemented to dissipate the generated heat. This is ensured by a series of copper tubes wounded over the electromagnet with cool oil flowing through the tubes. Appendix B details the cooling system for the electromagnet as well as the electromagnet load mechanism and its functioning.

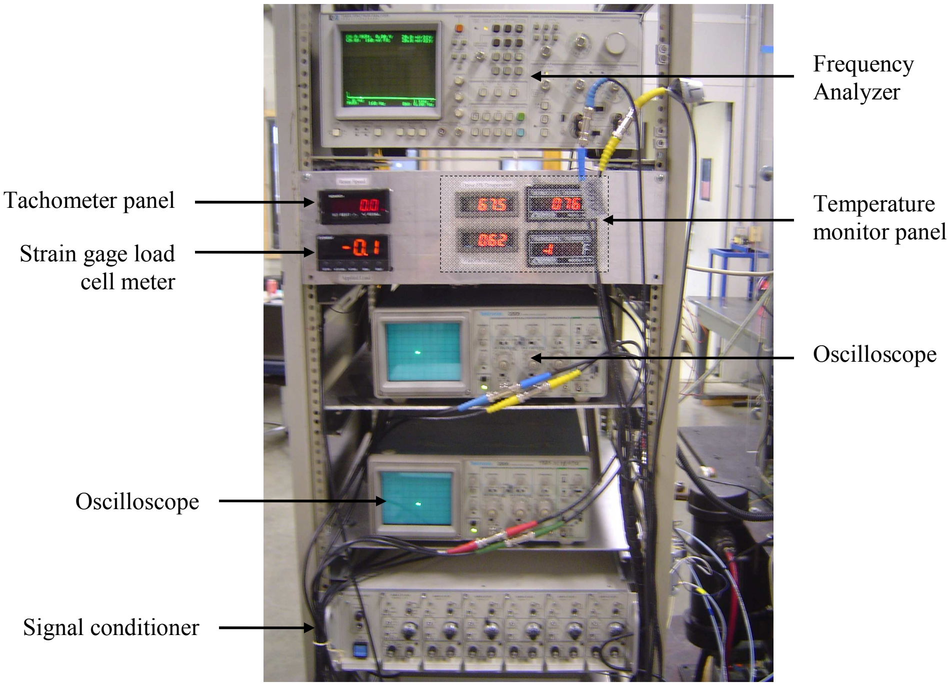

Figure III-7 Picture of the instrumentation rack used for FB testing

Nominal Imbalance Condition of Test Rotor

Rotor balancing is important because it provides a baseline for measurement of rotor response to calibrated imbalance masses. For the test rotor, a standard influence coefficient method for two-plane balancing reduced the original rotor synchronous response to satisfactory small levels of vibration. The selected speed for the balancing procedure is 4,000 rpm, well below the first critical speed at ~ 9,000 rpm. The rotor balancing procedure consists of introducing imbalance masses at the rotor free and motor drive ends. The ensuing synchronous motion vectors (amplitude and phase), vertical and horizontal directions, at the rotor free and drive end are recorded. The imbalance mass and the angle between the trial mass and tachometer position, coinciding with the reflective surface in the rotor, represents the imbalance mass vector. The angles are considered positive against shaft rotation. Once the rotor balancing tests are performed, the influence coefficient method allows determination of correction mass vectors (amplitude and angular location) to balance the test rotor.

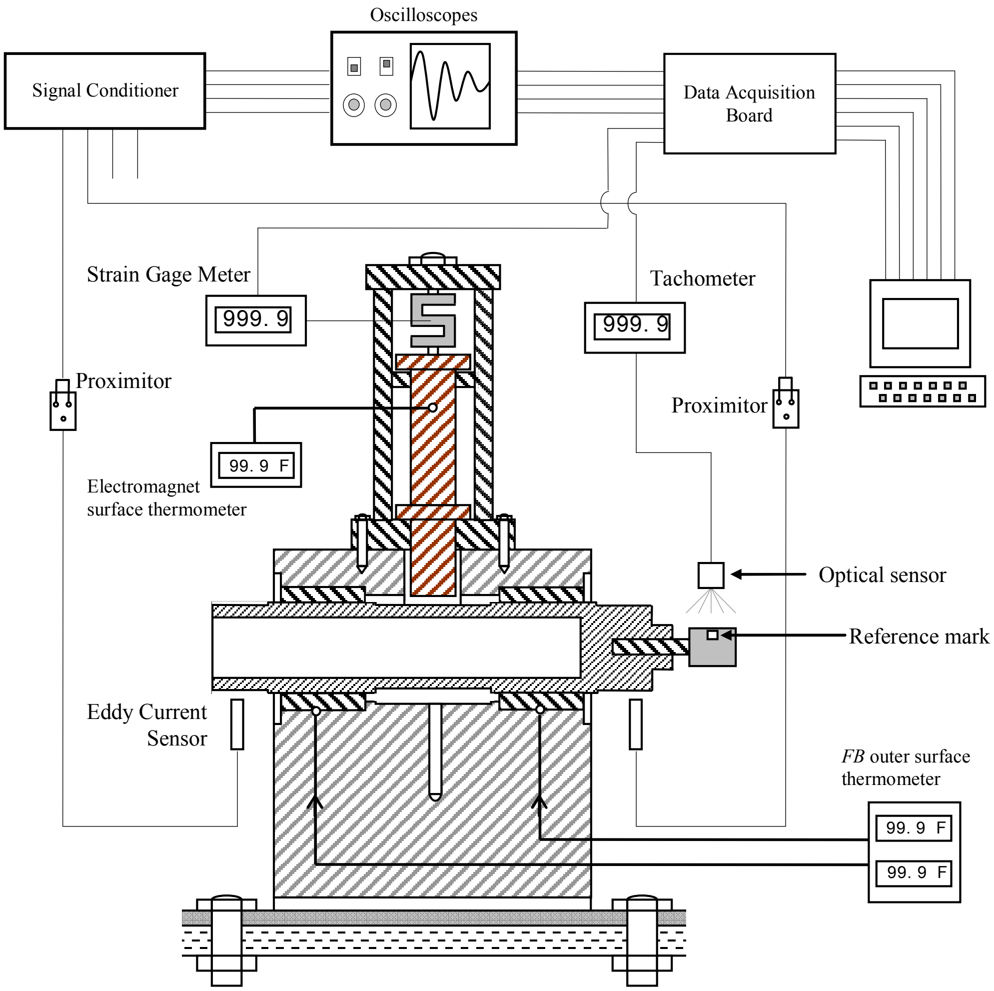

Figure III-8 Data acquisition system for measurement and recording of rotor vibration, applied electromagnet force and rotor speed

Figure **III-9** shows the location and magnitudes of the calculated correction weights at the free and motor end. Once the correction weights are inserted, the test rotor is brought to its maximum speed (25 krpm) and the baseline condition is recorded at the four rotor locations.

Rotor displacement designations are: X_{DE} for horizontal drive end, Y_{DE} for vertical drive end, X_{FE} for horizontal free end, and Y_{FE} for vertical free end.

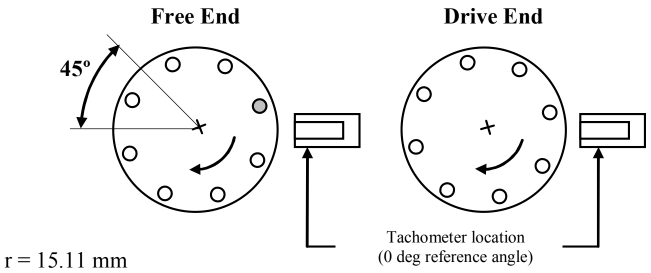

Correction Masses	Drive end	Free end
Distributed correction mass	None	3.62 gr.mm @ 27°

Figure III-9 Correction weight magnitudes and angular positions at the balancing planes

Figure III-10 and Figure III-11 show the amplitudes of the direct and synchronous coastdown displacement responses (zero to peak) of the rotor baseline condition for a supply pressure at the bearing housing midspan of 34.4 kPa [5 psig][9]. The baseline synchronous responses in Figure III-11 show subtraction of the runout vector at the lowest running speed, i.e. ~ 1500 rpm.

The direct response comprises the synchronous and non-synchronous contents of the rotor response. Non-synchronous vibration components occur at low shaft speeds

---

[9] Imbalance response tests for increasing supply pressures are shown later.

due to the dry friction generated from the journal and top foil upon contact. Notice that the synchronous components of the baseline condition are not small (~ 5 to 20 μm).

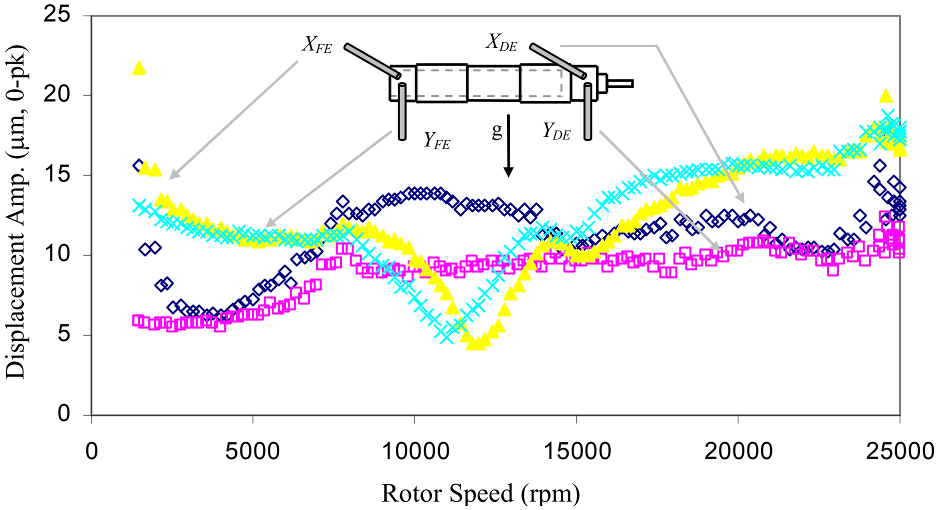

Figure III-10 Amplitude of direct displacement response of rotor baseline condition for air supply pressure at 34.4 kPa [5 psig]

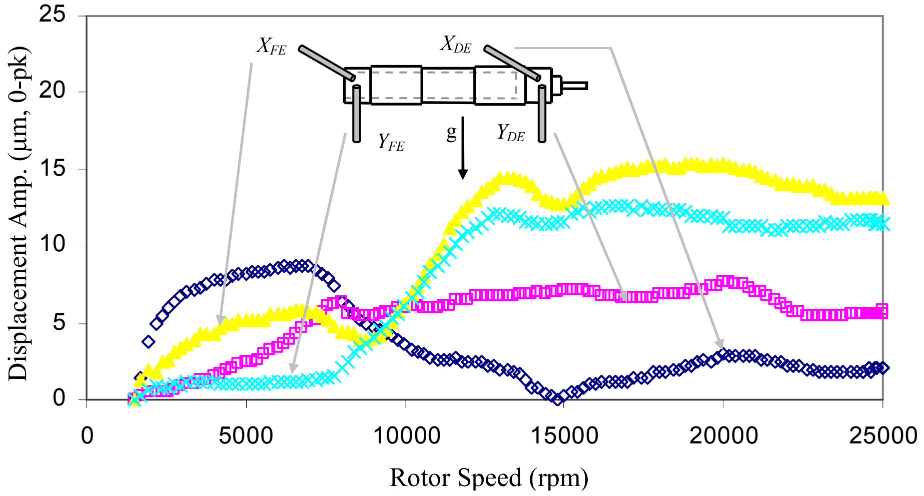

Figure III-11 Amplitude of synchronous displacement responses of the rotor baseline condition for air supply pressure at 34.4 kPa [5 psig]

Figure III-12 and Figure III-13 present waterfall plots of the baseline rotor coastdown response along the horizontal direction for the rotor drive end and free end, respectively. Appendix C shows waterfall plots for the other two measurement locations. Low magnitudes of super-harmonics motions compared to the synchronous magnitudes are noted over the entire shaft speed range. Incipient subsynchronous vibration for the baseline condition is observed at the maximum speed (~ 25 krpm). The frequency of subsynchronous whirl is approximately at the rigid body mode natural frequency (~9,000 rpm (150 Hz)). For shaft speeds lower than 20,000 rpm, the subsynchronous components disappear indicating that the system is stable (no whirl).

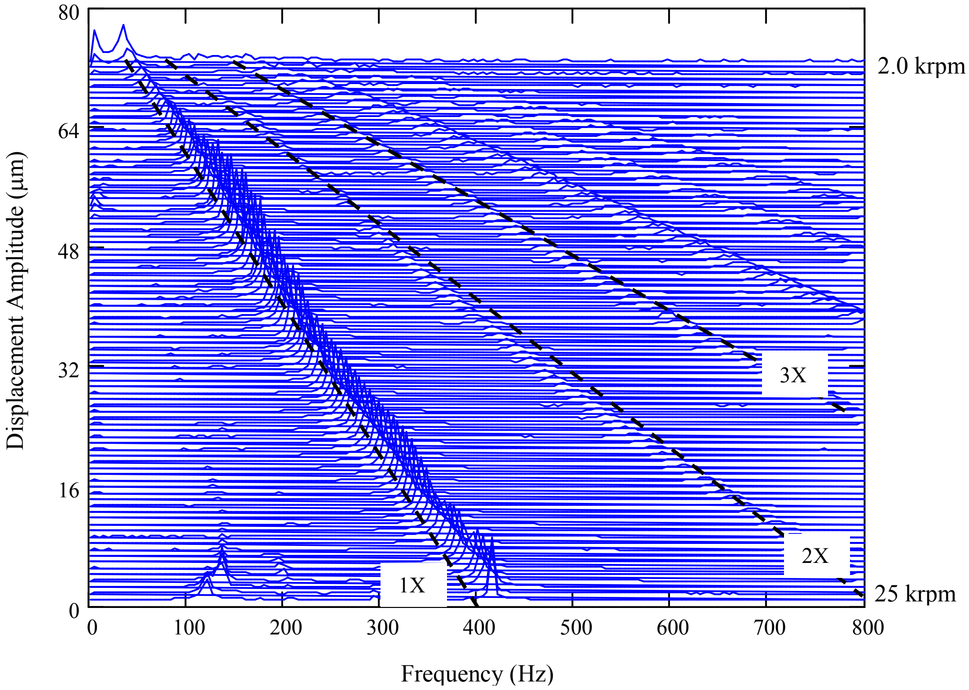

Figure III-12 Waterfall plot of baseline rotor coastdown at drive end, horizontal plane (X_{DE}). Air pressure at 34.4 kPa [5 psig]

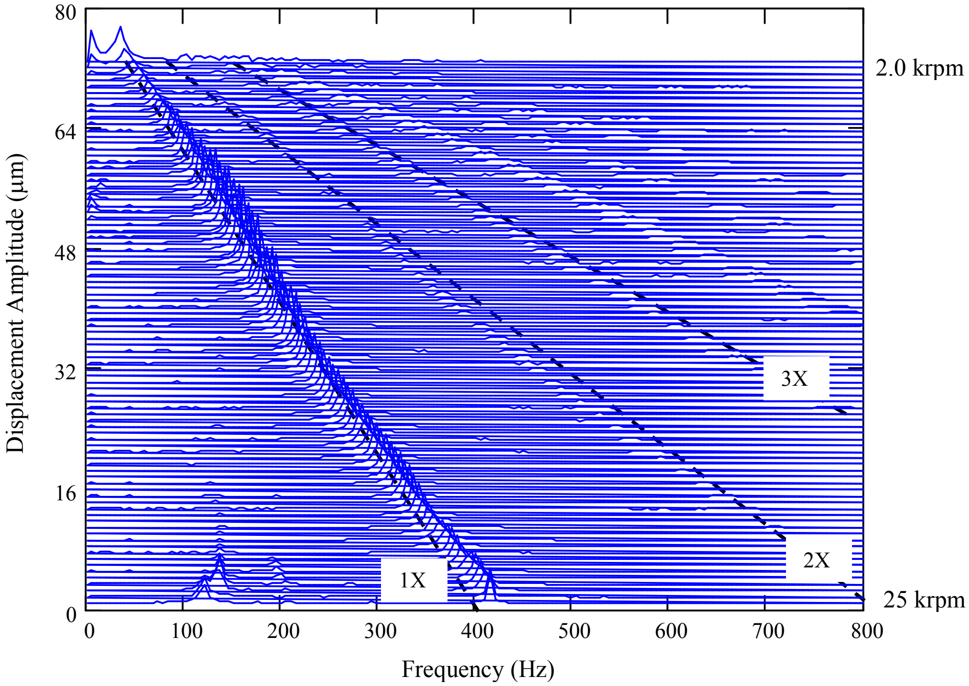

Figure III-13 Waterfall plot of baseline rotor coastdown at drive end, vertical plane (Y_{DE}). Air pressure at 34.4 kPa [5 psig]

CHAPTER IV

ROTORDYNAMIC PERFORMANCE OF A ROTOR SUPPORTED ON THE TEST FOIL GAS BEARINGS – EXPERIMENTAL RESULTS

The rotordynamic performance of the test rotor supported on foil bearings is evaluated by conducting measurements of its response for increasing mass imbalance conditions. Coastdown rotor responses from 25,000 rpm to rest allow observing regions of subsynchronous instabilities and the associated whirl frequencies ratio with respect to the running speed. Shaft motion orbits at selected speeds (below, above, and at the critical speeds) provide an insight of the effect of the spot weld location on the rotor motion behavior. Finally, this chapter presents experimental results of the influence of supply pressure on the rotor imbalance response and the system stability

Estimation of Clearance in Foil Bearings and Static Load Distribution in Test Foil Bearings

The nominal clearance in foil bearing is an ambiguous concept, largely unknown in most applications. The nominal clearance herein is defined as the actual air gap between the journal (shaft) and the foil bearing non-deflected inner bore. A reliable estimation of radial clearance and static load of the test bearings is paramount for predictions of the foil bearing performance shown later in this thesis.

Radial clearances of the foil bearings in the rotor are measured by performing displacement versus static load experiments on the non-rotating test rotor. An electromagnetic load actuator exerts static loads to the test rotor while vertical eddy current sensors record the rotor vertical displacements at the measurements planes. The electromagnetic load tests are performed with no motor attachment to the test rotor. Therefore, the static rotor load is distributed on the test foil bearings. The tests begin with the test rotor resting on the test foil bearings. An upward electromagnetic load is then incrementally increased while recording the rotor displacements. Figure IV-1 illustrates the recorded rotor displacements at the bearing locations versus the applied load. Notice that rotor motions at the bearing locations are not recorded in the tests. However, a simple geometrical transformation assuming a rigid rotor allows obtaining displacements at the bearing locations. Bearing diametral clearances are estimated by marking the boundaries of the high flexibility region on the displacement versus load curves. Using this ad-hoc procedure, the radial bearing clearances are estimated with values shown later in table on p.34.

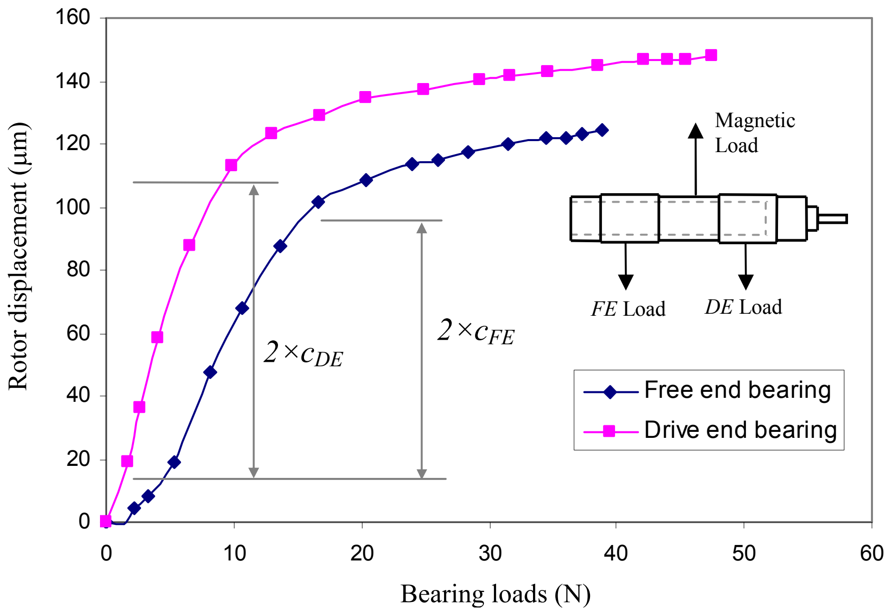

Figure IV-1 Rotor displacement at the free end and drive end bearings for increasing applied electromagnetic loads

On the other hand, the static load distribution among the foil bearings is calculated through a simple static equilibrium analysis of the rotor/bearing system with the motor connected to the rotor/bearing system[10]. Figure IV-2 shows a schematic representation of the forces acting on the test rotor for static conditions. From the static equilibrium analysis of the test rotor, the drive end and free end forces are derived in terms of the static rotor weight and the coupling force as,

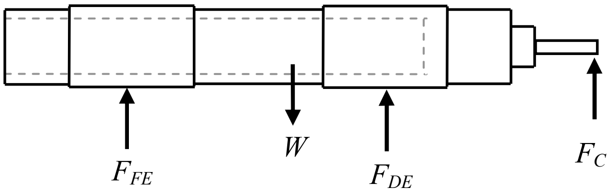

Figure IV-2 Schematic view of acting forces on test rotor for static conditions

$$\begin{aligned} F_{DE} &= 0.62 \cdot W - 1.54 \cdot F_C \\ F_{FE} &= 0.38 \cdot W + 0.61 \cdot F_C \end{aligned} \tag{1}$$

where, F_{DE} and F_{FE} are the static bearing forces, W is the rotor weight (~10 N) and F_C is the coupling static force. The constant coefficients in Equation (1) are obtained from geometrical properties of the test rotor. Figure IV-3 illustrates the influence of the coupling force on the distribution of static load among the test bearings. Notice that for no coupling force, the static bearing loads are 6.5 N and 3.5 N for the drive and free end bearings, respectively. Conversely, for high coupling forces (> 3N), the free end bearing and the coupling solely support the test rotor, while the drive end bearing force contribution is minimal.

On the other hand, notice in Equations (1) that the static equilibrium analysis provides an undetermined system of equations with three unknowns (F_{FE}, F_{DE} and F_C). However, an ad-hoc procedure allows to estimate the static load distribution on the

---

[10] With no motor-shaft connection, the rotor static load distribution on the test bearings are 6.5 N and 3.5 N for the drive end and free end bearings, respectively

flexible coupling, thus giving F_{DE} and F_{FE} from Equations (1). The simple experimental procedure, illustrated in Figure IV-4, consists of recording the rotor motion at the coupling location after attaching the motor to the rotor/bearing system. The ensuing rotor motion at the coupling location is δ_C = 7.6 μm (an average of 10 rotor displacement measurements).

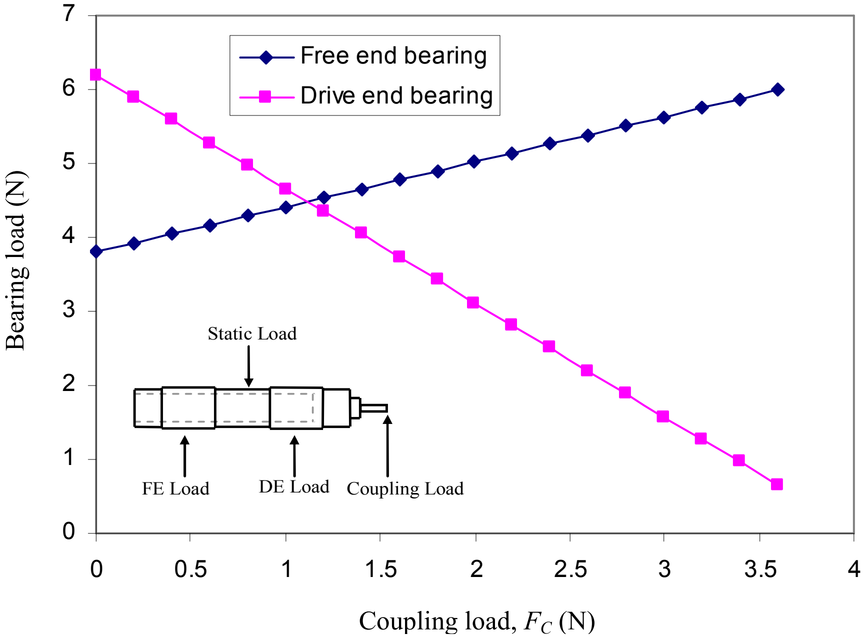

Figure IV-3 Effect of coupling load on the reacting bearing loads

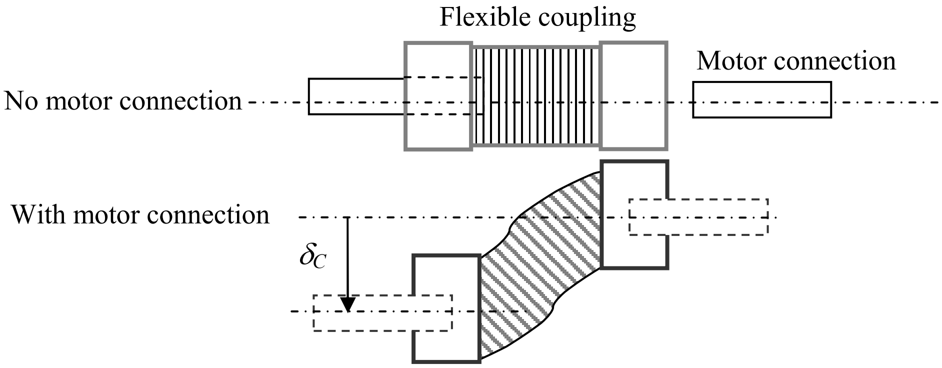

Figure IV-4 Schematic view of coupling deflection when connecting motor

Once obtained the rotor motion at the coupling location, the coupling force (F_C) is estimated by using the measured coupling stiffness (Figure III-6). Notice that there are two distinctive values of coupling stiffness depending on the lateral deflection. For the rotor motion displacement of δ_C = 7.6 μm, the corresponding coupling stiffness is K_C = 0.163 MN/m. Therefore, the resulting coupling force is F_C = 1.23 N. Once obtained the coupling force, the distribution of the rotor static load among the test foil bearings is determined using Equation (4).

Table IV-1 lists the estimated radial clearances and static load for the test foil bearings. Notice that the estimated bearing clearance is larger that the nominal clearance given by the manufacturer (35 μm). The radial clearance uncertainty depends on the selection of the boundaries of the high flexibility region on the displacement versus load curves. The boundaries are set when the rate of change in displacement between consecutive data points is less than 5%. Therefore, the radial clearances for the drive end and free end bearings are 2.11 μm and 2.14 μm, respectively. The static load uncertainty is calculated through a general uncertainty analysis based on the uncertainties in the individual variables (coupling deflection and stiffness) and the equilibrium force equations.

Table IV-1 Estimated radial clearances and static loads for test foil bearings

Bearing	Radial Clearance (μm)	Static Load (N)
Free end bearing	45 ± 2.14	4.5 ± 0.13
Drive end bearing	50 ± 2.11	4.2 ± 0.13

Radial clearance uncertainty associated to instrument accuracy = 1.2 μm
Measurement conducted after imbalance response test were completed

Imbalance Response Tests

Imbalance response tests were conducted with calibrated imbalance masses at the two imbalance planes in the rotor. The distribution of masses leads to two linerly independent responses of the test rotor. For each rotational speed, the baseline condition is subtracted from the measured imbalance response to reveal the actual effect of the mass imbalance used[11]. The imbalance responses, presented herein, are for rotor coastdowns from 15,000 rpm[12]. Table IV-2 summarizes the magnitude of the imbalance masses for the two types of imbalance tests, A and B while Figure IV-5 shows the location of the imbalance masses. In tests A, the imbalance masses are added at the same angular location at the rotor end planes; whereas in tests B, the imbalance masses are out of phase (180°). For each imbalance condition, an imbalance displacement (u) is defined as

$$u = \frac{\left| m_{FE} . r_e . e^{i\phi_{FE}} \right| + \left| m_{DE} . r_e . e^{i\phi_{DE}} \right|}{M + m_{DE} + m_{FE}} \tag{2}$$

where, m_{FE} *and* m_{DE} are the imbalance masses at the free and drive end, respectively, ϕ_{FE} and ϕ_{DE} are the imbalance mass locations at the free and drive end, respectively, M is the rotor mass and r_e is the radial distance of the imbalance location (15.11 mm).

Figure IV-6 shows direct and synchronous coastdown responses at the four measurement locations for imbalance displacement u = 7.4 μm (in phase, test A1). Rotor motions at the bearing locations are not presented due to rotor bending within the speed range of operation.

---

[11] The procedure is strictly correct in a linear system.

[12] The repeatability of test results is significantly better for coastdowns from 15 krpm than those starting from 25 krpm. The lower start speed for coastdowns avoids excessive build up of subsynchronous motions.

Table IV-2 Imbalance mass magnitudes and locations

Imbalance Name	Imbalance mass (m_{FE} / m_{DE}) ± 0.002 g	Imbalance mass location (ϕ_{FE} / ϕ_{DE})	Imbalance displacement (u)
A1	0.24 g / 0.24 g	-18° / -18°	u = 7.4 μm
A2	0.31 g / 0.31 g	-18° / -18°	u = 9.5 μm
A3	0.34 g / 0.34 g	-18° / -18°	u = 10.5 μm
B1	0.12 g / 0.12 g	-18° / 162°	u = 3.7 μm
B2	0.17 g / 0.17 g	-18° / 162°	u = 5.2 μm
B3	0.24 g / 0.24 g	-18° / 162°	u = 7.4 μm

Free and drive end imbalance plane: radius = 15.11 mm
Positive angles on rotor are measured opposite to direction of rotation and from rotating reference, i.e. reflective pick-up mark.

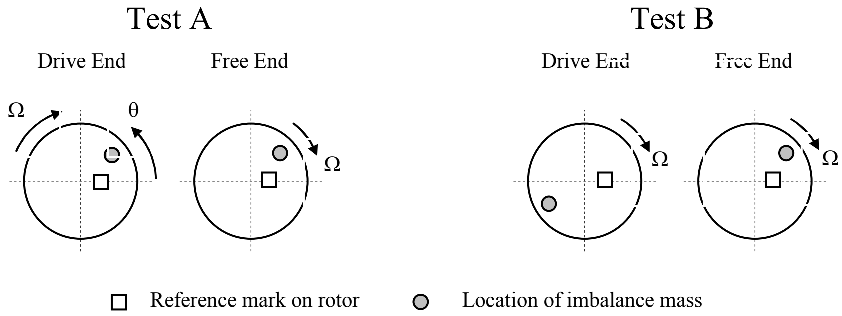

Figure IV-5 Schematic view of the imbalance mass location for Test A and B

Small non-synchronous vibrations occur throughout the entire speed range for this smallest imbalance condition. Rotor motions at the drive end evidence the occurrence of a critical speed at ~ 8.2 krpm while motions at the free end do not manifest this critical speed. Later, analysis of the phasor vectors[13] at the measured displacement signals determine the rigid body shape associated to this critical speed, i.e. cylindrical or conical. Figure IV-7 displays direct and synchronous coastdown responses for a large imbalance displacement, i.e. u = 10.5 μm (in phase). Synchronous magnitudes for all measurement locations indicate a clear critical speed occurring at 8.2 krpm. On the other hand, nonsynchronous motions initiate at 20.5 krpm and disappear at 12 krpm. This speed range encloses a speed twice the system first critical speed. Sub-synchronous vibrations are also observed near the critical speed. A following section presents waterfall plots for this imbalance condition showing the frequencies at which these non-synchronous vibrations occur. Figure IV-6 and Figure IV-7 indicate that subsynchronous vibrations are more notorious when imbalance masses are the largest. Similarly, Figure IV-8 presents synchronous and direct coastdown responses for an out of phase imbalance displacement of u = 5.2 μm. Subsynchronous vibrations initiate at twice the system critical speed and disappear at approximately 12.5 krpm. It is important to notice that the synchronous responses shown in Figure IV-6 through Figure IV-8 do not show subtraction of the baseline condition.

---

[13] The phasor vector contains the amplitude and phase angle of the time measured signals.

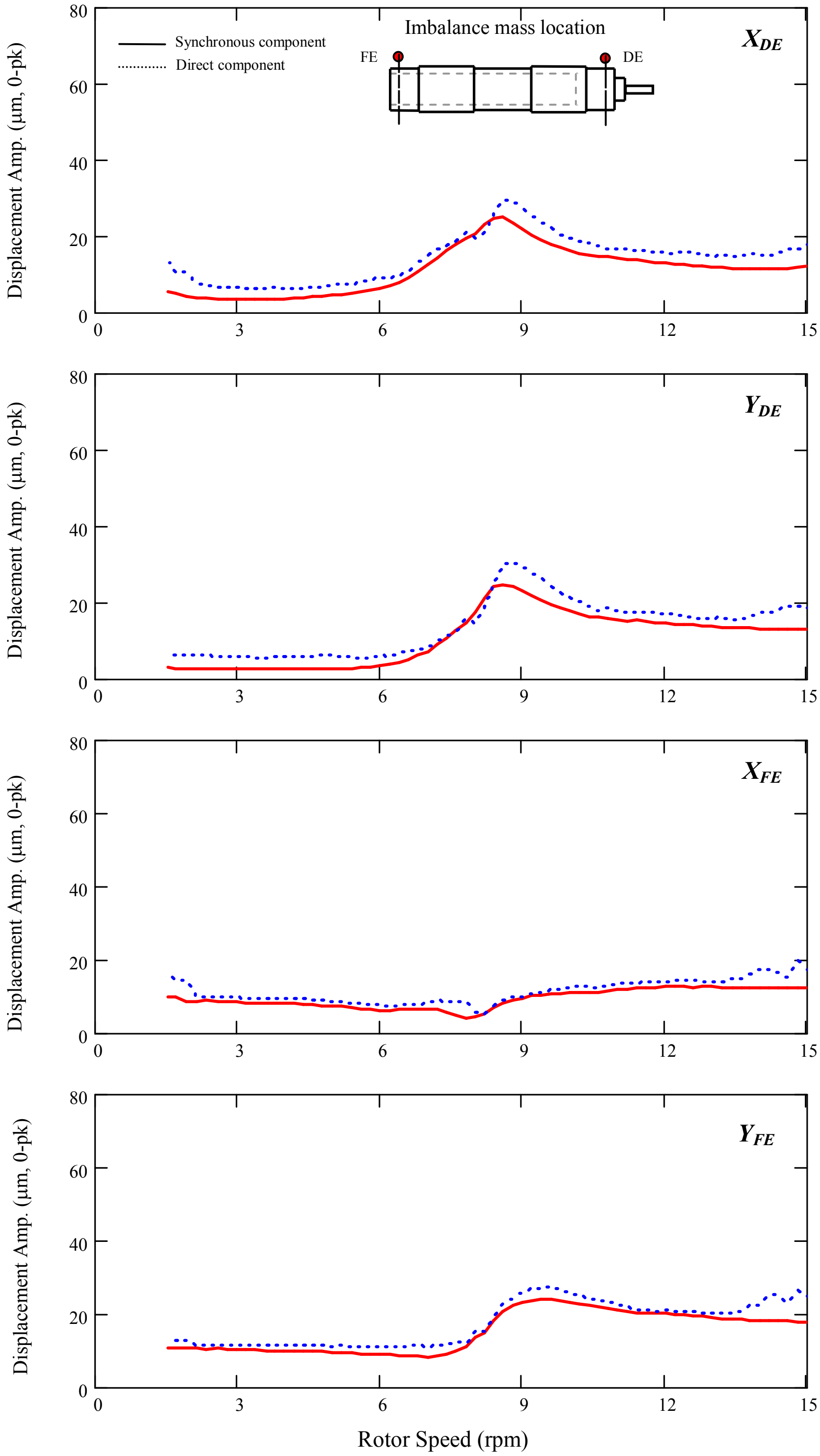

Figure IV-6 Direct and synchronous coastdown response for an imbalance displacement of u = 7.4 µm (in phase, Test A1). Air pressure at 34.4 kPa [5 psig]

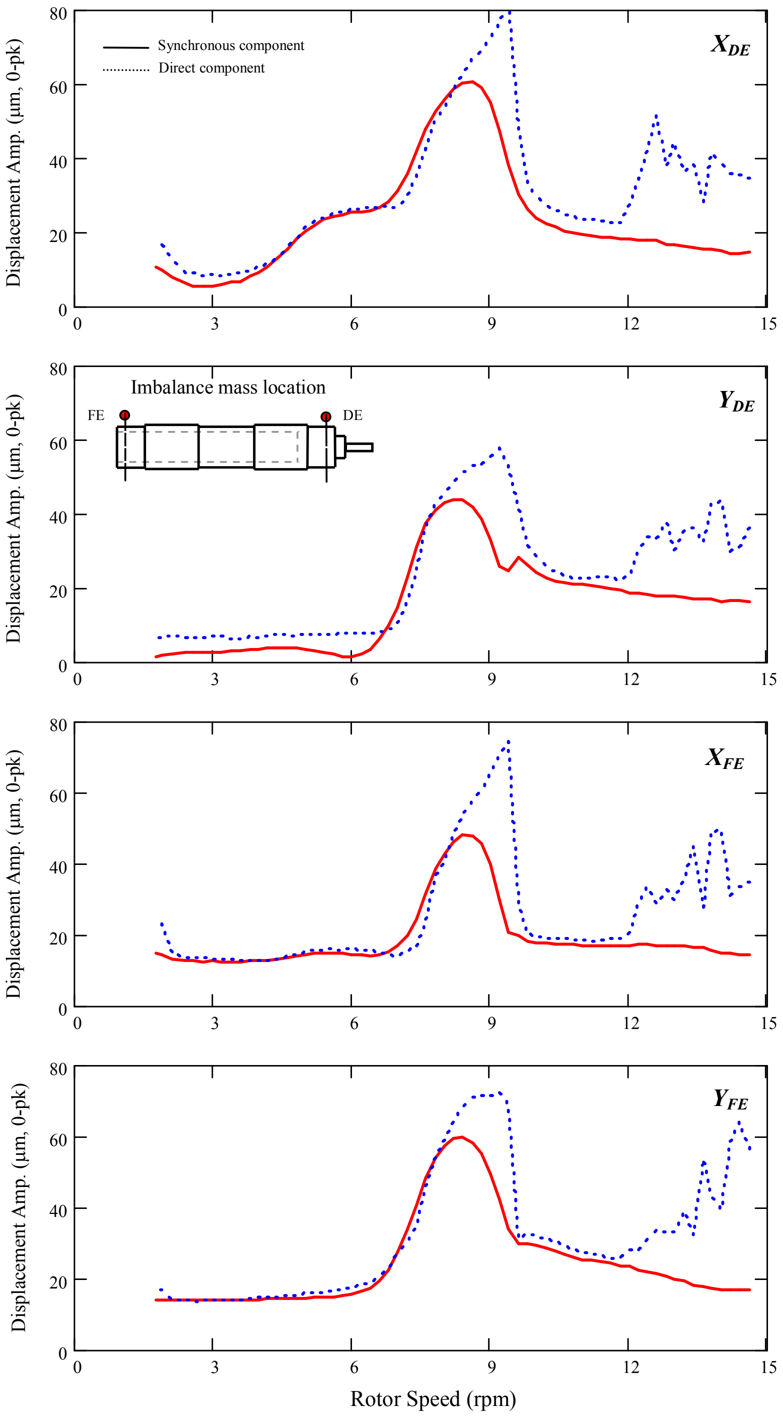

Figure IV-7 Direct and synchronous coastdown response without baseline subtraction for an imbalance displacement of u = 10.5 μm (in phase, Test A3). Air pressure at 34.4 kPa [5 psig]

The two distinctive imbalance tests allow identification of the first two rigid body mode critical speeds. From imbalance tests A, the first critical speed is at approximately 8.2 krpm; while from imbalance tests B, the second critical speed occurs at approximately 9.0 krpm. Note that for imbalance tests B, the first rigid body mode critical speed is excited at the horizontal drive end location while at other locations the second rigid body mode is excited.

Figure IV-9 through Figure IV-12 present synchronous rotor responses for increasing imbalance masses. Recall that the imbalance responses show the subtraction of the baseline condition. Figure IV-9 and Figure IV-10 depict measured responses at the rotor drive end and free end (horizontal plane), respectively, for imbalance tests A. Experimental results in Figure IV-11 and Figure IV-12 correspond to imbalance tests B at the rotor drive and free ends (vertical plane), respectively. Amplitudes of synchronous motions (1X) are largely different for vertical and horizontal rotor motions, thus evidencing the anisotropy of the test foil bearings. Recall that the test foil bearings are installed with the spot weld at 45º clockwise from the top vertical orientation. A later section in this chapter details on the linearity of the rotor response to imbalance.

Figure IV-9 through Figure IV-12 also show the phase angle changes of the measured signals for the entire speed range. A clear shift in the phase angle near the two first critical speeds is distinguished for all imbalance conditions. Appendix D shows the synchronous and direct rotor responses for the remaining imbalance conditions, i.e. A2, B1, and B3 (refer to Table IV-2 for imbalance displacement magnitudes). Appendices E and F show the synchronous responses and phase angles at the locations not shown in this section for imbalance tests A and imbalance tests B, respectively.

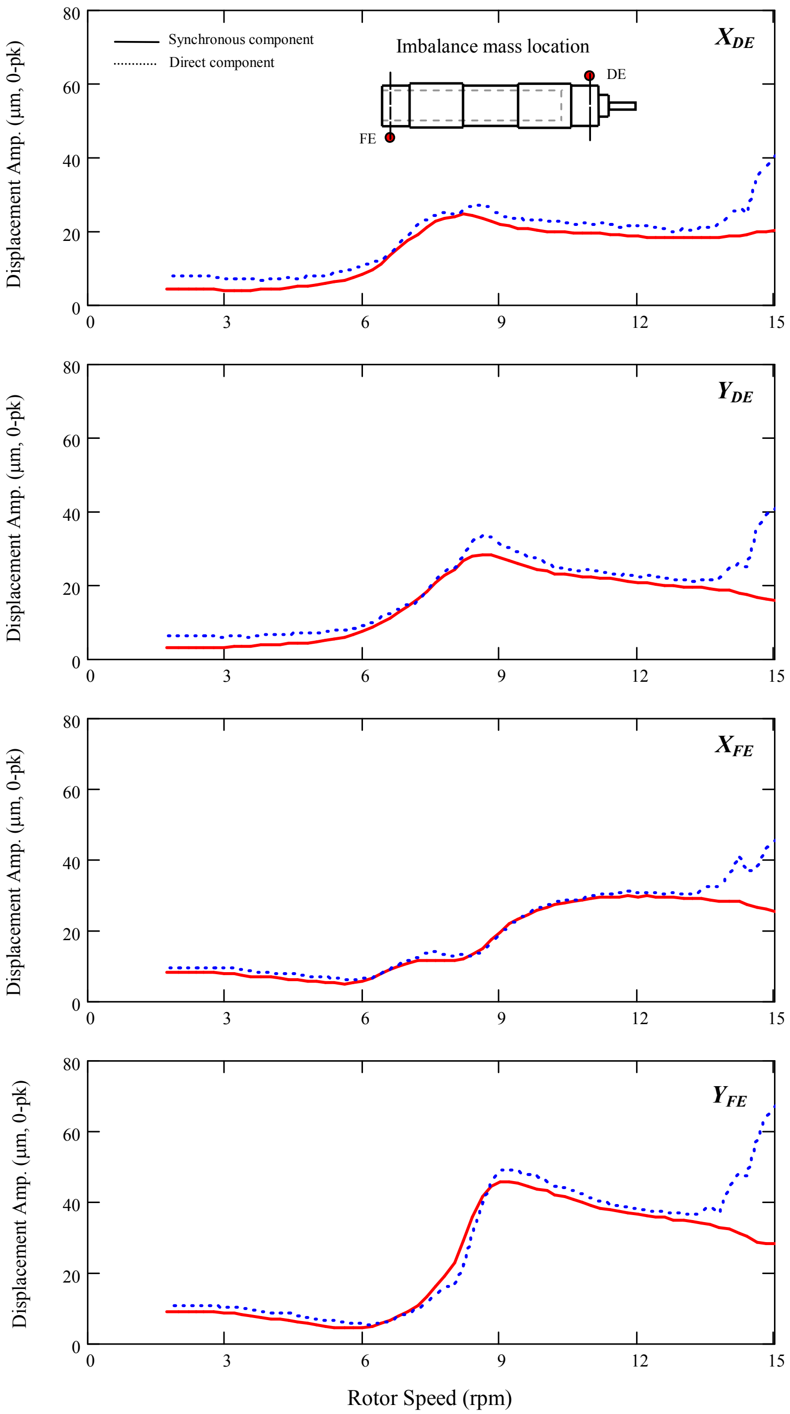

Figure IV-8 Direct and synchronous coastdown response without baseline subtraction for an imbalance displacement of u = 5.2 μm (out of phase, test B2). Air pressure at 34.4 kPa [5 psig]

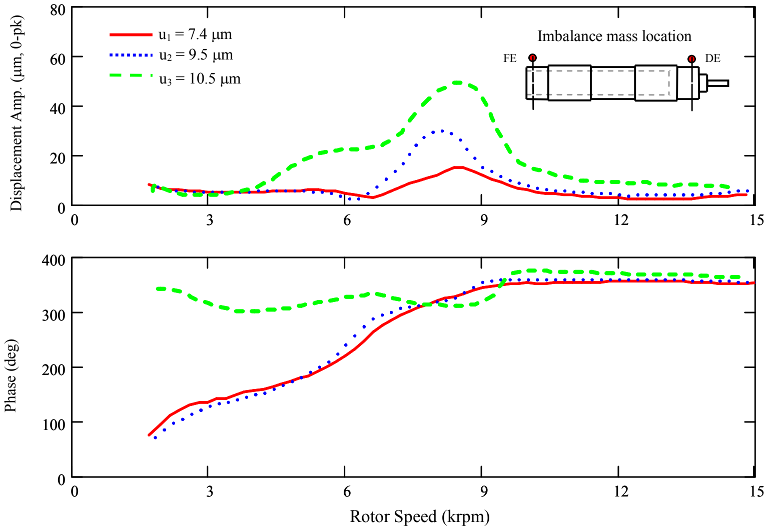

Figure IV-9 Synchronous rotor response amplitude with baseline subtraction and phase angle for imbalance tests A. Air pressure at 34.4 kPa [5 psig]. Measurements taken at drive end, horizontal direction (X_{DE})

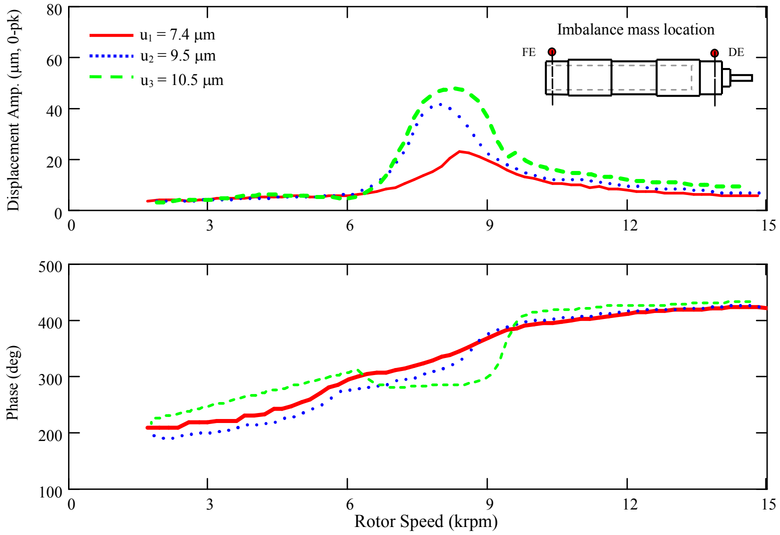

Figure IV-10 Synchronous rotor response amplitude with baseline subtraction and phase angle for imbalance tests A. Air pressure at 34.4 kPa [5 psig]. Measurements taken at free end, horizontal direction (X_{FE})

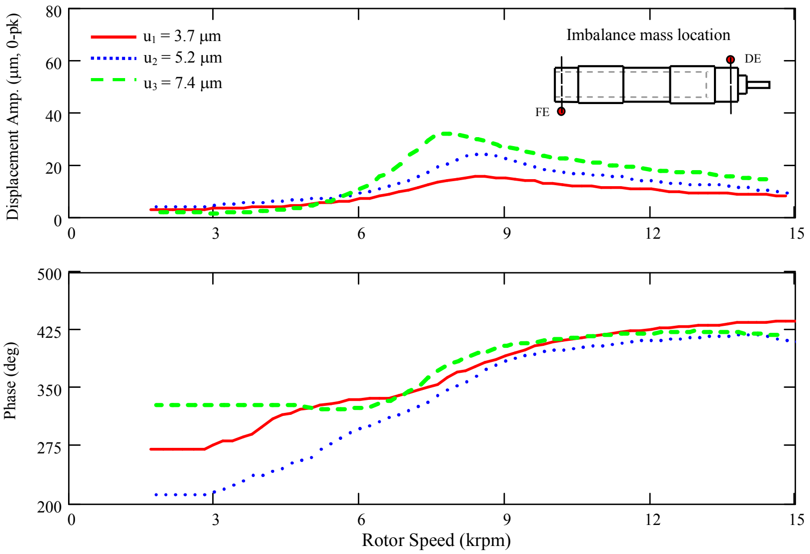

Figure IV-11 Synchronous rotor response amplitude and phase angle for imbalance tests B. Air pressure at 34.4 kPa [5 psig]. Measurements taken at drive end, vertical direction (Y_{DE})

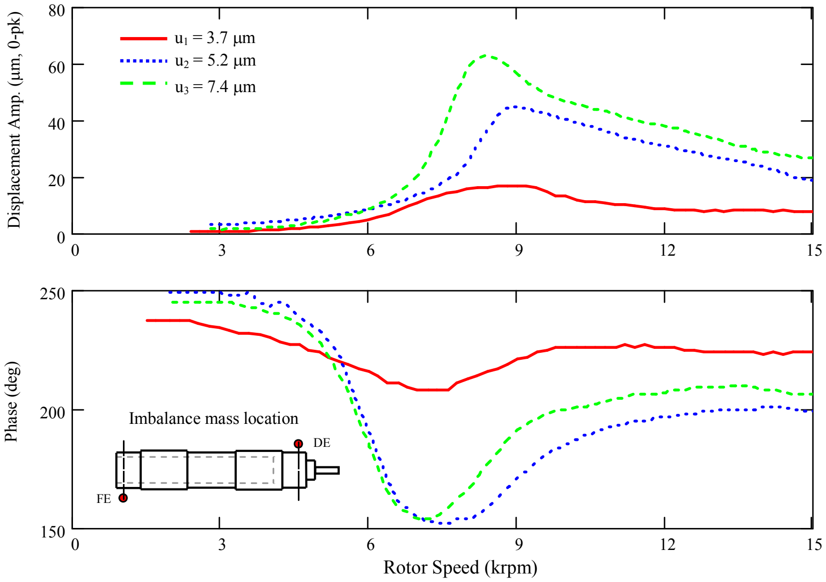

Figure IV-12 Synchronous rotor response amplitude and phase angle for imbalance tests B. Air pressure at 34.4 kPa [5 psig]. Measurements taken at free end, vertical direction (Y_{FE})

Rotor/Bearing System (Non) Linearity

The synchronous rotor response for increasing imbalance masses allows verifying the rotor system linearity for in-phase and out-of-phase imbalance conditions. In a linear mechanical system, an increase in the excitation force, *nF*, leads to a proportional increase in the system response, *nX*, where *n* is an constant. The system is characterized by material parameters not determined by the motion or system state. An amplitude ratio (*AR*) of the rotor imbalance responses relative to the lowest imbalance conditions is defined to check the rotor/bearing linearity. The definition of the amplitude ratio is given as,

$$AR_i = Amp_i \frac{u_1}{u_i} \tag{3}$$

where, Amp_i is the amplitude of rotor synchronous response to an imbalance u_i, and u_1 is the lowest imbalance mass for each condition (in-phase and out-phase), see Table IV-2. Synchronous rotor responses with baseline subtraction are used to calculate the amplitude ratios.

Figure IV-13 shows amplitude ratios for in-phase imbalance conditions at the measurement rotor locations. Figure IV-14 shows similar plots for out-of-phase imbalance conditions. In general, amplitude ratios at the critical speeds for increasing imbalance conditions are slightly different, in particular for the smallest in-phase imbalance condition. Notice that amplitude ratios at the critical speed for the two largest imbalance conditions are similar at all measurement planes, except at the horizontal drive end. In addition, some imbalance responses show a shift in critical speeds of approximately 8%. The rotor/bearing system linearity is not proven, since the amplitude of imbalance response at the critical speed is not proportional to the imbalance masses. The apparent system non linearity may arise from the gas foil bearings and the flexible coupling mechanism.

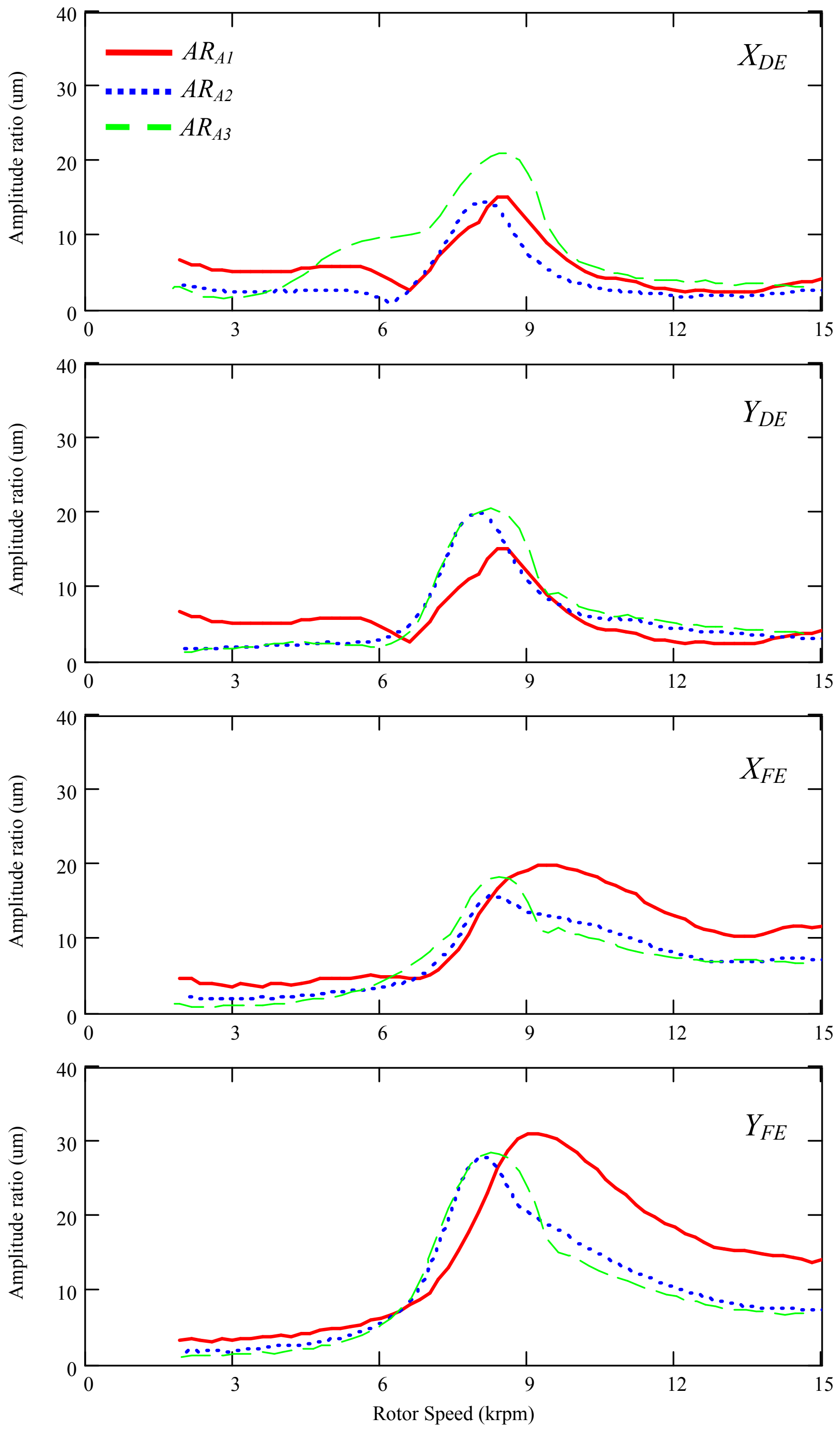

Figure IV-13 Amplitude ratio (*AR*) of rotor synchronous response at the measurement planes for in-phase imbalance conditions. (Remnant imbalance response subtracted)

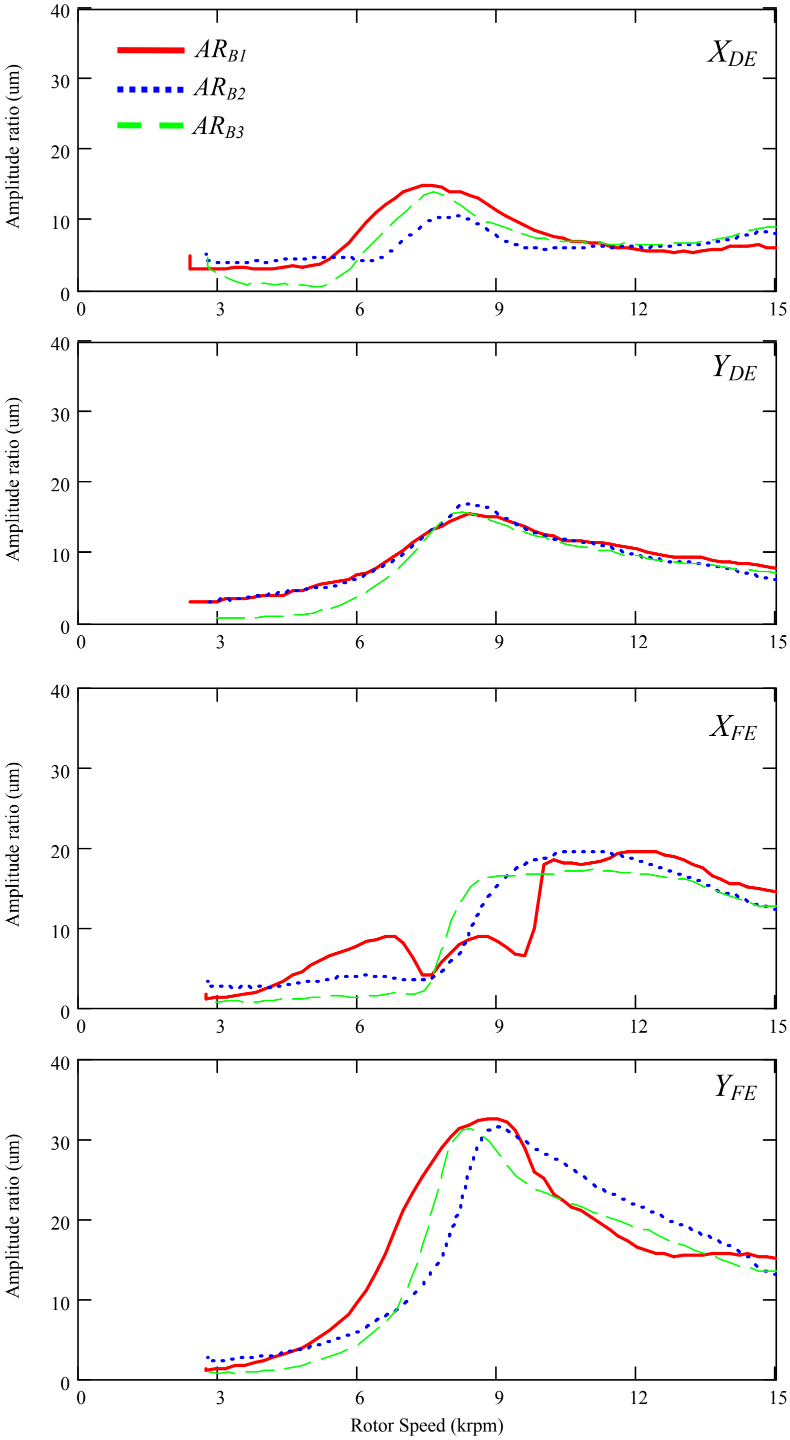

Figure IV-14 Amplitude ratio (*AR*) of rotor synchronous response at the measurement planes for out-of-phase imbalance conditions. (Remnant imbalance response subtracted)

Waterfall Analysis of Coastdown Rotor Responses

Synchronous and subsynchronous vibrations of coastdown tests from 25,000 rpm are analyzed below. Waterfall plots are presented for imbalance displacements u = 7.4μm (in phase), u = 10.5 μm (in phase), and u = 5.2 μm (out of phase). Figure IV-15 shows a waterfall plot of the rotor coastdown response for an imbalance displacement of u = 7.4μm (in phase). Figure IV-16 displays the corresponding synchronous and subsynchronous components and the whirl frequency ratio (*WFR*). The *WFR* is the ratio of subsynchronous frequency whirl to the shaft angular frequency. In general, synchronous motion dominates the rotor response for the entire coastdown speed range, i.e. 25 krpm to 2 krpm. Recall that the imbalance rotor responses presented in the previous section relate to coast downs from 15 krpm; whereas the waterfall plots are obtained for coastdowns from 25 krpm. Therefore, experimental results from both set of experiments may differ due to lack of repeatability for coastdowns starting from different initial speeds.

Figure IV-17 depicts waterfall plots of the rotor coastdown response for an imbalance displacement of u = 10.5 μm (in phase). Subsynchronous motions exist from ~ 20.5 krpm to 15.0 krpm with a 50% typical whirl frequency ratio, see Figure IV-18. Below 15 krpm, the subsynchronous whirl motion bifurcate into two whirl ratios, ~0.55 and ~0.45; until disappearing at a shaft speed of ~12.5 krpm. For lower shaft speeds, no major subsynchronous motions are observed.

Figure IV-19 shows waterfall plots of the rotor coastdown response for an imbalance displacement of u = 7.4 μm (out of phase). Figure IV-20 presents amplitudes of synchronous and subsynchronous components and whirl frequency ratios for this imbalance condition. A similar subsynchronous motion behavior than in the previous imbalance condition (see Figure IV-18) is evident, i.e. two subsynchronous motion regions with distinctive whirl frequency ratios.

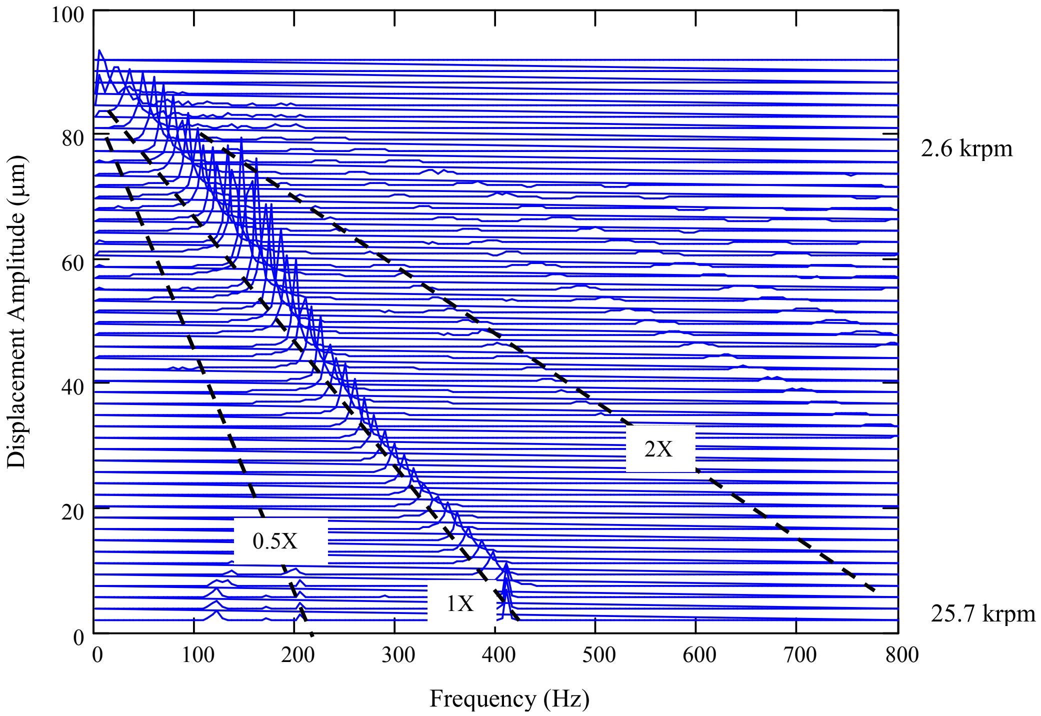

Figure IV-15 Waterfall plot of coastdown response for imbalance displacement u = 7.4 μm (in phase, test A1). Air pressure at 34.4 kPa [5 psig] and measurements at rotor free end, vertical plane (Y_{FE})

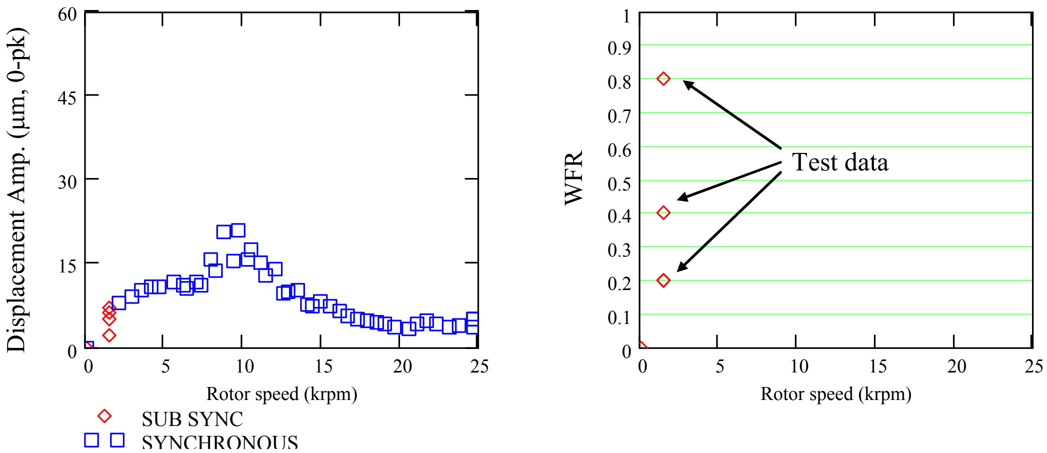

Figure IV-16 Filtered components of synchronous and subsynchronous vibrations and whirl frequency ratio for imbalance displacement *u* = 7.4 μm (in phase, test A1). Air pressure at 34.4 kPa [5 psig] and measurements at rotor free end, vertical plane (Y_{FE})

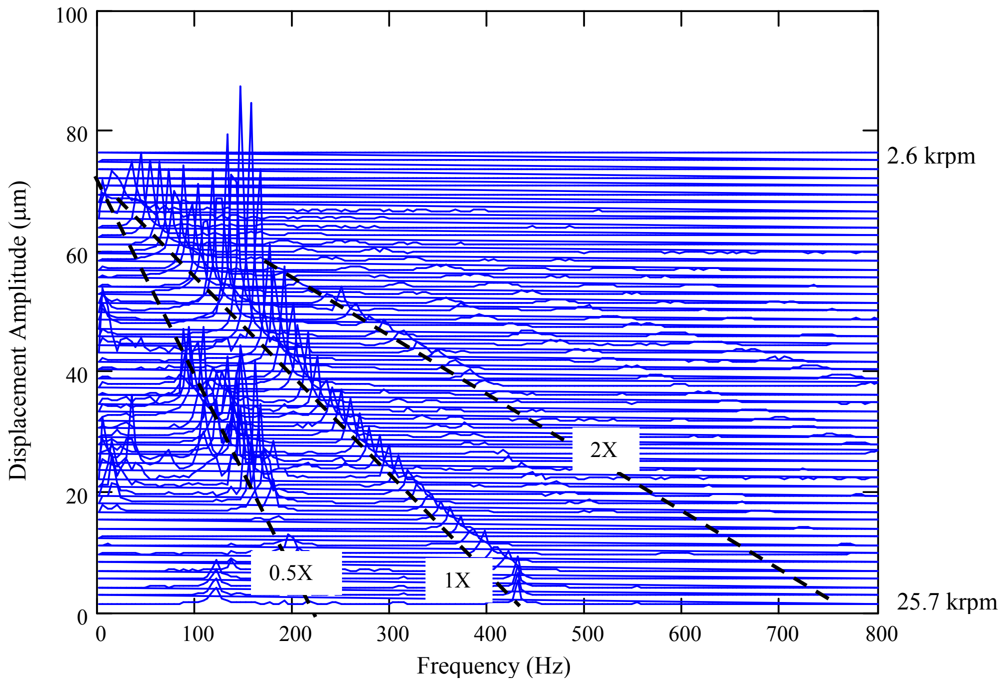

Figure IV-17 Waterfall plot of coastdown response for imbalance displacement *u* = 10.5 μm (in phase, test A3). Air pressure at 34.4 kPa [5 psig] and measurements at rotor free end, vertical plane (Y_{FE})

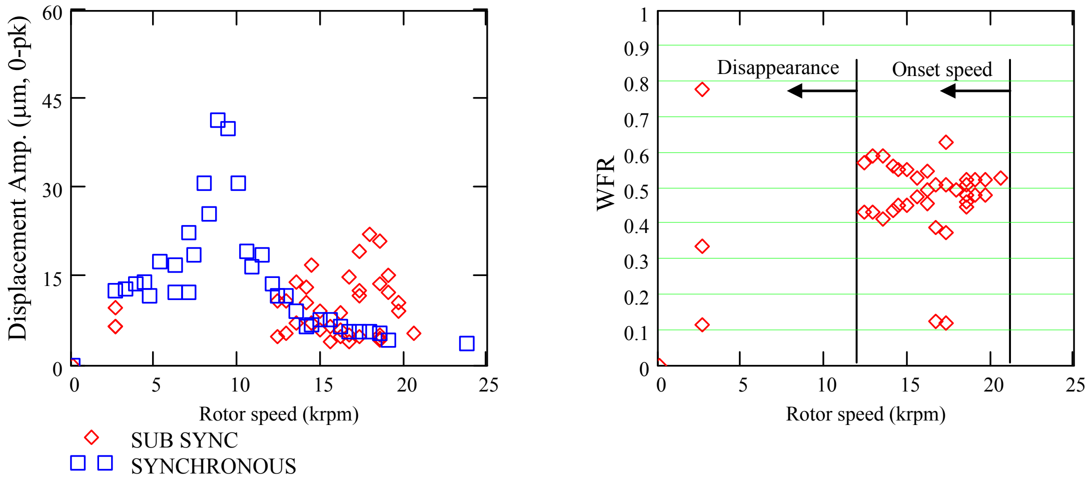

Figure IV-18 Filtered components of synchronous and subsynchronous vibrations and whirl frequency ratio for imbalance displacement u = 10.5 μm (in phase, test A3). Air pressure at 34.4 kPa [5 psig] and measurements at rotor free end, vertical plane (Y_{FE})

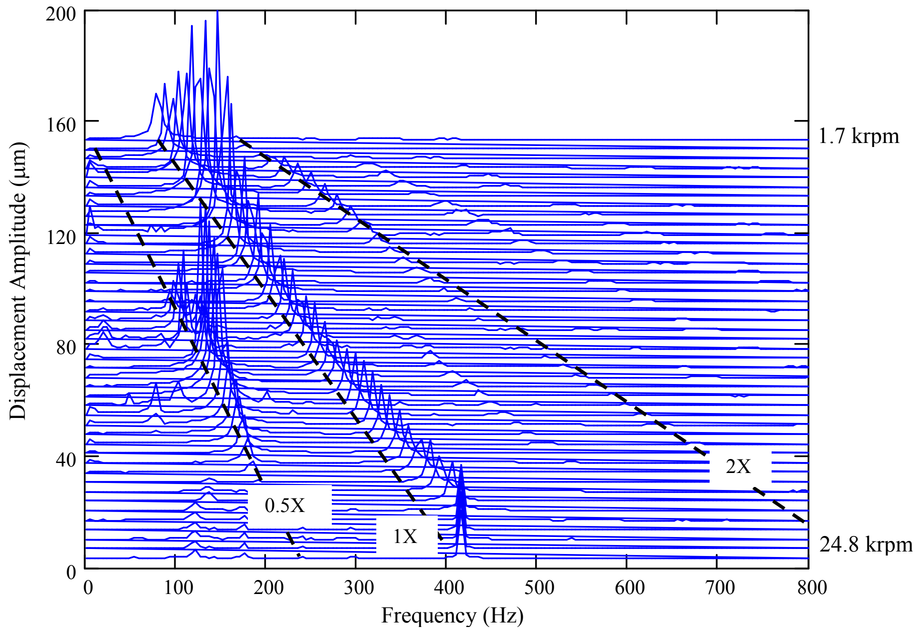

Figure IV-19 Waterfall plot of coastdown response for imbalance displacement *u* = 7.4 µm (out of phase, test B2). Air pressure at 34.4 kPa [5 psig] and measurements at rotor free end, vertical plane (Y_{FE})

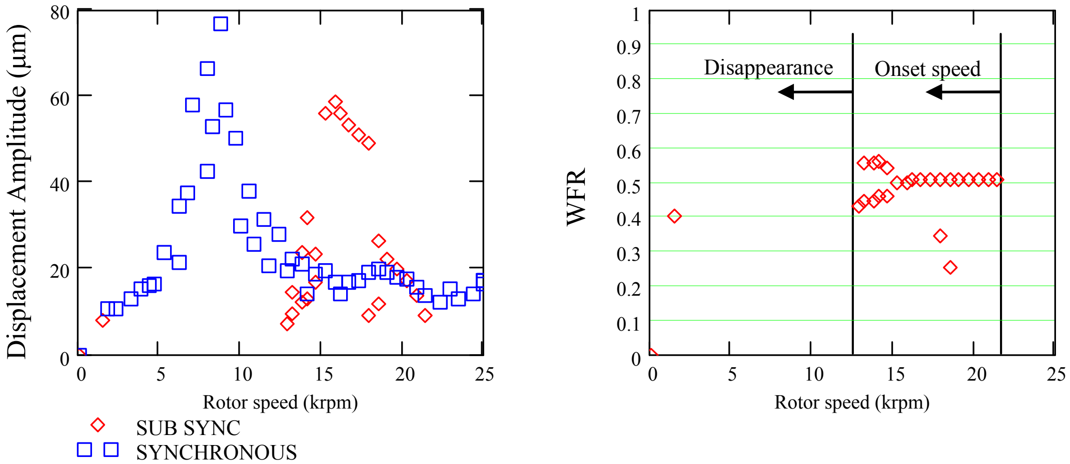

Figure IV-20 Filtered components of synchronous and subsynchronous vibrations and whirl frequency ratio for imbalance displacement u = 7.4 µm (out of phase, test B2). Air pressure at 34.4 kPa [5 psig] and measurements at rotor free end, vertical plane (Y_{FE})

In general, imbalance masses of increasing magnitude have a larger impact on the amplitudes of subsynchronous motion. Also, the speed range with more subsynchronous motion activity occurs near twice the system critical speeds, i.e. ~16.4 krpm and ~18 krpm. The rotordynamic performance of the test foil bearings show similar results as in other experimental programs reported in the literature, see Table II-1 on p.9. Typically, rotors supported on gas foil bearings show subsynchronous whirl frequencies coinciding with the system natural frequencies [22, 23]. Figure IV-21 shows the subsynchronous amplitudes versus their corresponding whirl frequencies for the maximum imbalance magnitudes of each test. The most severe (largest amplitudes of motion) occur at whirl frequencies ω_1 = 120 Hz (7,200 rpm) and ω_2 = 150 Hz (9,000 rpm). The experimental results thus show the severity of subsynchronous motions is related to the amount of imbalance. This shows a forced nonlinear phenomenon not an instability which is a self-excited phenomenon.

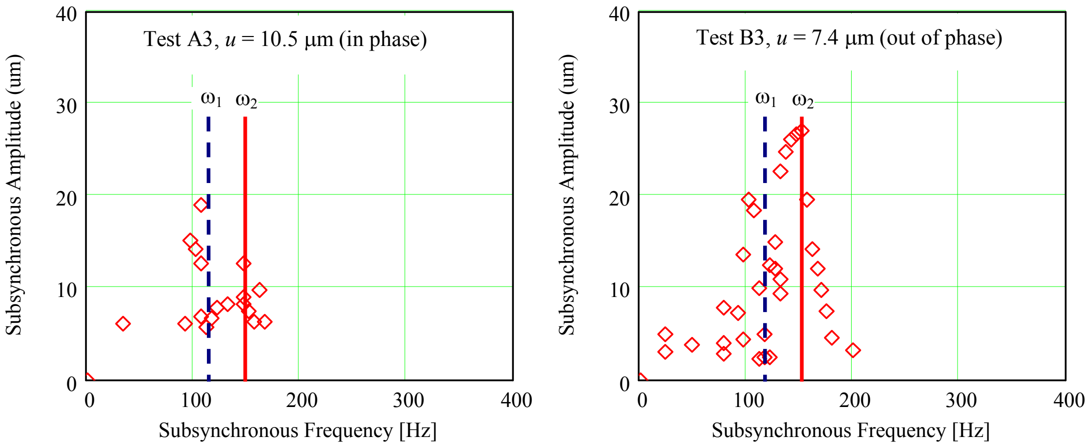

Figure IV-21 Subsynchronous amplitudes and frequencies of occurrence for imbalance u = 10.5 μm (in phase) and u = 7.4 μm (out of phase)

Rotor Motion Orbits at Various Shaft Speeds

Motions orbits of the test rotor are obtained from the time varying displacement signals (vertical and horizontal) at selected shaft speeds. Figure IV-22 show synchronous filtered and direct motion orbits, at the rotor drive and free ends, for rotor speeds equal to 3.8 krpm; 8.2 krpm, and 16.7 krpm. The data corresponds to the largest *in-phase* imbalance, i.e. u = 10.5 μm. Figure IV-23 depict also orbital motions for the largest *out-of-phase* imbalance, i.e. u = 7.4 μm, at 4.7 krpm; 9.1 krpm, and 16.4 krpm

Figure IV-22B and Figure IV-23B display rotor orbits at the critical speeds, 8.2 krpm and 9.1 krpm, corresponding to the in phase and out of phase imbalances. The synchronous orbits at both rotor ends are clearly out of phase indicating the occurrence of a conical mode shape. The angle of the major axis of the elliptical orbit is about 45º from the horizontal plane, i.e. coinciding with the direction of the spot-weld for the top foil. Figure IV-22C and Figure IV-23C show rotor motion orbits at shaft speeds around twice the critical speed (~16 krpm). The rotor response contains large amplitude subsynchronous components with a whirl ratio of nearly 50% shaft speed. Again, the elliptical orbits appear to align with the spot weld location, in particular for the *in-phase* imbalance test.

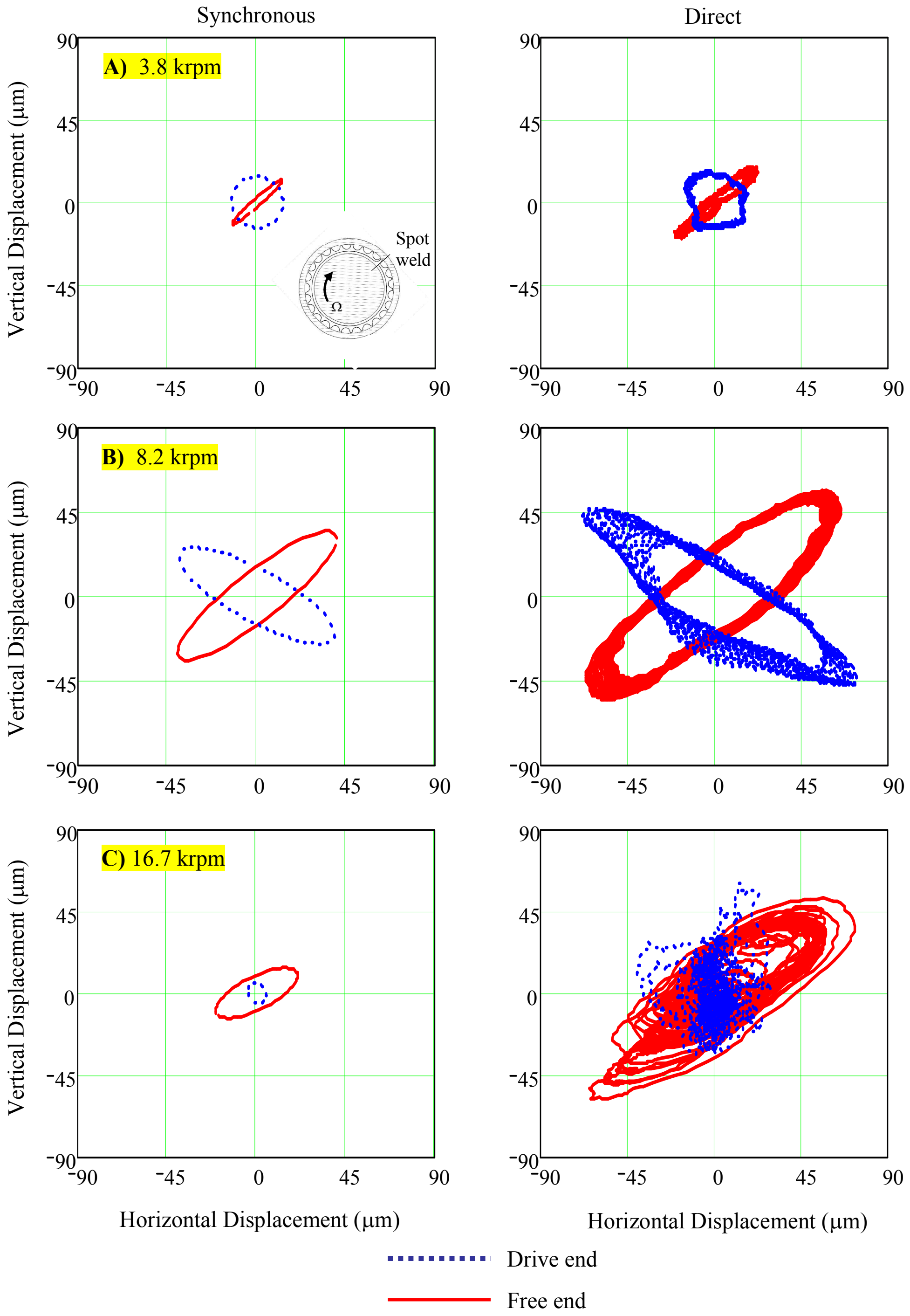

Figure IV-22 Synchronous and direct motion orbits at the drive and free rotor ends for an imbalance u = 10.5 μm (in phase). A) Rotor speed 3.8 krpm, B) 8.2 krpm and C) 16.7 krpm

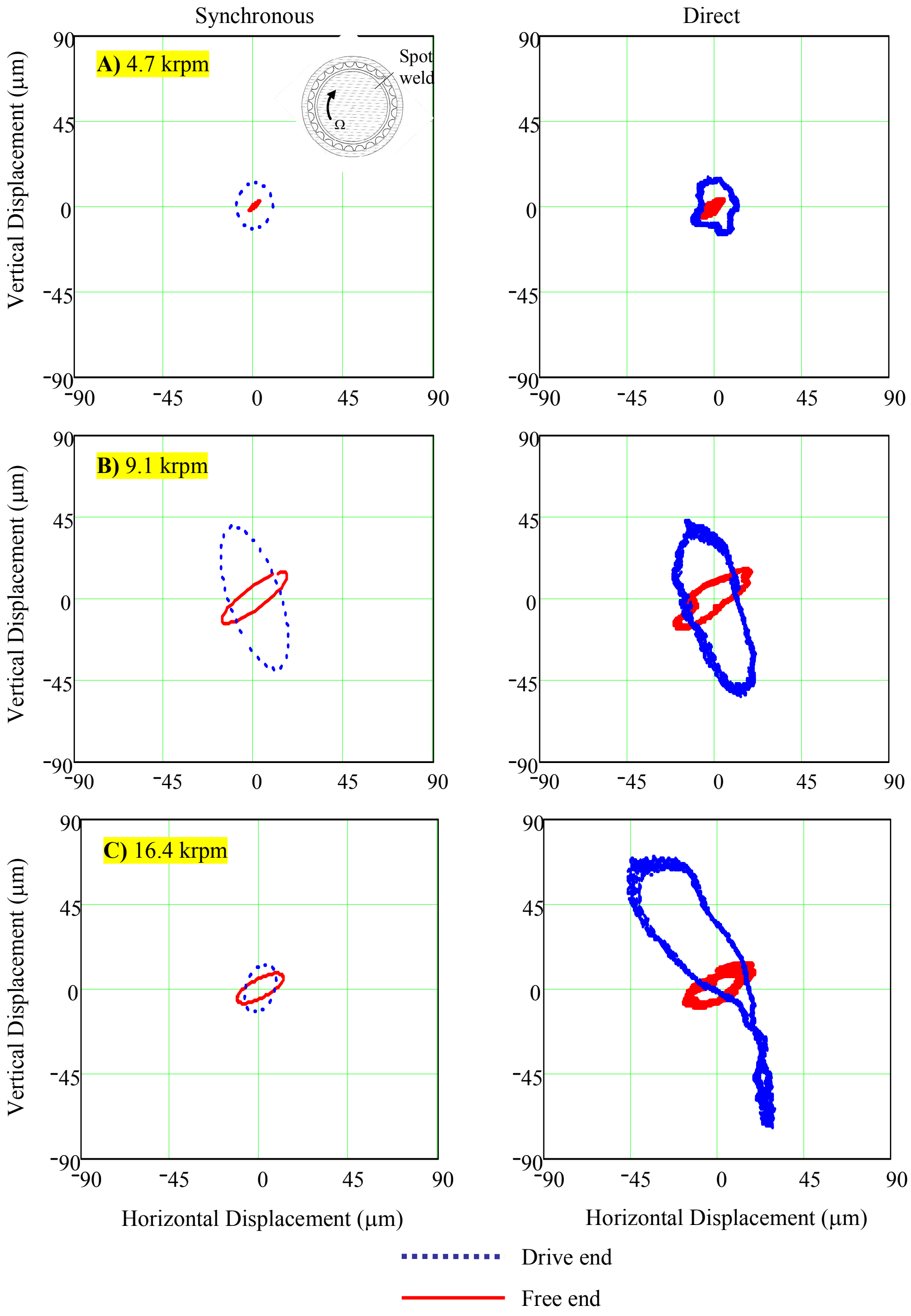

Figure IV-23 Synchronous and direct motion orbits at the drive and free rotor ends for an imbalance u = 7.4 μm (out of phase). A) Rotor speed 4.7 krpm, B) 9.1 krpm and C) 16.4 krpm

Effect of Air Pressurization on Imbalance Response and System Stability

This section presents experimental results of the influence of supply pressure on the rotor imbalance response and the system stability. Recall that the air supply inlet is at the test rig casing middle plane and exits axially through the test foil bearings. In these tests, the electromagnet was removed and a Plexiglas casing sealed the middle of the rig casing holding the bearings.

Constant speed tests for five air pressures equal to 40 kPa [6 psig], 136 kPa [20 psig], 204 kPa [30 psig], 272 kPa [40 psig] and 340 kPa [50 psig] followed. The test rotor imbalance is u = 4.7 μm (*in phase* condition). One must realize that the test supply pressures are not currently practical for industrial applications using gas foil bearing since they require additional power out of the rotating machine. In actuality, the differential pressure across the bearing axial length is very small (~ 7 kPa [1psig]), enough to affect the needed cooling flow [34]. The selected test supply pressure intends to provide experimental evidences of the influence of (small and large) air pressurization on the response to imbalance and system stability. These experimental results may apply to industrial turbomachines where high-pressure process fluid can be allowed to flow through the supporting bearings such as cryogenic turbopumps, multi-stage compressors, and aircraft engines, among other. In these applications, gas foil bearings are foreseen to be implemented to achieve lighter turbomachinery with less maintenance and fewer harmful emissions.

Figure IV-24 and Figure IV-25 show, for increasing supply pressure, the amplitudes of synchronous motions at shaft speeds coinciding with the system critical speed and twice its value. The supply pressure evidently ameliorates the synchronous amplitude at the critical speed. Changes in feed pressure barely affect the synchronous amplitude at the higher shaft speed, as seen Figure IV-25.

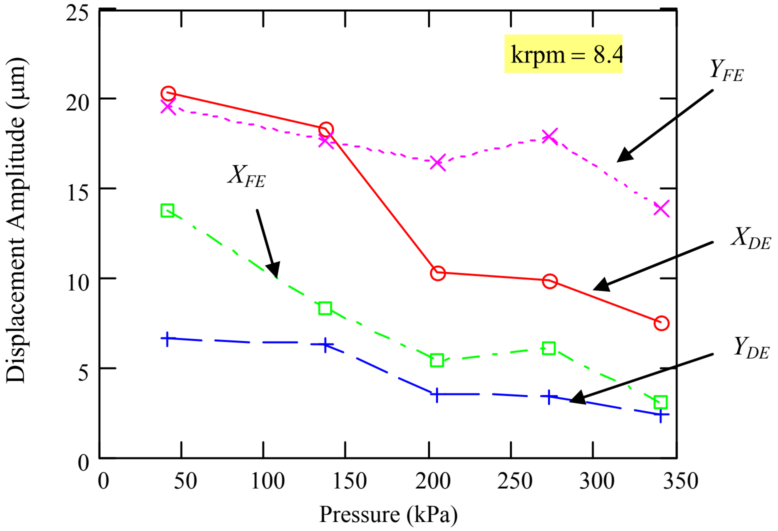

Figure IV-24 Synchronous vibrations at 8.4 krpm for increasing air supply pressures. Measurements taken at the four eddy current sensors

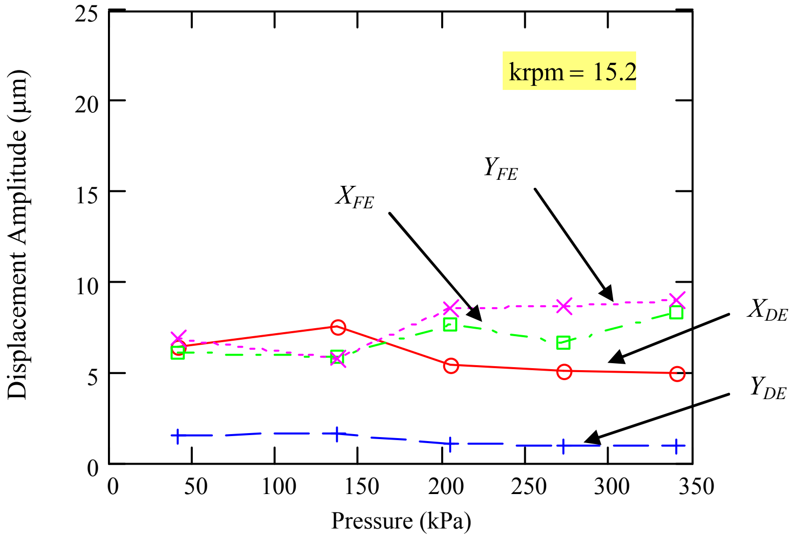

Figure IV-25 Synchronous vibrations at 15.2 krpm for increasing air supply pressures. Measurements taken at the four eddy current sensors

Air pressurization acts to reduce the rotor motion amplitude at the critical speeds, thus denoting an increase of damping at the foil bearings. The enhanced damping may arise from a “hovering” effect of the air flowing underneath the bearing top foil, as depicted in Figure IV-26. A very thin film of gas “lubricates” the contact regions allowing the bumps to slide over the bearing surface, thus dissipating more energy. No changes were noted in the system critical speed when increasing the supply pressure, thus discarding a *Lomakin* type effect. Experiments without rotor spinning further demonstrate that air pressurization does not load the foil or bumps since the rotor static position did not change.

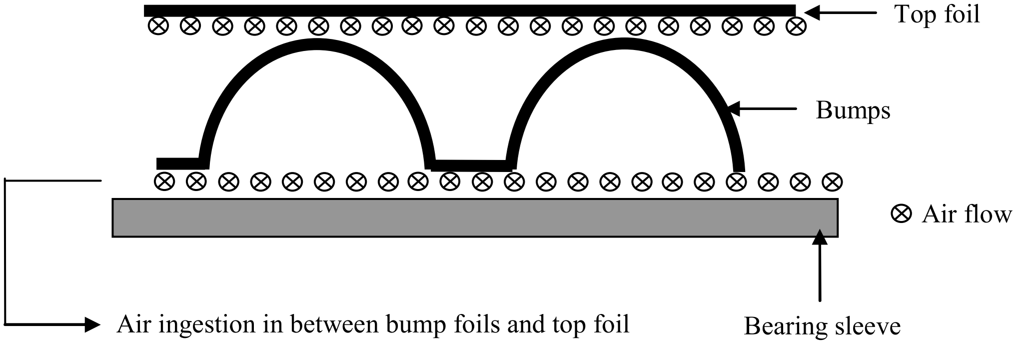

Figure IV-26 Schematic representation of air axial flow through test foil bearings

The effect of air supply pressure on the rotor/bearing stability was also evaluated for operation at a constant shaft speed (15.2 krpm), ~ twice the system critical speed. Figure IV-27 and Figure IV-28 display FFTs of rotor motion (drive end, horizontal and vertical planes) for three increasing supply pressures. The figures evidence a notable reduction in subsynchronous motion amplitudes when increasing the air feed pressure. For the highest supply pressure (340 kPa), the main subsynchronous frequency, *WFR*~0.5, splits or bifurcates into two other frequencies, below and above the original value. The spectra for the highest feed pressures are rather broad, indicating a more “rugged” subsynchronous motion, albeit with less amplitude.

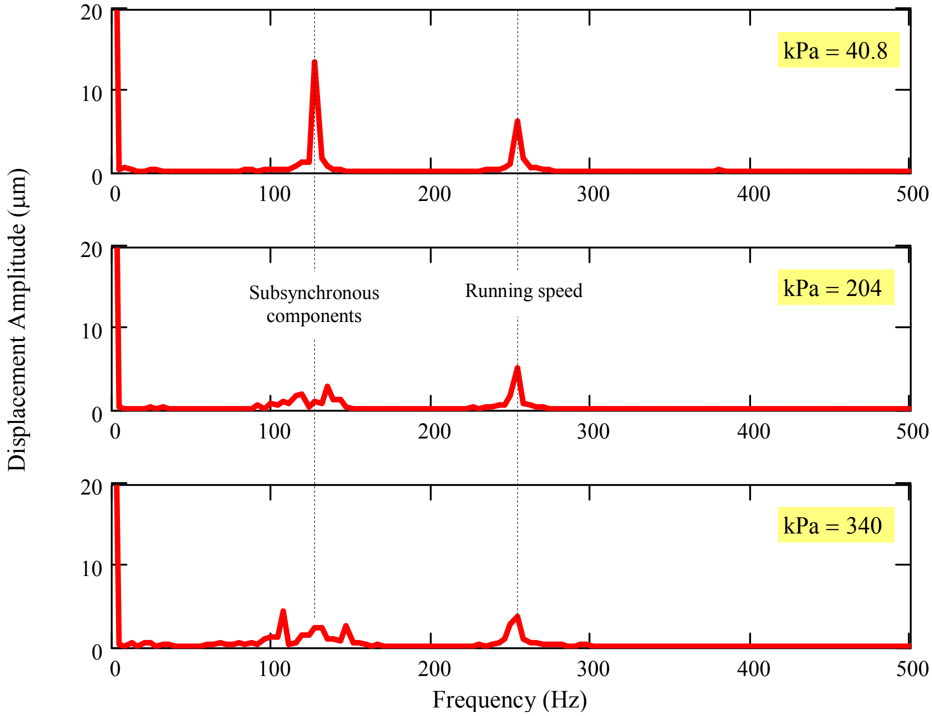

Figure IV-27 FFTs of steady state time responses at 15,200 rpm for three increasing air supply pressures; 40.8 kPa, 204 kPa and 340 kPa. Measurements taken at the drive end, horizontal direction (X_{DE})

Incidentally, the axial flow rate induced by the feed pressure could lead to reductions on the circumferential flow development along the bearing. This phenomenon decreases cross-coupled stiffness, thus favoring rotor stability. A comparison of the axial and circumferential fluid inertia properties is conducted to investigate this phenomenon.

The Reynolds number, a measure of the importance of fluid inertia forces relative to viscous forces, in a thin film bearing, is given by

$$Re_C = \frac{\rho \cdot \Omega \cdot R \cdot c}{\mu_V} \tag{4}$$

where, ρ and μ_V are the lubricant density and viscosity, R is the bearing radius, c is the bearing clearance and Ω is the shaft speed in radian per second.

For a clearance of c = 45 μm (drive end bearing) and shaft speed of 15,000 rpm (one showing severe subsynchronous vibrations), the circumferential flow Reynolds number is $Re_C = 103$. The modified Reynolds number (Re_c^*) for the fluid film bearing is $Re_C^* = Re_C \frac{c}{R} = 0.30$. The calculated modified Reynolds number indicates laminar flow along the circumferential direction and also negligible fluid inertia effects. The influence of the axial flow on the circumferential flow development is determined from a simple analysis based on laminar flow and journal centered operation. Appendix G details the procedure to determine mass flow rate, exit axial flow velocity and Reynolds number for the axial flow. Table IV-3 shows the calculated axial flow characteristics for the different test supply pressures.

Table IV-3 Calculated mass flow rate, mean velocity and Reynolds number for the axial bearing flow

Pressure Ratio P_s / P_a	Pressure Drop ΔP, [kPa]	Mass Flow Rate, $\dot{m}_z$, [g/s]	[LPM]	Total Flow Velocity V_z, [m/s]	Axial flow Reynolds Number, Re_A
1.4	40	0.07	3.7	11.5	32.6
2.4	136	0.36	18.4	57.1	161.8
3.0	204	0.61	31.0	95.9	272.0
3.7	272	0.96	49.2	152.2	431.4
4.4	340	1.39	71.2	220.2	624.2

Interestingly enough, as the pressure supply increases, the axial flow Reynolds number exceeds the circumferential flow Reynolds number of $Re_C = 103$, calculated at a rated speed of 15,000 rpm. Experimental results show that subsynchronous vibrations are significantly reduced for a feed pressure of 204 kPa, see Figure IV-27 and Figure IV-28. For higher feed pressures, the level of subsynchronous vibration reduction remains unchanged, indicating that there is no need of providing larger feed pressures to achieve substantial reductions in subsynchronous vibrations. From test results, the feed pressure needed to substantially reduced subsynchronous vibrations is 204 kPa (pressure ratio = 3). At this feed pressure, Table IV-3 indicates that the axial flow Reynolds number is approximately three times larger than that in the circumferential direction. Therefore, the axial flow rate induced by the side feed pressure affects significantly the circumferential flow development, thus reducing cross-coupled stiffness and favoring rotor stability.

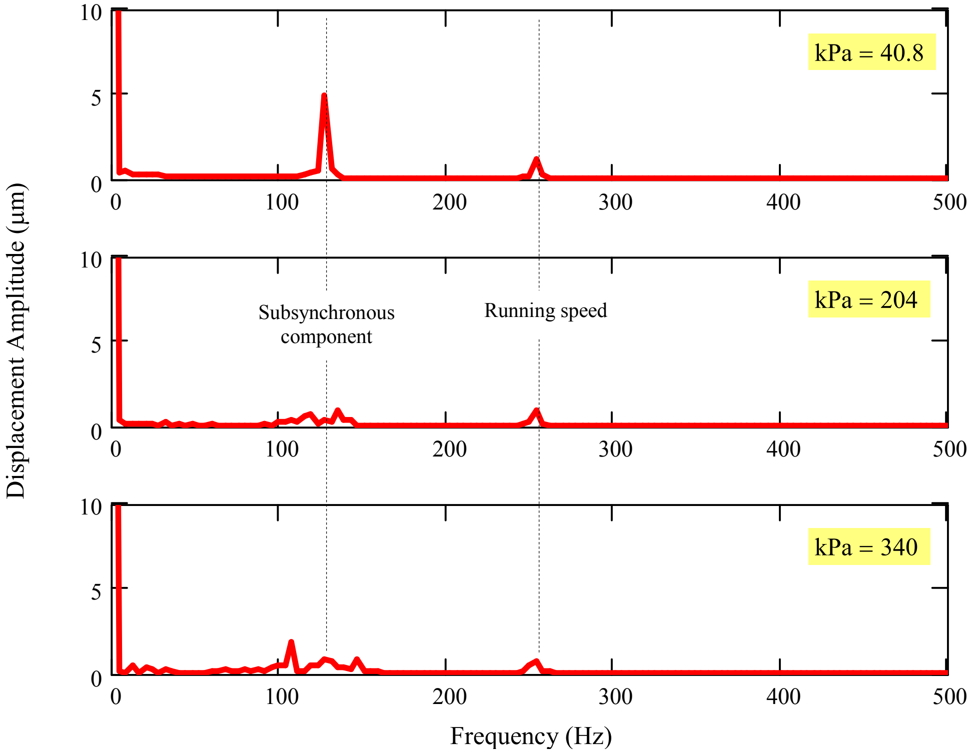

Figure IV-28 FFTs of steady state time responses at 15,200 rpm for three increasing air supply pressures; 40.8 kPa, 204 kPa and 340 kPa. Measurements taken at the drive end, vertical direction (Y_{DE})

Time for Rotor to Coastdown

Figure IV-29 presents coastdown tests of rotor speed versus time for increasing air feed pressures. The imbalance condition corresponds to baseline. No major differences in the coastdown speed are noticeable when increasing the air pressure. However, two distinctive regions of exponential and linear decay are distinctive. An exponential approximation to the speed versus time curve, from 25,000 rpm to approximately 7,000 rpm, renders a goodness of correlation of 99.5%. Similarly, a linear approximation from 5,000 rpm to the minimum speed (~ 1,500 rpm) leads to a goodness of correlation of 99.6%. Thus, in the first region, the bearing drag is of viscous-type, while in the second region Coulomb-type (dry friction) from the contact between the journal and the foil dominates the bearing drag. In the transition region, the foil bearing touchdown speed occurs, as depicted in Figure IV-29.

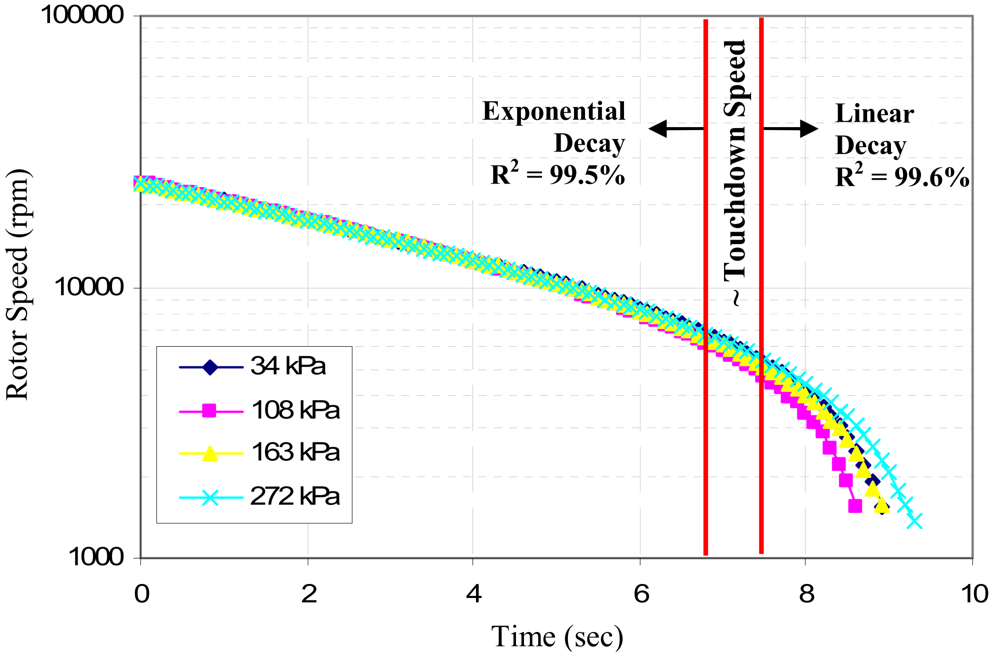

Figure IV-29 Coastdown speed versus time for rotor baseline condition and increasing air feed pressures. Logarithmic scale

In general, the coastdown time (~9 sec) is rather small. However, one must also realize that the drive DC motor remains coupled to the test rotor. Thus, the total coastdown time represents that of the rotor and motor combined. The DC motor coastdown time is approximately 5 seconds, thus greatly influencing in the rapid coastdown time of the rotor and motor combined. This indicates that most of the drag comes from the motor.

Damping Ratios

The *Q* factor method allows estimating equivalent the viscous damping ratio (ξ) by using the peak of the amplitude response at the critical speed from the coastdown synchronous tests[14]. The viscous damping ratios, a measure of the rotor/bearing system damping, are calculated in the horizontal and vertical directions at the measurement plane locations.

$$\xi = \frac{1}{2Q}$$

where, (5)

$$Q = \frac{N_n}{N_2 - N_1}$$

Equation (5) shows the formulae used to calculate the damping ratios and Figure IV-30 defines the notation used for estimating system viscous damping ratio. Presently, synchronous responses with baseline subtraction are used to calculate the system viscous damping ratio. Table IV-4 summarizes the damping ratios determined from the synchronous coastdown responses at the measurement planes locations for imbalance test conditions.

---

[14] The Q factor method is valid for system with relatively small damping (less than 10%) since the natural frequency is equal to the critical speed.

Table IV-4 Damping ratios of rotor/bearing system obtained from synchronous coastdown responses

Location		Imbalance Condition	Critical Speed (rpm)	Q factor	Damping ratio (ξ)
Imbalance condition A1 and B1					
Drive end	X_{DE}	in phase	8,590	6.13	0.08
		out of phase	7,580	2.71	0.18
	Y_{DE}	in phase	8,390	5.98	0.09
		out of phase	8,390	2.09	0.24
Free End	X_{FE}	in phase	9,910	2.69	0.19
		out of phase	-	-	-
	Y_{FE}	in phase	8,780	3.05	0.16
		out of phase	8,780	2.91	0.17
Imbalance condition A2 and B2					
Drive end	X_{DE}	in phase	8,190	5.89	0.08
		out of phase	8,180	4.07	0.12
	Y_{DE}	in phase	7,990	5.7	0.08
		out of phase	8,390	2.97	0.16
Free End	X_{FE}	in phase	8,190	2.91	0.17
		out of phase	-	-	-
	Y_{FE}	in phase	8,190	4.57	0.19
		out of phase	8,990	2.45	0.21
Imbalance condition A3 and B3					
Drive end	X_{DE}	in phase	8,540	5.58	0.09
		out of phase	7,590	3.83	0.13
	Y_{DE}	in phase	8,390	4.76	0.10
		out of phase	8,190	2.55	0.19
Free End	X_{FE}	in phase	8,390	5.45	0.09
		out of phase	-	-	-
	Y_{FE}	in phase	8,390	4.87	0.10
		out of phase	8,390	2.97	0.18

X: horizontal, Y: vertical

Note that ξ is not given at the free end bearing location (out of phase imbalance) because a peak in amplitude is not evident. At all other measurement planes, the calculated damping ratios for the out-of-phase imbalances are generally larger than those estimated with in-phase imbalances. Damping ratios at the horizontal direction are slightly smaller than those in the vertical directions at both measurement planes. In general, the calculated damping ratios range from 0.08 to 0.19, except for two imbalance conditions where ξ is larger than 0.20.

The test responses used for estimating damping ratios are obtained for a supply pressure of 40 kPa [6 psig]. In general, for all imbalance conditions, damping ratios at all bearing locations are approximately 10% of the critical damping, thus slightly exceeding the criterion for the Q factor method.

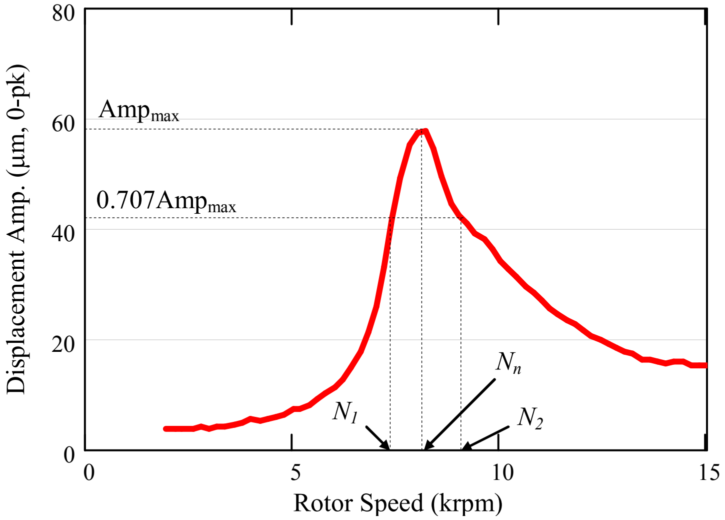

Figure IV-30 Notation for estimating system viscous damping ratio using the Q factor method

CHAPTER V

ROTORDYNAMIC ANALYSIS OF TEST ROTOR SUPPORTED ON GAS FOIL BEARINGS – PREDICTIONS VERSUS EXPERIMENTAL RESULTS

The rotordynamic analysis consists of modeling the test rotor with XLTRC^2® rotordynamic software developed in the Turbomachinery Laboratory at Texas A&M University. A computational code, developed by Kim and San Andrés [35], solves the Reynolds equation for a thin gas film coupled to a simple elastic foundation model for the bump foil strip. The program calculates the equilibrium pressure profile which is then used to obtain bearing force coefficients as a function of the whirl frequency and the journal operating speed. The test rotor model and the predicted bearing force coefficients allows performing a stability analysis which includes examination of damped natural frequencies, stability map, threshold speeds and vibration modes. Synchronous rotor responses to imbalance are predicted and then compared to experimental responses.

Predicted Bearing Performance

The predicted foil bearing performance is described through a computational program which accounts for the hydrodynamic and elastic foundation interaction [35]. The simple model predicts the static and dynamic force characteristics upon selection of major bearing features, i.e. acting static load, bump geometry, bearing clearances and structural loss factor. The model uses an axially averaged hydrodynamic pressure to calculate the structural bump deflection. For dynamic analysis of a gas bearing, the journal is perturbed about an equilibrium position, determined by the static load. Applying these perturbations to the gas film Reynolds equation defines the equilibrium and perturbed pressure fields within the lubricant film, from which stiffness and damping force coefficients are extracted. The programs accounts for the nonlinearity behavior of the overall bearing stiffness which depends on the applied load and assembly preload [8].

Figure V-1 shows the coordinate system for analysis of gas foil bearing performance. The spot weld angular location is noted. The static load is applied along the negative Y axis in order to provide consistency with the coordinate systems later used in the rotordynamic analysis.

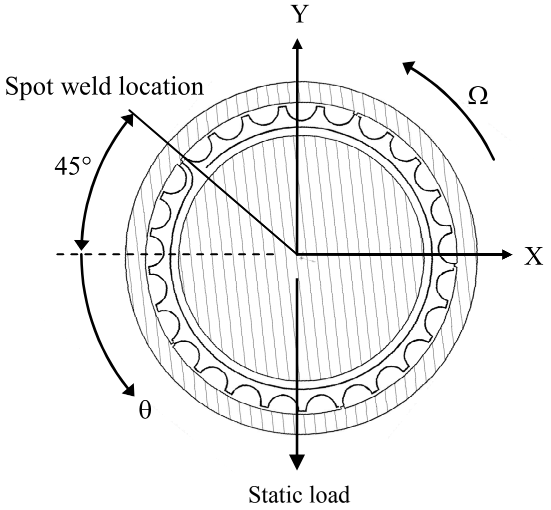

Figure V-1 Coordinate systems for analysis of gas foil bearing performance

Table V-1 lists the test bearing geometry while Table V-2 details the physical operating conditions of the rotor/bearing system. Notice that the foil detach option is disabled (no detach), thus allowing for sub-ambient pressures. Currently, the program does not allow for assembly preload larger than the selected bearing clearance, i.e. no interference between bearing and journal. The radial bearing clearances and acting static bearing loads corresponds with the estimation given in Table IV-1, see page 34.

Table V-1 Geometry for analysis of gas bearing performance

Physical Properties	*Value*
Rotor diameter (mm)	38.10
Axial Length (mm)	38.10
Bump stiffness (mm)	3.17×10^9
Top foil arc length (deg)	350
Spot weld location (deg)	-45
Structural loss factor	0.05
Foil bearing detach	No detach
Bearing preload	0
Drive end FB radial clearance (μm)	50
Free end FB radial clearance (μm)	45
Static load drive end bearing (N)	4.5
Static load free end bearing (N)	4.2

Table V-2 Operating conditions for analysis of gas bearing performance

Operation conditions	*Value*
Ambient pressure (bar)	1.013
Supply temperature (°C)	26.7
Viscosity at ambient pressure, μ_V (c-Poise)	0.0187
Density at ambient pressure, ρ (kg/m3)	1.22

The computational model uses 91 circumferential nodes and 11 axial nodes to represent the complete bearing. The equilibrium and perturbed pressure fields are numerically iterated until a convergence tolerance of 10^{-5} is satisfied between consecutive iterations in pressure fields. The program determines the pressure profile and mass flow rate of the lubricant for a range of structural loss factors and operating speeds.

Journal Eccentricity and Attitude Angle

The foil bearing static equilibrium of the test bearing performance is predicted for static load conditions and bearing clearances detailed in Table IV-1. The selection of the structural loss factor coefficient (γ) is based on the acting static bearing load. Rubio and San Andrés [35] report structural loss factor coefficients which are constant with excitation frequency and increases with applied load. For the static load conditions of the test foil bearings, the corresponding structural loss factor is selected as $\gamma = 0.05$.

Figure V-2 displays the predicted journal eccentricity ratios versus rotational speed for static load conditions which resemble the load conditions for the test foil bearings, i.e. 4.2 N for the drive end bearing and 4.5 N for the free end bearing. As the rotational speed increases the eccentricity ratio (e/c) decreases, thus the journal approaches the bearing center position. Notice that for the levels of static load on the test bearings, the journal eccentricities do not exceed the bearing clearance ($e/c < 1$). Predictions of journal eccentricities for more severe static load are shown in [34], and evidencing journal excursions larger than the bearing nominal clearance.

The attitude angle is defined as the angle between the direction of static load and the journal eccentricity vector. Figure V-3 depicts the predicted journal attitude angle for the two load bearing conditions. The attitude angle approaches 90 degrees for both foil bearings, favoring hydrodynamic instability. Overall, both foil bearings present a similar static performance.

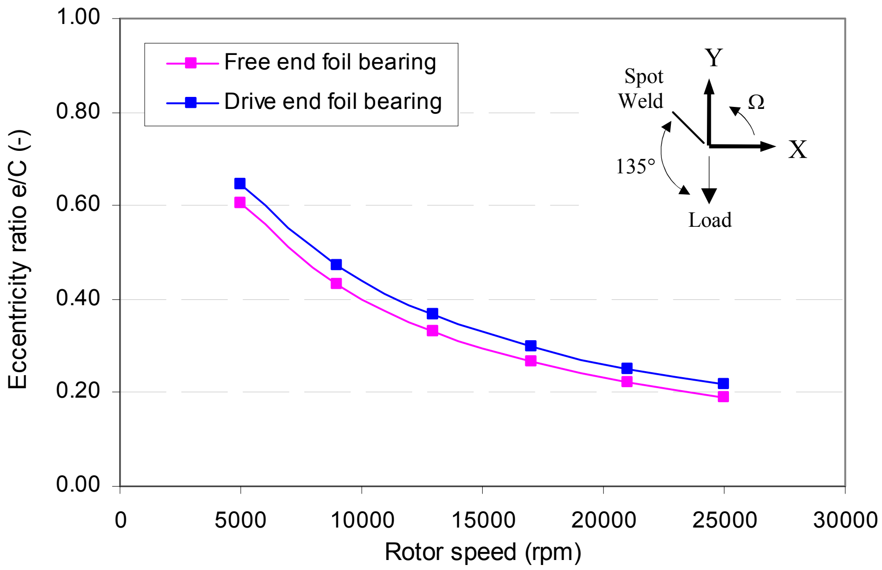

Drive end FB
$F_X = 0$
$F_Y = -4.2$ N
$c = 50$ µm
$\gamma = 0.05$

Free end FB
$F_X = 0$
$F_Y = -4.5$ N
$c = 45$ µm
$\gamma = 0.05$

Figure V-2 Predicted journal eccentricity ratios versus rotational speed. Drive end FB static load = 4.2 N and free end FB static load = 4.5 N

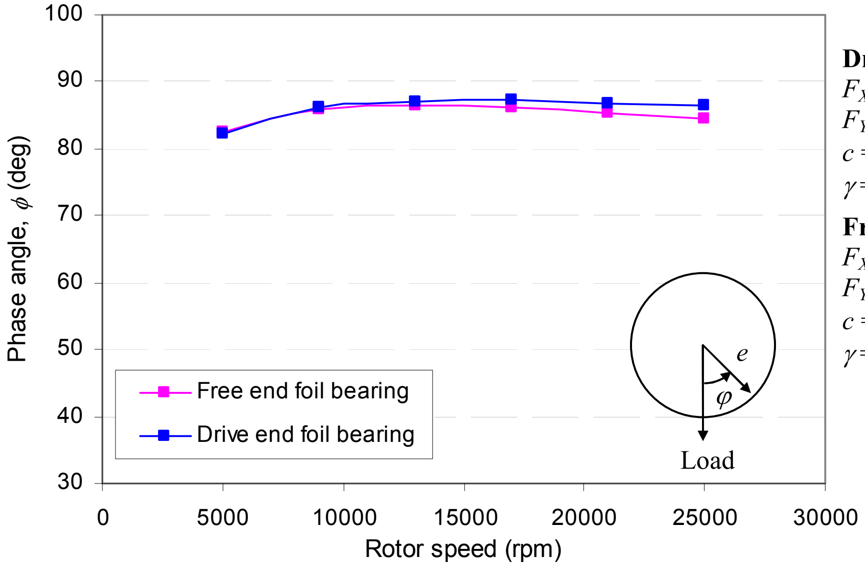

Drive end FB
$F_X = 0$
$F_Y = -4.2$ N
$c = 50$ µm
$\gamma = 0.05$

Free end FB
$F_X = 0$
$F_Y = -4.5$ N
$c = 45$ µm
$\gamma = 0.05$

Figure V-3 Predicted attitude angle versus rotational speed. Drive end FB static load = 4.2 N and free end FB static load = 4.5 N

The role of the nominal clearance is crucial in the performance of foil bearings. Radil et. al [31] explain that foil bearings have an optimum radial clearance that produces a maximum load capacity. Relative to the optimum clearance there are two distinct regimes, i.e. heavily and lightly preloaded zones. Figure V-4 illustrates the effect of bearing clearance and rotational speed on the predicted minimum gas film thickness for a static load condition of 4.2 N (drive end bearing). The clearance ratio (c^*/c) refers to a percent of the reference bearing clearance (c = 50 μm for the drive end bearing).

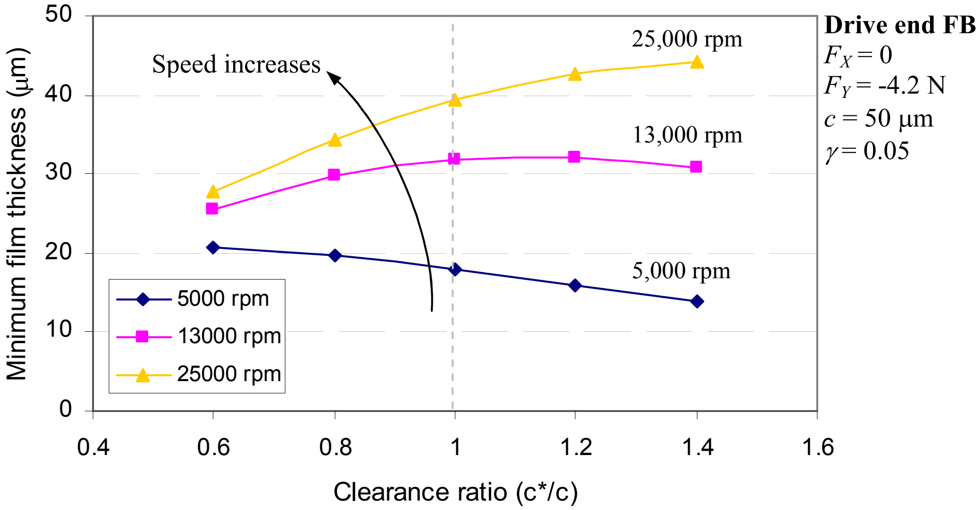

Figure V-4 Predicted minimum film thickness versus a percent of the measured drive end bearing clearance (c = 50 μm). Load fixed at 4.2 N

At a rated static load condition of 4.2 N and low rotational speeds, the minimum film thickness must be small to generate the fluid film reaction force balancing the static load. As the rotational speed increases, the required minimum gas film thickness increases as well[15]. On the other hand, the bearing clearance clearly affects the foil

---

[15] In general, the fluid film reaction force (W_n) is proportional to the rotor speed (Ω) and inversely proportional to the square of the minimum film thickness (h_{min}), i.e. $W_n = \mu_V \, \Omega / (h_{\min})^2$

bearing static load capacity. At low speeds, an increase in bearing clearance leads to smaller minimum gas film thicknesses. Conversely, at higher speeds the gas film thickness increases as the bearing clearance increases.

Figure V-5 shows the predicted drag torque for different bearing clearance ratios. At low shaft speeds, the influence of the bearing clearance on the predicted drag torque is minimal since the shearing forces, due to shaft spinning, are not significant[16]. Once the rotational speed increases, the drag bearing torque augments due to an increment on the velocity gradient along the air film thickness. At high speeds, the drag bearing torque is also greatly affected by the bearing clearance. As shown in Figure V-4, at high speed and low bearing clearances, the minimum film thickness is small, thus leading to larger drag torques. As the clearance increases for a rated high speed, the drag torque decreases due to an increase in the film thickness.

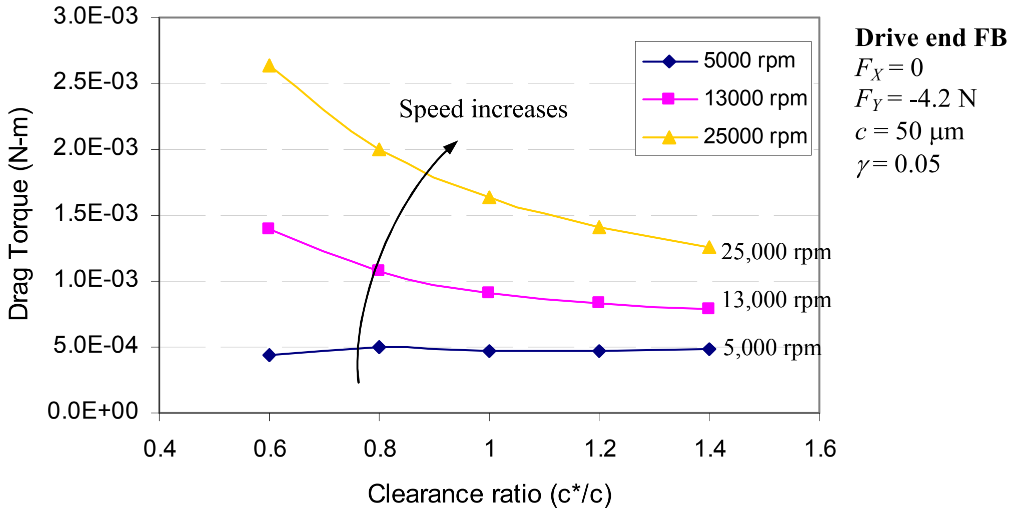

Figure V-5 Predicted drag torque versus a percent of the measured drive end bearing clearance ($c = 50$ μm). Load fixed at 4.2 N

---

[16] The torque drag (T_D) increases linearly with speed and is inversely proportional to the minimal film thickness, i.e. $T_D = \mu_V \Omega / h_{\min}$

Predicted Bearing Force Coefficients

Figure V-6 through Figure V-9 depict the predicted synchronous stiffness and damping (direct and cross-coupled) force coefficients as a function of rotor speed for the two bearing load conditions and loss factor $\gamma = 0.05$. Recall that the selection of the structural loss factor coefficient (γ) is based on the acting static bearing load [36]. Figure V-6 and Figure V-7 shows predicted stiffness (direct and cross-coupled) for both bearing load conditions. In general, the direct stiffness coefficients (K_{xx} and K_{yy}) increase with rotor speed. The free end bearing, carrying a little more load than the drive end bearing, presents slightly larger direct stiffness coefficients than those for the drive end bearing. Recall than the foil bearing elastic structure has a stiffening effect when increasing the applied static load. Cross-coupled stiffness force coefficients slightly increase with rotor speed, with magnitudes comparable to those of the direct stiffness force coefficients. These coefficients may eventually lead to rotordynamic instability.

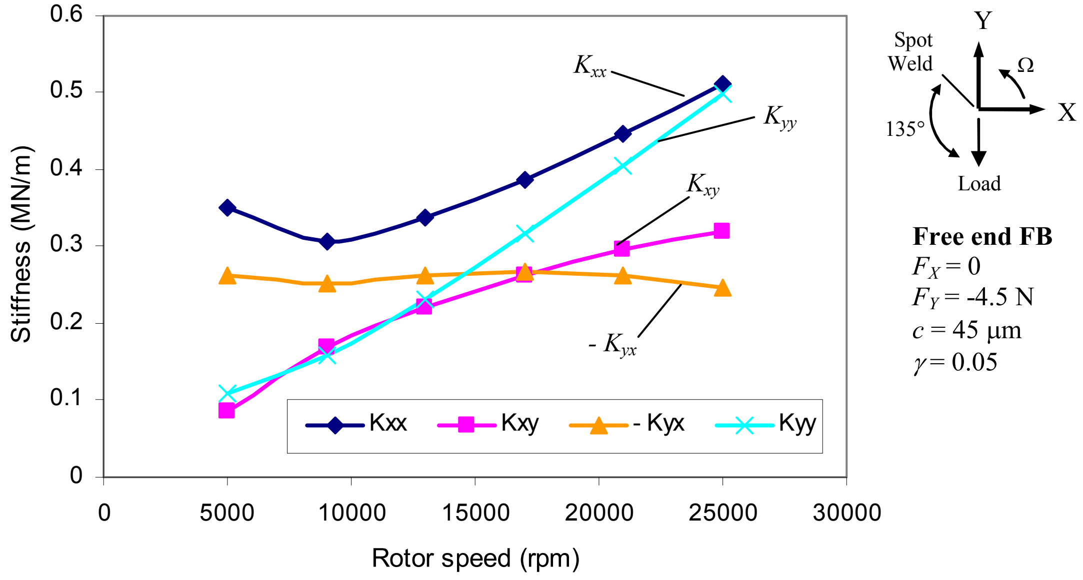

Figure V-6 Predicted synchronous stiffness coefficients for free end foil bearing. Radial clearance of 45 μm and static load 4.5 N

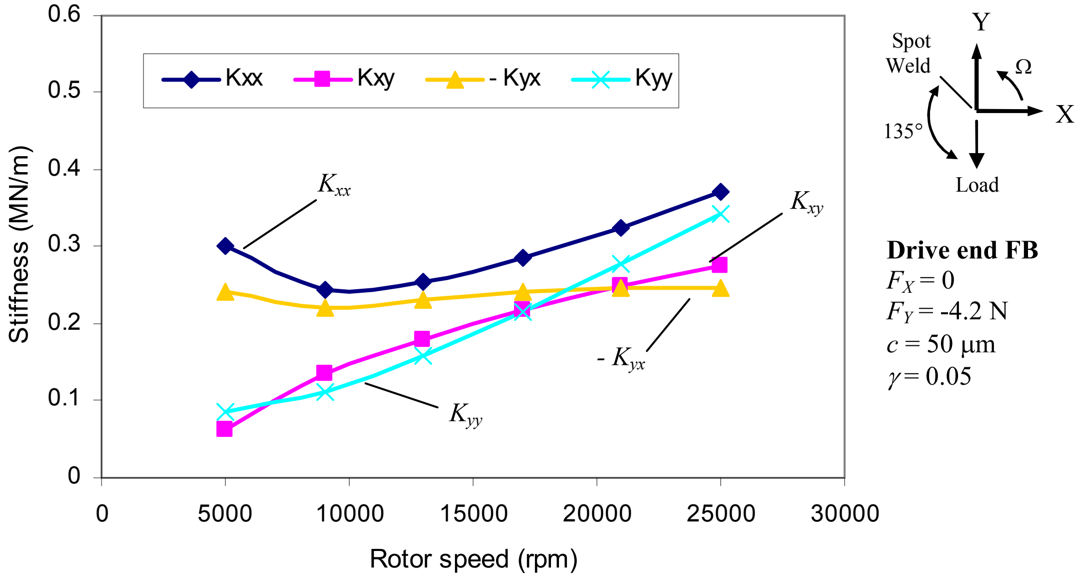

Figure V-7 Predicted synchronous stiffness coefficients for drive end foil bearing. Radial clearance of 50 μm and static load 4.2 N

Figure V-8 and Figure V-9 depicts predicted <u>synchronous</u> damping coefficients (direct and cross-coupled) for both bearing load conditions Synchronous damping coefficients presented herein are determined with a structural loss factor (γ) of 0.05. See reference [34], for more details on the effect of structural loss factor on the frequency dependency of damping force coefficients.

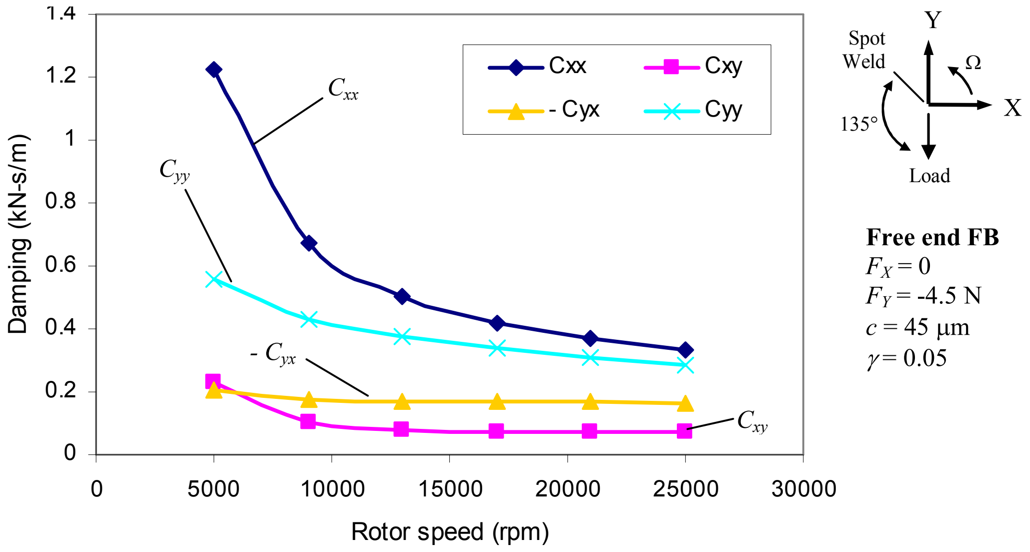

Figure V-8 Predicted synchronous damping force coefficients for free end foil bearing. Radial clearance of 45 μm and static load 4.5 N

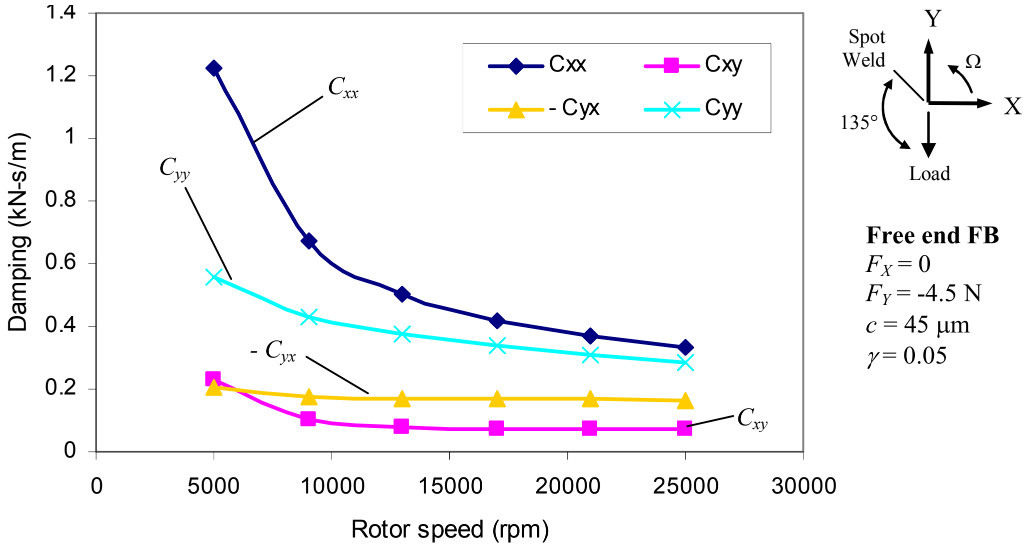

Figure V-9 Predicted synchronous damping force coefficients for drive end foil bearing. Radial clearance of 50 μm and static load 4.2 N

At low shaft speeds, the minimum gas film thickness is small, thus leading to large direct synchronous damping coefficients. As the shaft speed increases (minimum gas film increases), direct damping coefficients decrease. It is important to notice that such behavior at low speeds is due to the nature of the equivalent viscous damping which increases with minimum gas film thickness. The effect of structural loss factor on the direct synchronous damping coefficients is small, less than 5% when varying γ from 0.0 to 0.4 for the lowest shaft speed.

Kim and San Andrés [35] show that frequency dependant damping coefficients are largely affected by the structural loss factor for static loads larger than ~ 50 N, thus affecting also synchronous damping coefficients (especially at low shaft speeds). However, the static load levels supported by the test foil bearing (~ 4 N) are considerably lower, therefore not affecting the predicted synchronous direct damping for the test foil bearings.

Predicted Rotor/Bearing Performance

The test rotor/bearing system is modeled using XLTRC^2 rotordynamic software. The input parameters for the software are the geometrical and material features of the test rotor and the predicted bearing force coefficients. Figure V-10 shows the multiple station test rotor model in XLTRC^2. A two layer section, from stations 1 to 6, represents the connecting shaft while the flexible coupling is modeled with an added mass and inertia. The support bearings are added at the appropriate physical locations and a coupling stiffness is added at station 1[17].

---

[17] The flexible coupling lateral stiffness is identified statically through load versus deflection tests. The identified coupling lateral stiffness is 0.16 MN/m, of the same order of magnitude as the test gas foil bearings.

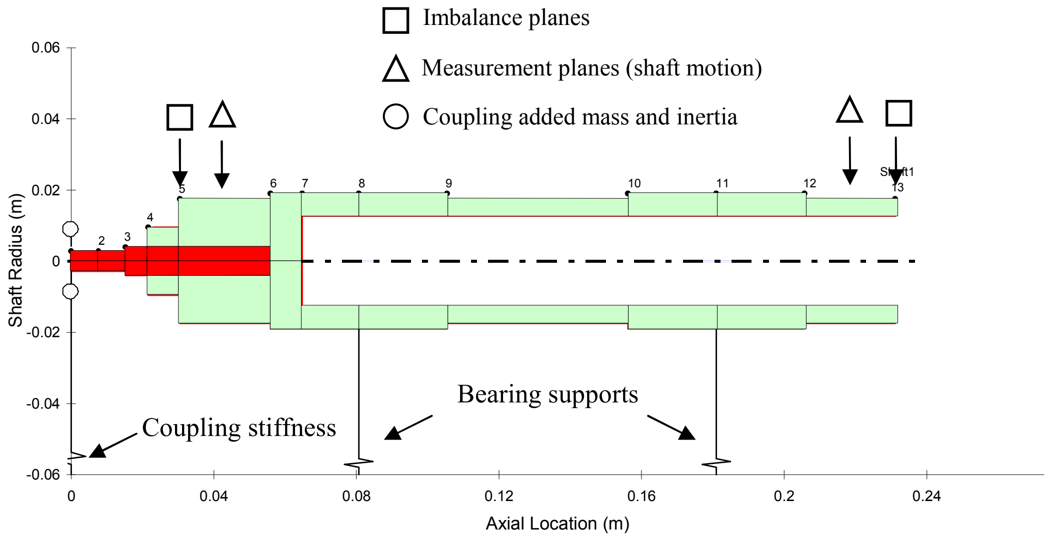

Figure V-10 Finite element model of test rotor (with connecting shaft and flexible coupling included)

A calibration of the rotor structural model is conducted by comparing predictions to experimental rap tests[18] results evidencing free-free mode shapes. The rap tests are conducting with three rotor configurations, i.e. rotor with connecting shaft and flexible coupling, rotor with connecting shaft alone, and rotor alone. Table V-3 lists the measured and predicted free-free mode frequencies for each of the rotor configurations. Experimental results and predictions of the three free-free natural frequencies are within 3% of error for all cases.

The addition of the connecting shaft and flexible coupling reduces significantly the first two free-free natural frequencies. However, these frequencies are still above the maximum speed of test rig operation. Notice that the second free-free natural frequency of the rotor without the connecting shaft and flexible coupling are similar to the third free-free natural frequencies for the other two rotor configurations. The addition of the

---

[18] The rap test consists of hanging the rotor and rapping it with an impact hammer. Then, the amplitude of the relative motion between a stationary and roaming accelerometer, positioned along the rotor axial length, shows the bending natural frequencies and mode shapes.

connecting shaft and flexible coupling to the test rotor causes the appearance of an additional free-free natural frequency. Figure V-11 makes clear the cause of the addition free-free mode natural frequency when presenting predictions and experimental results of the mode shapes for the test rotor with the connecting shaft and flexible coupling. Notice that the connecting shaft flexibility leads to two distinctive mode shapes for the first two free-free natural frequencies, i.e. bending shapes of test rotor and connecting shaft in phase and out phase. The bending shapes of the rotor alone remain fairly unchanged for the first two free-free natural frequencies.

Table V-3 Measured and predicted bending mode frequencies

Mode frequencies		Rotor with connecting shaft and coupling	Rotor with connecting shaft alone	Rotor without connecting shaft and coupling
First	Measured*	3008 Hz	3968 Hz	4096 Hz
	Predictions	3086 Hz	3826 Hz	4100 Hz
Second	Measured*	4065 Hz	4736 Hz	9856 Hz
	Predictions	4125 Hz	4722 Hz	9851 Hz
Third	Measured*	9760 Hz	9760 Hz	Not recorded
	Predictions	9447 Hz	9543 Hz	

*Uncertainty of the measured free-free mode natural frequencies ± 127 Hz

In general, the mode shapes correlations are quite satisfactory. Notice that experimental results of mode shapes are not measured at the connecting shaft locations because the accelerometer mass, when positioned in the connecting shaft, affected the readings of the free-free natural frequencies and rotor acceleration amplitudes. Therefore, in order to provide a consistent correlation between experiments and predictions, the normalized amplitudes are obtained with respect to the maximum amplitude along the rotor axial length, i.e. stations 4 through 13. Appendix H shows mode shapes for the other two rotor configurations.

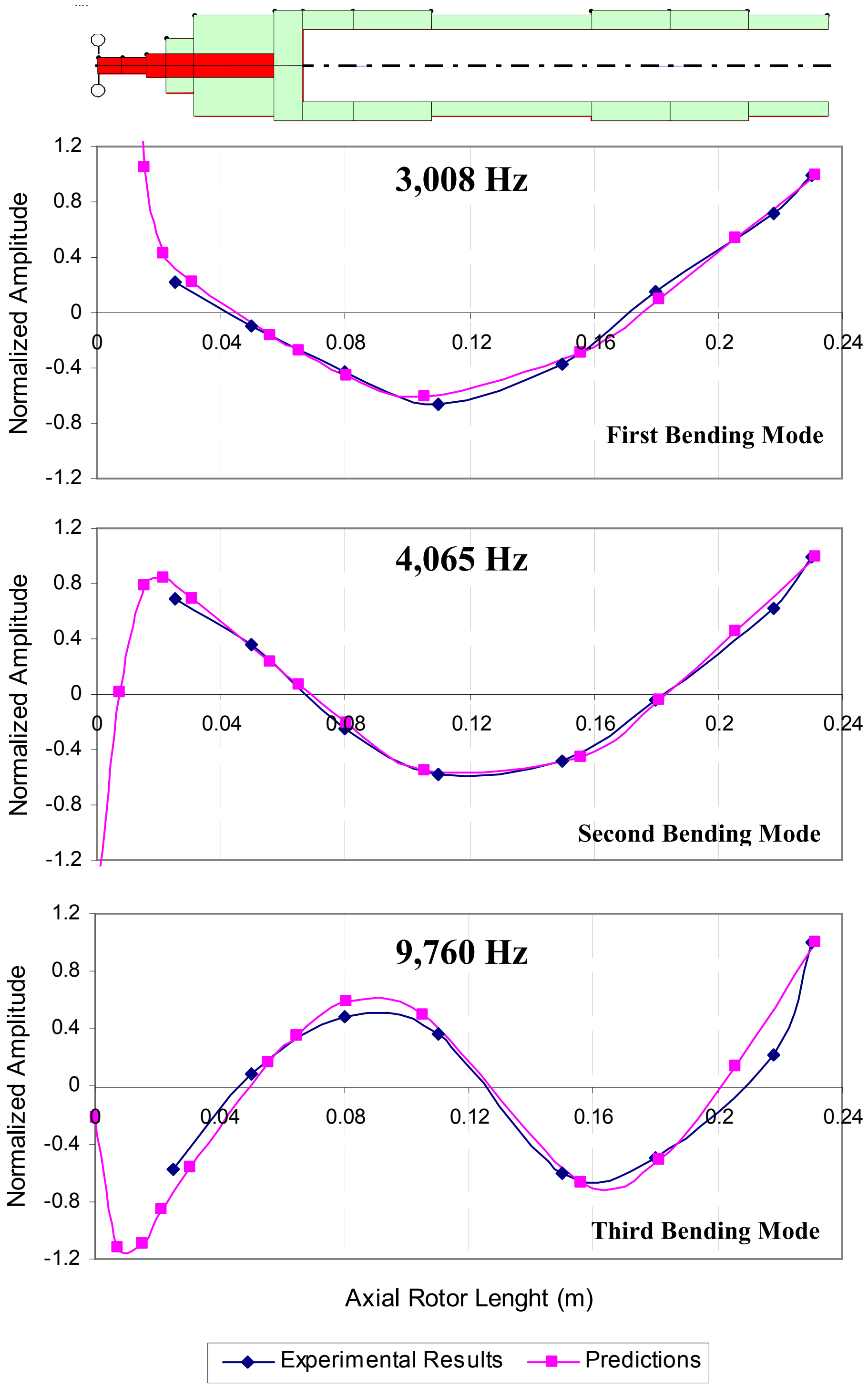

Figure V-11 Measured and predicted free-free mode shapes of test rotor with the connecting shaft and flexible coupling

Damped Natural Frequencies and Damping Ratios

Figure V-12 shows the undamped critical speed map of the test rotor. From experimental results, the critical speeds occur around 8,500 rpm, which requires a range of support stiffness from ~ 0.15 MN/m to ~ 0.7 MN/m. Figure V-6 and Figure V-7 show that the predicted stiffness force coefficients for both foil bearings are within the noted range for the operating speed range (0 to 25,000 rpm). Notice that the natural frequencies for the flexible rotor modes approaches to the free-free mode natural frequencies (Figure V-11) as the bearing stiffness decreases.

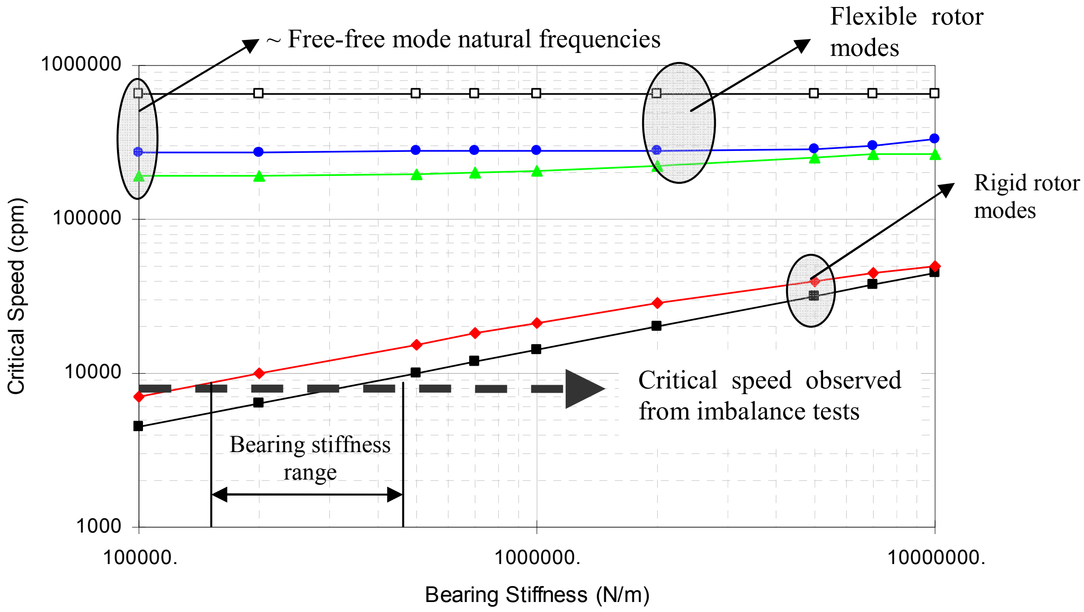

Figure V-12 Undamped critical speed map of the test rotor with the connecting shaft and flexible coupling

An eigenvalue analysis calculates the rotor/bearing system damped natural frequencies and damping ratios over the speed range of 2000 rpm - 25,000 rpm[19]. Figure V-13 shows the damped natural frequency map of the rotor/bearing system. The critical speeds are determined by the intersection of the synchronous frequency line with the damped natural frequencies. The first critical speed is shown at approximately 8,000 rpm while the second one occurs at 9,000 rpm. Both critical speeds are associated with conical mode shapes (see bottom of Figure V-13) as also confirmed by the experimental results.

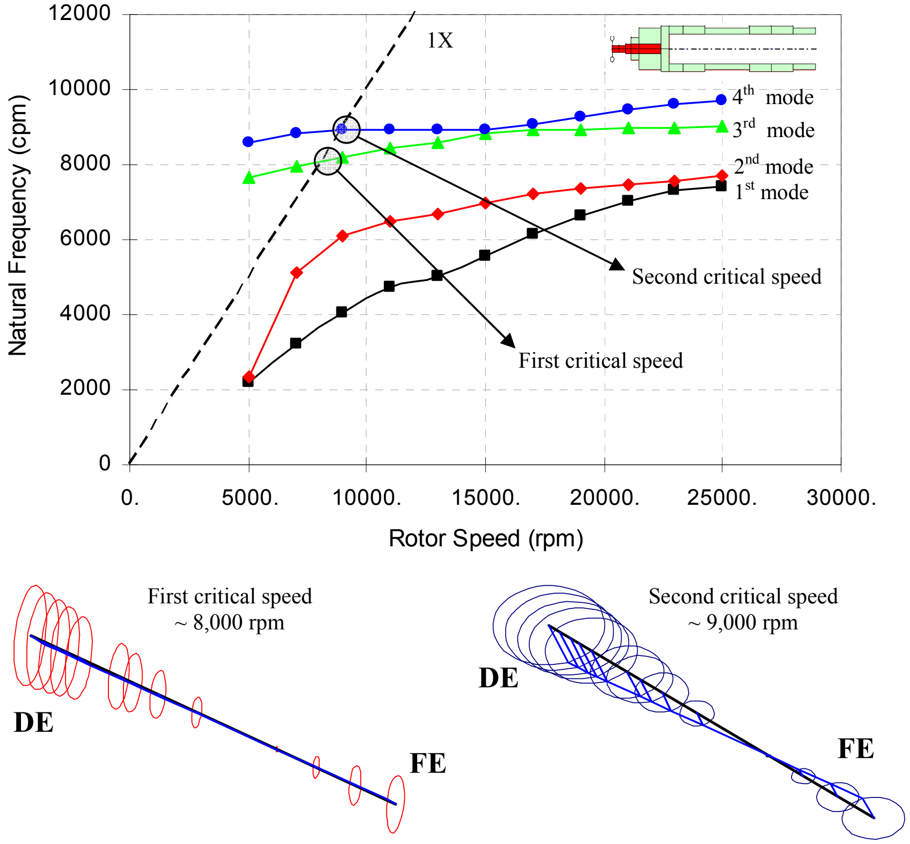

Figure V-13 Damped natural frequency map of the FB rotor/bearing system

---

[19] Synchronous force coefficients were used in the analysis. This is not exactly accurate since *GFB* show force coefficients depending on excitation frequency.

It is important to note that predictions of deflected shapes also show some connecting rod bending within the speed range of operation. Appendix I shows the rotor deflected shapes for an in-phase imbalance condition u = 10.7 μm at four shafts speeds. Connecting rod bending is also predicted for the other imbalance conditions. Therefore, a rigid body motion assumption is not valid to perform foil bearing parameter identification using the test data. In general, rotor bending occurs for all imbalance distributions. Note that rotor bending is predicted for the configuration of test rotor with the connecting shaft and flexible coupling. No rotor bending is predicted when performing rotordynamic analysis of the rotor alone. Therefore, the coupling connection exerts significant forces to the test rotor which leads to its bending for speed ranges of 3,000 rpm to 7,000 rpm.

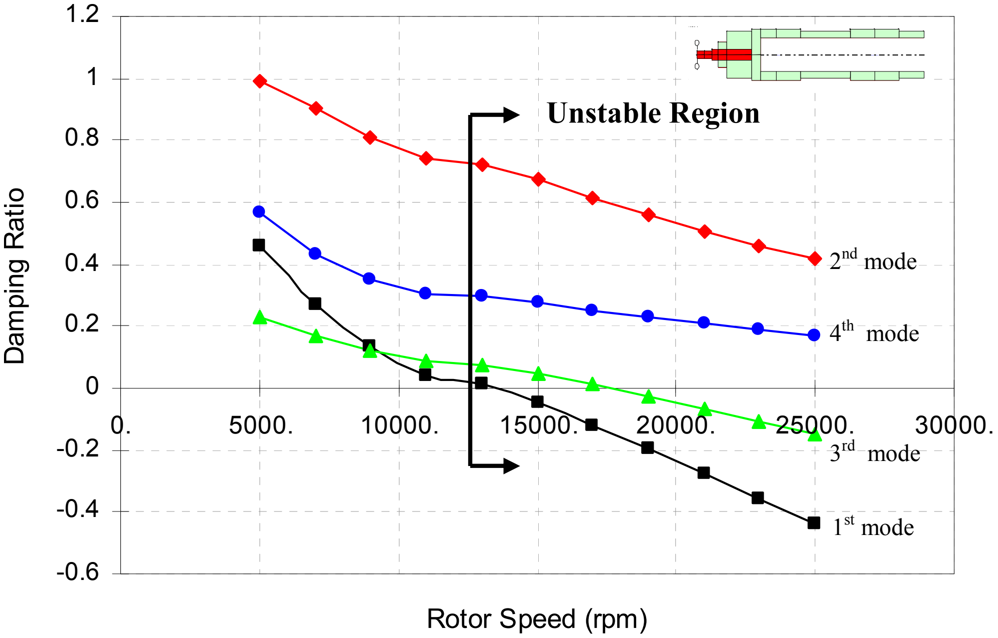

Figure V-14 Predicted rotordynamic stability map of the FB rotor/bearing system

Figure V-14 depicts the damping ratio for the test rotor/bearing system. The eigenanalysis predicts rotordynamic instability starting at 12,500 rpm for the first mode and 17,000 rpm for the second mode. Subsynchronous vibrations continue up to maximum test speed (25,000 rpm) for both modes. The third and fourth modes are stable for the entire speed range. Experimental results also reveal subsynchronous vibrations starting at 12,000 rpm and continuing until reaching ~ 22,000 rpm.

Response to Imbalance: Comparison between Predictions and Experimental Results

Figure V-15 and Figure V-16 show comparisons of experimental synchronous (with baseline subtraction) and predicted responses to imbalance for in phase and out of phase imbalance conditions, respectively. Predictions are obtained for the rotor model which includes the connecting shaft and the flexible coupling and for bearing clearances and static load detailed in Table IV-1. Figure V-15 depicts the predicted and experimental rotor imbalance at the drive end free end measurement planes for an in-phase experimental imbalance displacement of u = 10.51 μm. The predicted imbalance responses are obtained for the same imbalance displacement. Overall, predictions show good critical speed correlation with test values (within 4% of difference). In terms of the response amplitudes, predictions correlate well with experimental results along the horizontal direction (X) at both rotor ends. While the predicted and experimental response amplitudes along the vertical direction (Y) do not correlate well in particular for the rotor free end bearing location.

Similarly, Figure V-16 depicts the predicted and experimental rotor imbalance at the drive end free end measurement planes for an out-of-phase experimental imbalance displacement of u = 7.4 μm. At the rotor free end, predictions show good agreement with test for amplitude and critical speed. At the rotor drive end, predictions are in agreement with experimental results along the vertical direction (Y). Predicted amplitudes along the horizontal direction (X) are significantly larger than those recorded, indicating that predictions of damping coefficients are too low.

In-phase	Imbalance displacement
Experiments	u = 10.51 µm
Predictions	u = 10.51 µm

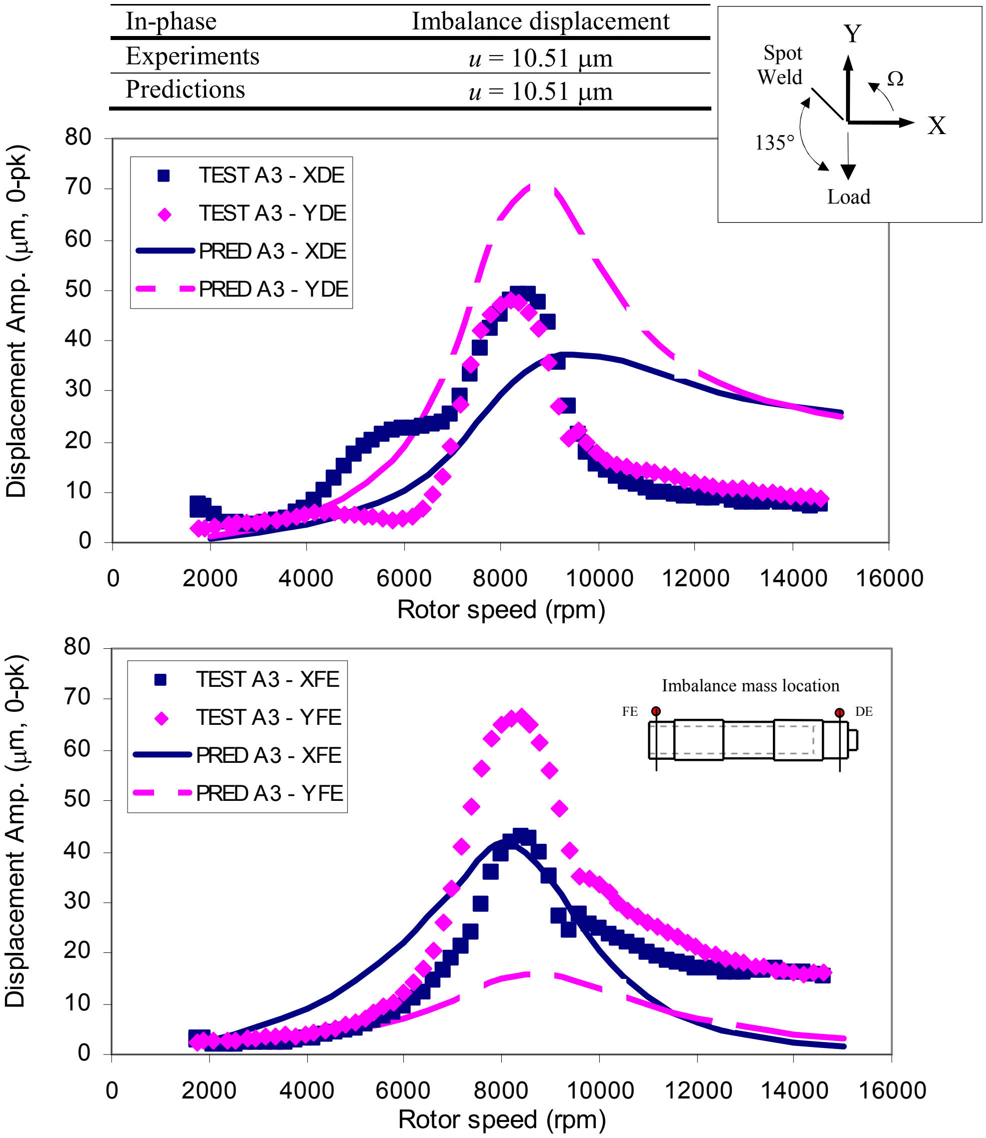

Figure V-15 Predicted and experimental response to imbalance at the drive end and free end location for an imbalance displacement of u = 10.5 µm (in phase, Test A3)

Out-of-phase	Imbalance displacement
Experiments	u = 7.4 μm
Predictions	u = 7.4 μm

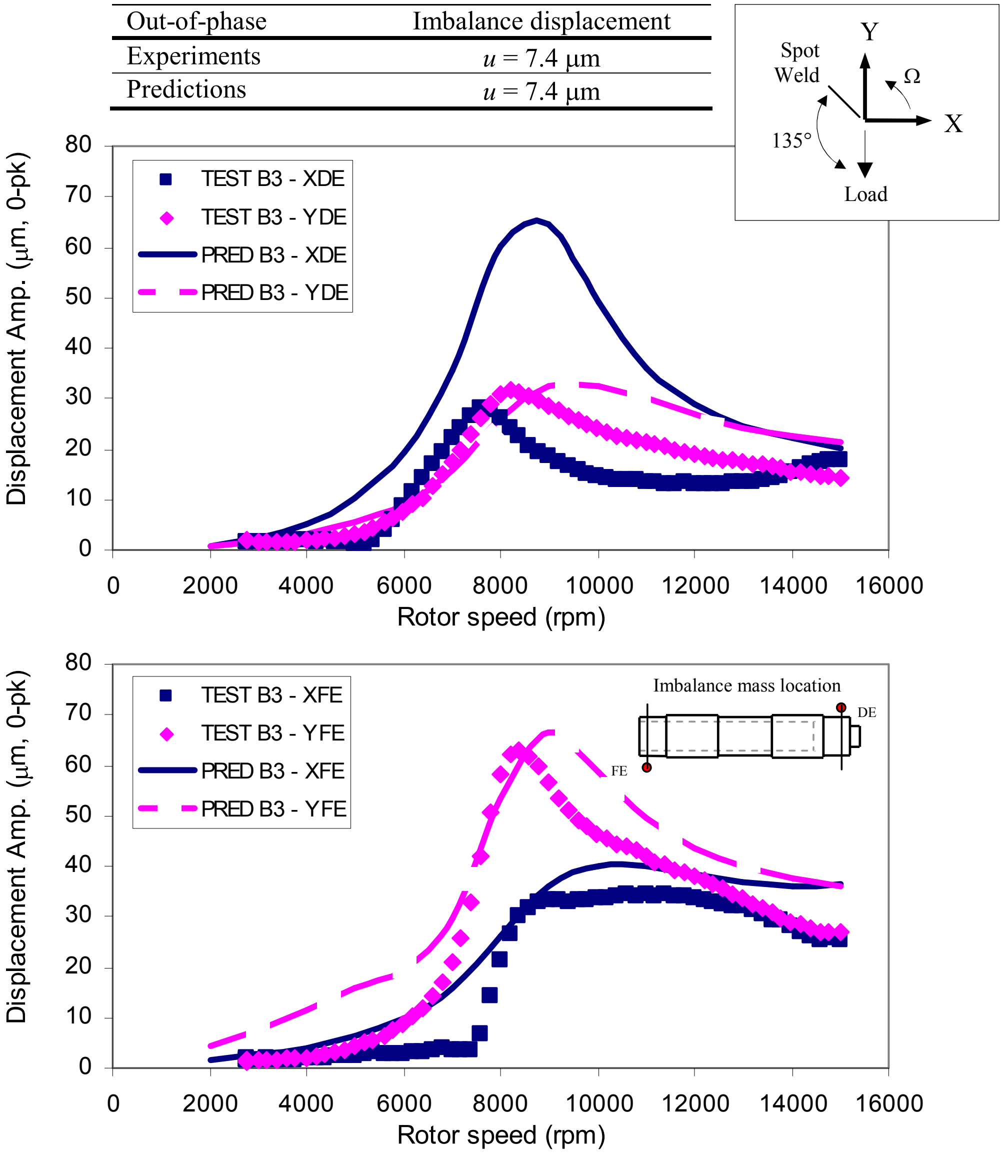

Figure V-16 Predicted and experimental response to imbalance at the drive end and free end location for an imbalance displacement of u = 7.4 μm (out-of-phase, Test B3)

CHAPTER VI

TEST FOIL BEARING AND ROTOR SURFACE CONDITIONS

This chapter examines the final condition of the test rotor and foil bearing surfaces after the exhaustive experimentation. In general, post-test inspection of the rotor evidenced sustained wear at the locations in contact with the bearings, in particular at the edge of the bearings. However, the foil bearings are almost in pristine condition, except for transfer of shaft coating material to the top foils.

Table VI-1 summarizes the material properties of the test rotor and bump foils. The test rotor at the bearing location is coated with a TDC (thin dense chrome) coating, of thickness 25.4 μm. The top foil is coated with a spray-on coating Emralon 333, applied to a thickness of 25.4 μm.

Table VI-1 Test rotor and bump foil material properties

Top foil material properties	SI Units	English Units
Poisson's ratio, υ	0.29	
Bump modulus of elasticity, E_B	213 GPa	31,000 ksi
Test rotor material properties		
Modulus of elasticity, E	193 GPa	28,000 ksi
Material density, ρ_E	7830 kg/m^3	0.282 lb/in^3

Figure VI-1 shows photographs of the test rotor surface before and after the rotordynamic tests. It is evident that the majority of coating wear is at the location of the journal outboard edges. The coating wear is attributed first to rubbing between journal and top foil at rotor start up and coastdown. Predominant conical motions on the test rotor lead to large coating wear at the outboard bearing edges where rotor motions are the largest. The hydrodynamic film pressure drops at the bearing edges (to ambient pressure) may also lead to top foil-journal contact at the journal edges.

Figure VI-2 depicts photographs of the test foil bearing surface after the measurements. The white portions represents the unworn top foil coating of the test foil bearing, while the opaque spots within the white section represents the top foil coating wear. The top foil also evidences more wear at the bearing edges, although a few wear spots are found along the direction of applied static load (~ 135 degrees away from the spot weld) and also near the spot weld line.

Figure VI-1 Test rotor surface condition before and after rotordynamic experiments

Table VI-2 shows measurements of bearing diameters before and after the measurements. The bearing diameters are measured at three axial planes along the axial bearing length; outboard edge, middle plane and inboard edge. The angular orientation where the diameter is measured coincides with the static load direction. The reported bearing diameters are obtained from an average of five measurements. After conducting the experiments, the bearing inner diameter increases for both the measurement planes, especially at the outboard edges for both bearings. At the inboard and outboard locations the bearing diameter has increased approximately 0.05 mm and 0.03 mm, respectively.

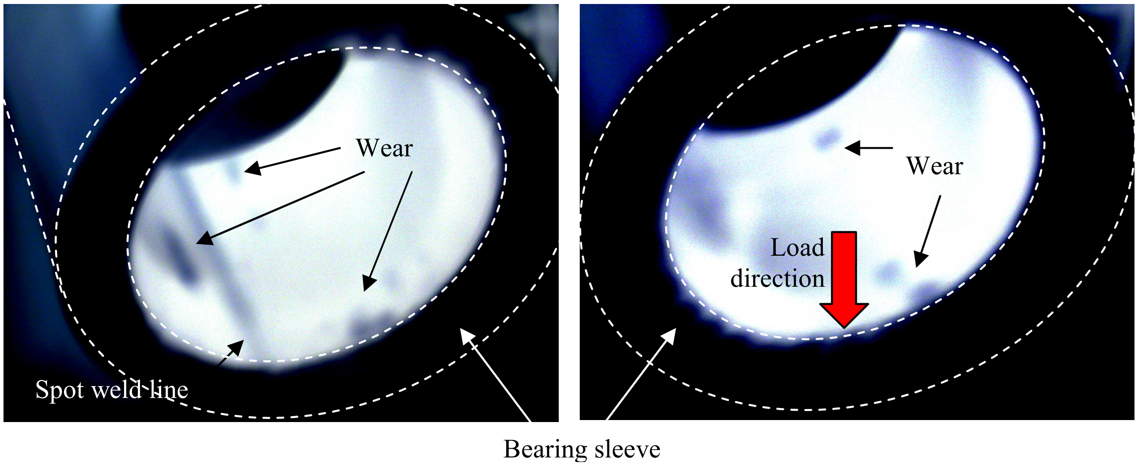

Figure VI-2 Test foil bearing surface condition after rotordynamic experiments

Table VI-2 Test foil bearing diameters before and after the measurements

	Diameter before experiments (mm)		Diameter after experiments (mm)	
	Drive end *FB*	Free end *FB*	Drive end *FB*	Free end *FB*
Outboard edge	38.15	38.15	38.22	38.20
Middle plane	Not measured	Not measured	38.19	38.18
Inboard edge	38.17	38.16	38.20	38.19

Measurements taken with a micrometer gage. Uncertainty: ± 0.012 mm.

Table VI-3 presents the rotor (shaft) diameter after the rotordynamic tests at the two bearing locations. Notice that the excessive coating wear at the outboard edges decreases the rotor diameter approximately 40 μm (± 12 μm) at these locations. Recall that the shaft coating thickness is 25.4 μm, thus the shaft coating completely wears at the outboard edges as depicted in the shaft photographs above. At the middle plane and inboard edge the coating wear is approximately 30 μm.

After conducting an exhaustive experimentation, the test foil bearings managed to survive severe synchronous and subsynchronous rotor vibrations, by virtue of their inherent flexibility. The top foil presented minor coating wear spots, especially at the bearing edges, while the coating wear in the test rotor was more severe due to the shaft coating softness compared to the top foil coating.

Table VI-3 Test rotor diameters before and after the measurements

	Diameter before experiments (mm)		Diameter after experiments (mm)	
	Drive end	Free end	Drive end	Free end
Outboard edge	38.10	38.10	38.06	38.07
Middle plane	38.10	38.10	38.08	38.08
Inboard edge	38.10	38.10	38.08	38.08

Measurements taken with a caliper. Uncertainty: ± 0.010 mm.
Average of four measurements at various circumferential locations.

Based on the post-test diameters of the test bearing and rotor, the bearing clearances are estimated at three planes, see Table VI-4. The radial clearances are the largest at the outboard edges for both bearings since most of the coating wear occurred at this location. Radial clearances for the middle plane and inboard edge are quite similar for each bearing and comparable to the estimated bearing clearances obtained through load versus displacement tests, see page 30.

Table VI-4 Calculated radial clearances based on the final diameters of the test rotor and foil bearings

	Radial clearances after experiments (μm)	
	Drive end (*c* = 50 μm)	Free end (*c* = 45 μm)
Outboard edge	90	65
Middle plane	55	50
Inboard edge	60	55

CHAPTER VII

CONCLUSIONS

High performance oil-free turbomachinery implements gas foil bearings *(GFB*s*)* to improve mechanical efficiency in compact units. Since the *GFB* design is largely empirical due to their mechanical complexity, the need of experimental demonstration of rotating machinery supported on foil bearing is essential. This work reveals important characteristics of this novel oil-free bearing technology by conducting rotordynamic experiments of a test rotor supported on two bump-type gas foil bearings.

Tests consisted of coastdown responses from a top speed of 25 krpm. These tests aid to evaluate the rotordynamic performance of a hollow rotor, 0.98 kg [2.2 lb] weight, supported on gas foil bearings. In general, rotor synchronous responses at the critical speed appear nearly proportional to the added imbalance masses. Appearance of subsynchronous vibrations is sensitive to the level of imbalance added to the rotor, i.e. the larger the imbalance, the larger the magnitudes of subsynchronous motions. In general, subsynchronous frequencies track the shaft speed, being most severe at frequencies coinciding with the rotor rigid body mode natural frequencies. The whirl ratio at the onset of the instability equals 50% of shaft speed. For the largest imbalance condition, amplitudes of subsynchronous vibration are significantly larger than the synchronous amplitudes, in occasions reaching maximum filtered subsynchronous amplitudes of ~ 60 μm.

External air pressurization through the bearing ends aids to reduce the amplitude of synchronous motions while crossing a critical speed. Feed pressure has no discernable effect on the amplitude of synchronous motions well above the rotor/bearing system critical speed. The air-film lubricates the contact regions allowing the bumps to hover easily, thus dissipating more energy. Importantly enough, the tests also demonstrate that increasing air pressures ameliorates the amplitudes of subsynchronous motions due to the significant effect of the axial flow retarding the circumferential flow development.

The experimental investigation aids to understand the rotordynamic performance of gas foil bearings. There are commercial claims stating foil bearings are free of rotordynamic instabilities. The current experimental results, however, show that rotor subsynchronous motions are of large amplitude though confined over a well defined rotor speed range which includes twice the system critical speed. Operation free of subsynchronous motion may be possible at even higher shaft speeds. This assertion may be corroborated in future tests with a faster drive motor.

Predictions of the static equilibrium *GFB* performance are presented for static load conditions comparable to the test foil bearing. Journal eccentricities for the two test bearings decrease with increasing shaft speeds, while predicted attitude angle show nearly centered operation at the rotor maximum speed (25,000 rpm), thus favoring hydrodynamic instability. The bearing clearance clearly affects the foil bearing static performance. At low speeds, an increase in the bearing clearance leads to smaller fluid film thickness. Conversely, at higher speeds the gas film thickness increases as the bearing clearance increases.

A finite element rotordynamic analysis models the test rotor and uses predicted synchronous speed bearing force coefficients based on the static load equilibrium *GFB* position. A calibration of the rotor model against experimental results of free-free mode natural frequencies renders excellent agreement. The rotordynamic analysis predicts critical speeds at ~8,000 rpm and ~9,000 rpm which correlate well with experimental evidences. Predictions of rotordynamic stability for the test speed range (0 to 25,000 rpm) show unstable operation for the rotor/bearing system starting at 12,000 rpm and higher. Experimental results also show a similar region of subsynchronous vibrations starting at 22,000 rpm and continuing up to 12,000 rpm. Predictions and experimental results show good agreement in terms of critical speed correlation, and moderate displacement amplitude discrepancies for some imbalance conditions.

Post-test inspection of the rotor evidenced severe shaft coating wear at the location of the bearing edges. The top foil presents minor coating wear spots, except at the bearing edges and at the location of static load applications. In general, the test foil bearings proved to survive severe synchronous and subsynchronous rotor vibrations, by virtue of their inherent flexibility. The capability of foil bearings to withstand severe subsynchronous vibrations and still preserve its mechanical integrity makes this oil-free bearing technology a great fit for commercial applications in turbomachines. However, limited load capacity and low damping are still main issues to be addressed.

Future experimental work on the foil bearing test rig needs to assess foil bearing performance at higher rotational speeds with a faster drive motor. The influence of more severe static load conditions on the rotor/bearing performance can be studied using the electromagnetic loader. Finally, the need of a less constraining connecting mechanism between the motor and rotor is recommended to avoid bending of rotor components within the speed range of operation, to improve motor/shaft misalignment, and to minimize flexible coupling effect on the rotor/bearing performance.

REFERENCES

[1] Agrawal, G. L., 1997, “Foil Air/Gas Bearing Technology - An Overview,” International Gas Turbine & Aeroengine Congress & Exhibition, Orlando, Florida, ASME paper 97-GT-347.

[2] Heshmat, H., Walowit, J., and Pinkus, O., 1983, “Analysis of Gas-Lubricated Compliant Journal Bearings,” ASME Journal of Lubrication Technology, **105** (4), pp. 647-655.

[3] Peng, J.-P, and Carpino, M., 1993, “Calculation of Stiffness and Damping Coefficient for Elastically Supported Gas Foil Bearings,” ASME Journal of Tribology, **115** (1), pp. 20-27.

[4] DellaCorte, C., and Valco, M., 2000, “Load Capacity Estimation of Foil Air Bearings for Oil-Free Turbomachinery Applications,” STLE Tribology Transactions, **43** (4), pp. 795-801.

[5] Ku, C.-P, and Heshmat, H., 1992, “Complaint Foil Bearing Structural Stiffness Analysis Part I: Theoretical Model - Including Strip and Variable Bump Foil Geometry,” ASME Journal of Tribology, **114** (2), pp. 394-400.

[6] Ku, C.-P, and Heshmat, H., 1993, “Complaint Foil Bearing Structural Stiffness Analysis Part II: Experimental Investigation,” ASME Journal of Tribology, **113** (3), pp. 364-369.

[7] Iordanoff, I., 1999, “Analysis of an Aerodynamic Complaint Foil Thrust Bearing: Method for a Rapid Design,” ASME Journal of Tribology, **121**, pp. 816-822.

[8] Rubio, D., and San Andrés, L., 2004, “Bump-Type Foil Bearing Structural Stiffness: Experiments and Predictions,” ASME Paper GT 2004-53611.

[9] Ku, C.-P, and Heshmat, H., 1994, “Structural Stiffness and Coulomb Damping in Compliant Foil Journal Bearing: Theoretical Considerations,” STLE Tribology Transactions, **37** (3), pp. 525-533.

[10] Ku, C.-P, and Heshmat, H., 1994, “Structural Stiffness and Coulomb Damping in Compliant Foil Journal Bearing: Parametric Studies,” STLE Tribology Transactions, **37** (3), pp. 455-462.

[11] Heshmat, H., 1994, “Advancements in the performance of Aerodynamic Foil Journal Bearings: High Speed and Load Capability,” ASME Journal of Tribology, **116** (2), pp. 287-295.

[12] DellaCorte, C., and Valco, M., 2003, “Oil-Free Turbomachinery Technology for Regional Jet, Rotorcraft and Supersonic Business Jet Propulsion Engines,” American Institute of Aeronautics and Astronautics, ASABE 2003 – 1182.

[13] Gu, A., 1988, “Process Fluid Foil Bearing Liquid Hydrogen Turbopump,” AIAA/ASME/SAE/ASEE 24th Joint Propulsion Conference, Boston, Massachusetts, Paper No. AA-88-3130.

[14] Chen, H., Howarth, R., Geren, B., Theilacker, J., and Soyars, W., 2001, “Application of Foil Bearing to Helium Turbocompressor,” Proceedings of the 30th Turbomachinery Symposium, Houston, TX, pp. 103-112.

[15] Ku, C-P., 1993, "An Experimental and Theoretical Study of the Dynamic Structural Stiffness in Compliant Foil Journal Bearings," ASME 14th Biennial Conference on

Mechanical Vibration and Noise, Albuquerque, NM, DE-Vol. **63**, *Vibration of Mechanical Systems and the History of Mechanical Design*, pp. 83-88.

[16] Heshmat, H., and Ku, C.-P., 1994, “Structural Damping of Self-Acting Compliant Foil Journal Bearings,” ASME Journal of Tribology, **116** (1), pp. 76-82.

[17] Salehi, M., Heshmat, H., and Walton, J., 2003, “On the Frictional Damping Characterization of Compliant Bump Foils,” Transactions of the ASME, **125** (4), pp. 804-813.

[18] Heshmat, H., 1994, “Advancements in the performance of Aerodynamic Foil Journal Bearings: High Speed and Load Capability,” ASME Journal of Tribology, **116** (2), pp. 287-295.

[19] Heshmat, H., 2000, “Operation of Foil Bearing Beyond the Bending Critical Mode,” ASME Journal of Tribology, **122** (1), pp. 192-198.

[20] Howard, S., DellaCorte, C., Valco, M.-J., Prahl, J.-M., and Heshmat, H., 2001, “Steady-State Stiffness of Foil Air Journal Bearings at Elevated Temperatures,” STLE Tribology Transactions, **44** (3), pp. 489-493.

[21] J.F., Walton II, and H., Heshmat, 2002, “Application of Foil Bearings to Turbomachinery Including Vertical Operation,” Transactions of ASME, **124**, pp. 1032-1041.

[22] E., Swason, J.F., Walton II, H., Heshmat, 2002, “A Test Stand for Dynamic Characterization of Oil-Free Bearings for Modern Gas Turbine Engines,” Proceedings of the ASME Turbo Expo 2002, Amsterdam, The Netherlands, pp. 1 -12.

[23] Lee, Y,B., Kim, T.H, Kim, C.H., and Lee, N.S., 2003, "Suppression of Subsynchronous Vibrations Due to Aerodynamic Response to Surge in a Two-Stage Centrifugal Compressor with Air Foil Bearings," STLE Presentation No. AM03-8.

[24] Y., Hou, L.Y., Xiong, and C.Z., Chen, 2004, "Experimental Study of a New Foil Air Bearing with Elastic Support," Tribology Transactions, **47**, pp. 308-311.

[25] DellaCorte, C., and Valco, M., 2000, "Load Capacity Estimation of Foil Air Journal Bearing for Oil-Free Turbomachinery Applications," STLE Tribology Transactions, **43** (4), pp. 795-801.

[26] Peng, J.-P, and Carpino, M., 1993, "Calculation of Stiffness and Damping Coefficient for Elastically Supported Gas Foil Bearings," ASME Journal of Tribology, **115** (1), pp. 20-27.

[27] San Andrés, L., 1994, "Turbulent Flow Foil Bearing for Cryogenic Applications," ASME Journal of Tribology, **117** (1), pp. 185-195.

[28] Lee, Y.-B., Kim, T.-H., Kim, C.-H., Lee, N.S., and Choi, D.-H., 2003, "Unbalance Response of a Super-Critical Rotor Supported by Foil Bearings – Comparison with Test Results," STLE Tribology Transactions, **47** (1), pp. 54-60.

[29] Lee, Y.-B., Kim, T.-H., Kim, C.-H., Lee, N.S., and Choi, D.-H., 2004. "Dynamic Characteristics of a Flexible Rotor System Supported by a Viscoelastic Foil Bearing (VEFB)," Tribology International, **37**, pp. 679-687.

[30] DellaCorte, C., Zaldana, A., and Radil, K., 2003, "A System Approach to the Solid Lubrication of Foil Air Bearing for Oil-Free Turbomachinery," ASME Journal of Tribology, **126** (1), pp. 200-207.

[31] Radil, K., Howard, S., and Dykas, B., 2002, "The Role of Radial Clearance on the Performance of Foil Air Bearings," STLE Tribology Transactions, **45** (4), pp. 485-490.

[32] Howard, S., DellaCorte, C., Valco, M.-J., Prahl, J.-M., and Heshmat, H., 2001, "Dynamic Stiffness and Damping Characteristics of a High-Temperature Air Foil Journal Bearing," STLE Tribology Transactions, **44** (4), pp. 657-663.

[33] Iordanoff, I., 1999, "Analysis of an Aerodynamic Complaint Foil Thrust Bearing: Method for a Rapid Design," ASME Journal of Tribology, **121**, pp.816-822.

[34] Heshmat, H., and Walton, J., 2005, "Demonstration of a Turbojet Engine Using Air Foil Bearing," ASME Paper GT2005-68404.

[35] Kim, T.H, and San Andrés, L., 2005, "Heavily Loaded Gas Foil Bearings: A Model Anchored to Test Data," ASME Paper GT2005-68486.

[36] Rubio, D., and San Andrés, L., 2005, "Structural Stiffness, Dry-Friction Coefficient and Equivalent Viscous Damping in a Bump-Type Foil Gas Bearing," ASME Paper GT2005-68384.

APPENDIX A

IDENTIFICATION OF FB STRUCTURAL DYNAMIC COEFFICIENTS FROM RAP TESTS ON ROTOR

An experimental procedure was developed to estimate rigid body mode natural frequencies and to identify *FB* structural coefficients. The test procedure consisted of two different (linearly independent) impact excitations at the rotor center of gravity and rotor end. Figure A1 shows the time varying impact load and ensuing rotor displacements for the two set of impact locations, i.e. at the rotor center of gravity and the rotor motor end. The measured rotor displacements (z_A, z_B, y_A and y_B) are recorded at the both rotor ends (A and B) in the horizontal (y) and vertical (z) directions. Cross-coupled motions are found to be significantly small in comparison with direct rotor displacement, i.e. approximately 7% of direct motions. Figure A2 shows the Fast Fourier Transform of the calculated rotor motion at the center of gravity (z_G) and the rotor angular displacement (θ). Amplitudes of vibration at the center of gravity for each impact excitation indicate that the first and second rigid body mode natural frequencies are approximately 156 Hz and 164 Hz, respectively.

A comprehensive parameter identification procedure to identify *FB* structural stiffness and equivalent damping coefficients was developed. The rotor/foil bearing system was modeled as 2-degree of freedom linear mechanical system. Structural stiffness and damping coefficients are estimated by calculating the experimental dynamic stiffness matrix from the test data in the frequency domain. Figure A3 shows that an increase in the excitation frequency slightly increases the direct stiffness coefficients (K_{zz}) and decreases the direct damping coefficients (C_{zz}) for both test foil bearings. The structural stiffness of the foil bearing located at the free end is slightly larger than the foil bearing located at the motor end, while equivalent viscous damping coefficients are slightly larger on the *FB* located at the motor end than the one located at the free end.

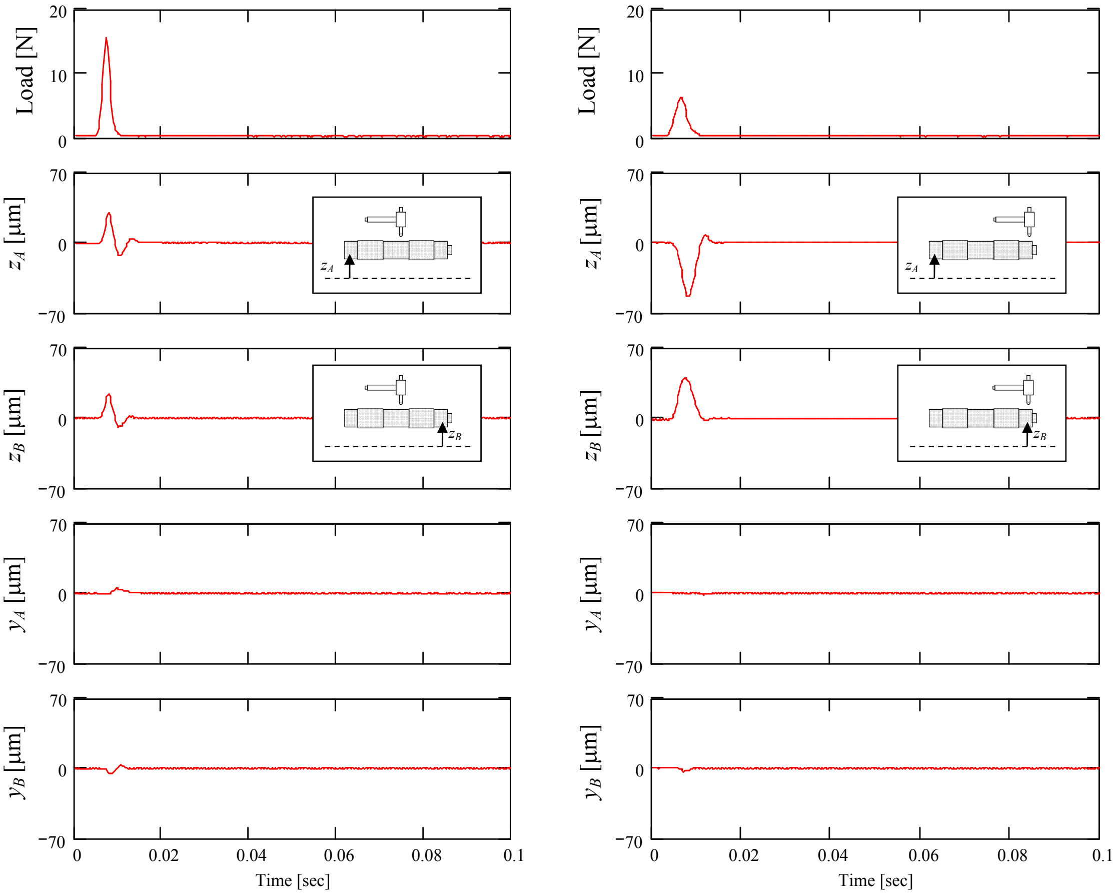

A) Impact at the center of gravity **B) Impact at the motor end**

Figure A1 Time dependant impact force and rotor displacements for load excitations at the A) center of gravity and B) the motor end

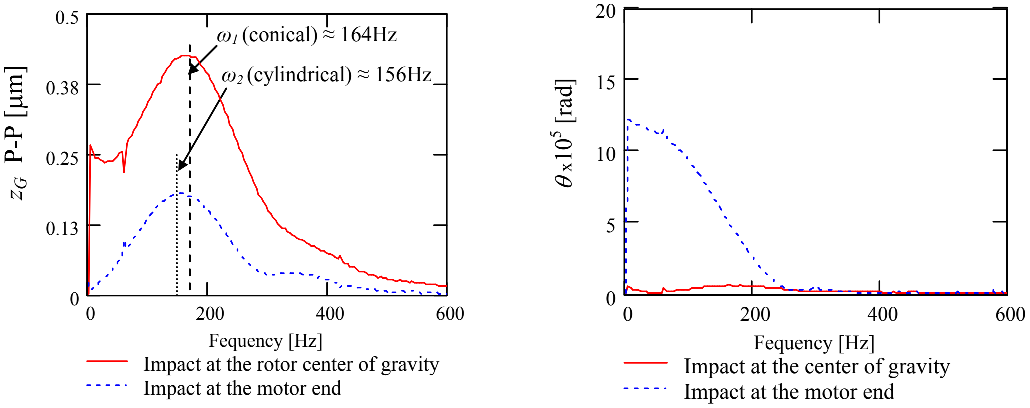

A) Amplitudes of vertical displacements at the center of gravity

B) Amplitudes of angular displacement

Figure A2 Impact forces, A) at the rotor center of gravity and B) at the motor end, and calculated C) rotor center of gravity displacement and D) angular deflections varying with frequencies

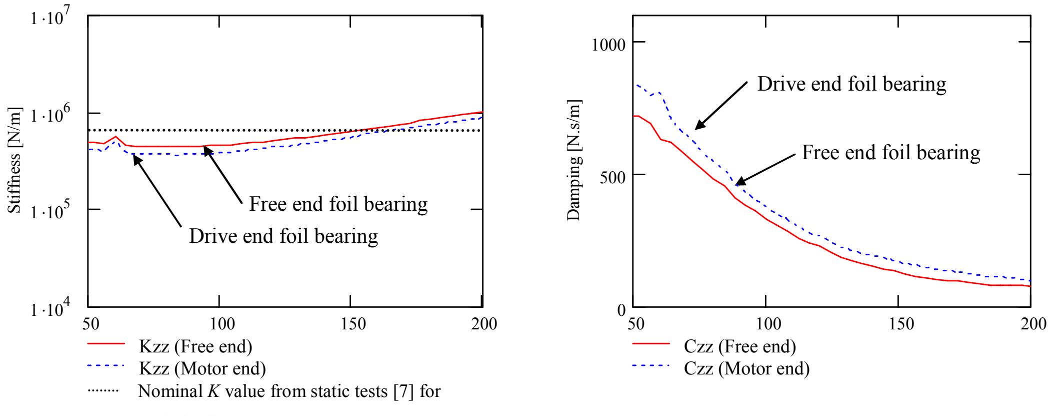

a) Estimated FB structural stiffness

b) Estimated equivalent viscous damping coefficients

Figure A3 Identified stiffness and damping coefficients versus frequency

The logarithmic decrement method is used to assess modal damping ratios for the test foil bearings. Linear and exponential approximations of the rotor transient responses allow determining dry friction coefficients and modal damping ratios of the test foil bearings. Table A1 shows experimental results of modal damping ratios for both foil bearings. Notice the large damping ratio coefficients for both bearing for non-rotating operations.

Table A1 Identified FB parameters from linear and exponential curve fit of rotor transient response

Identified FB parameters	Symbol	FB Drive end	FB Free end
Dry Friction Force, N	F_{DRY}	2.2	3.8
Dry friction coefficient	μ	0.15	0.24
Average structural Stiffness, MN/m	K	0.8	0.9
Standard deviation of K, MN/m	K_S	0.18	0.19
Modal damping ratio	ξ	42%	35%

APPENDIX B

ELECTROMAGNETIC LOAD ACTUATOR DESCRIPTION

For identification of *FB* force coefficients, an electromagnetic load fixture delivers non-contacting magnetic forces to the rotor middle span while the rotor spins. The electromagnetic loads are generated through a series of copper wires wounded around a high-magnetic permeability material made of Alloy-49. The electromagnetic forces are transmitted through small air gaps, typically varying from 0.25mm [0.010 in] to 0.50 mm [0.020 in], between the electromagnet tip and the rotor surface. Increasing current magnitudes through the copper wires boost electromagnetic forces applied to the rotor until reaching the electromagnet saturation zone. Figure A1 depicts a close view of the electromagnetic load actuator. Table B1 outlines the electromagnet material properties as well as its major dimensional features.

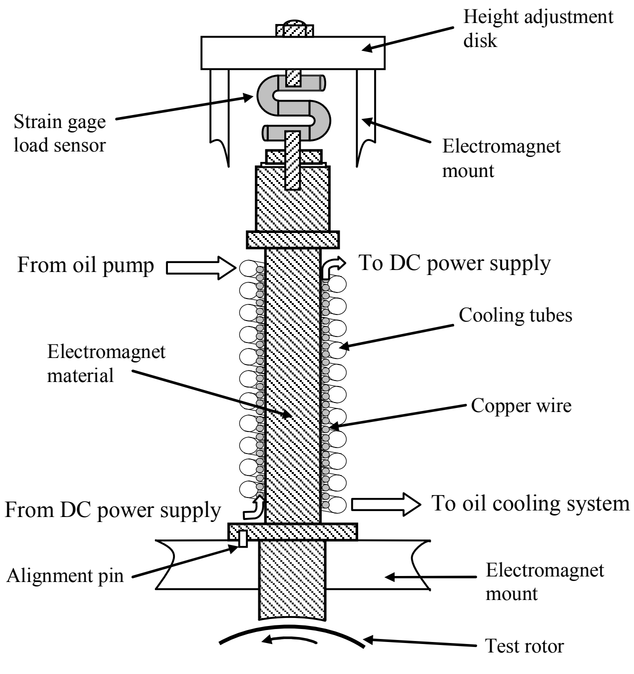

Figure B1 Schematic view of the electromagnetic actuator installed on the test rig

The electromagnetic load actuator exerts attracting forces to the test rotor, which also react to the strain gage load sensor. The opposite end of the strain gage features a disk mechanism upon which the electromagnetic-rotor gap is adjusted. Upon installation, special care is taken to ensure that the electromagnet aligns properly with the rotor in order to avoid rubs while rotor spinning. Therefore, an alignment pin prevents the electromagnet to swivel along its axial axis. A cooling system with lubricant flowing through cooper piping wounded around the magnet conduct heat away. Oil flows from a cooling reservoir tank that keeps the oil temperature at approximately 25 ºC. The oil contained on the cooling reservoir is brought to the electromagnet using a centrifugal pump of variable speed.

Table B1 Electromagnet material properties, physical dimensions and main characteristics

Material Properties	SI Units	English Units
Material	Steel Alloy-49	
Material density, ρ_E	8166 kg/m^3	0.294 lb/in^3
Modulus of elasticity, E_E	51.7 MPa	7498.5 Psi
Saturation flux density, ρ_{SAT}	1.5000 Tesla	15000 Gauss
Maximum permeability[20], μ_o	103000	
Physical Dimensions		
Pole area, A_P	451.61 mm^2	0.70 in^2
Tip arcuate diameter, D_E	35.05 mm	1.38 in
Length of wounded wire, L_E	101.6 mm	4.00 in
Number of turns, N_T	~ 420	

---

[20] Maximum permeability after being hydrogen annealed.

A DC power source supplies variable output voltages (0-25V) and currents (0-80A) to the cooper wires wounded on the electromagnet. In addition, a strain gage load sensor records the electromagnetic force applied to the test rotor, while a strain gage panel meter displays the applied electromagnetic force. To verify a proper temperature isolation of the electromagnet surface, a K-type thermocouple records the surface temperature at the copper wires when re-circulated cool oil flows through the tubes.

APPENDIX C

WATERFALL PLOTS OF BASELINE ROTOR RESPONSE AT THE FREE END, HORIZONTAL AND VERTICAL DIRECTIONS

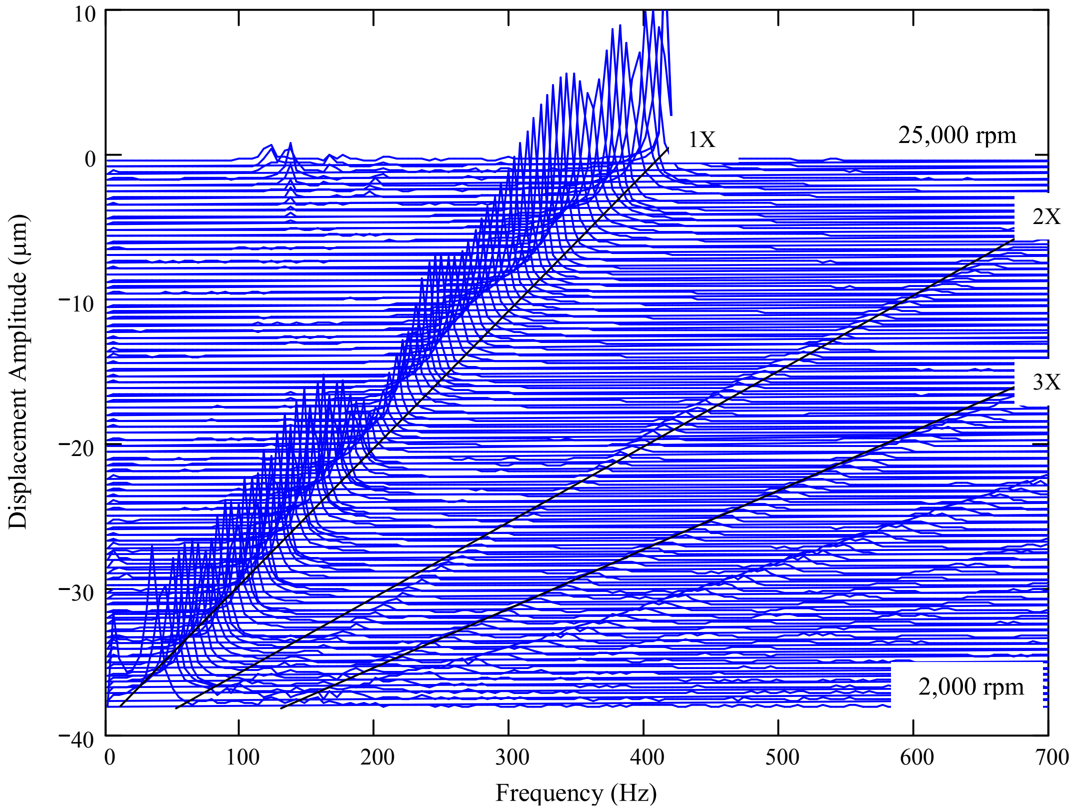

Figure C1 Waterfall plot of baseline rotor response at free end, horizontal location (X_{FE}). Air pressure at 34.4 kPa [5 psig]

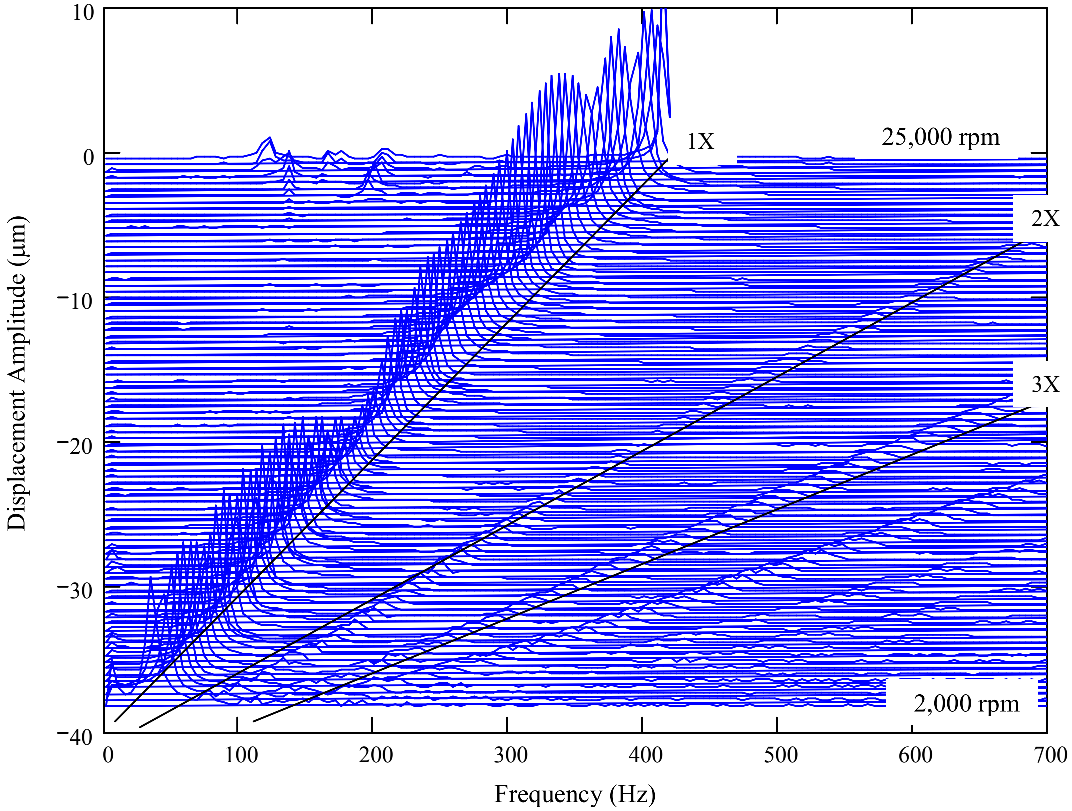

Figure C2 Waterfall plot of baseline rotor response at the free end, vertical location (Y_{FE}). Air pressure at 34.4 kPa [5 psig]

APPENDIX D

SYNCHRONOUS AND DIRECT ROTOR RESPONSES FOR IMBALANCE DISPLACEMENTS A2, B1 AND B3

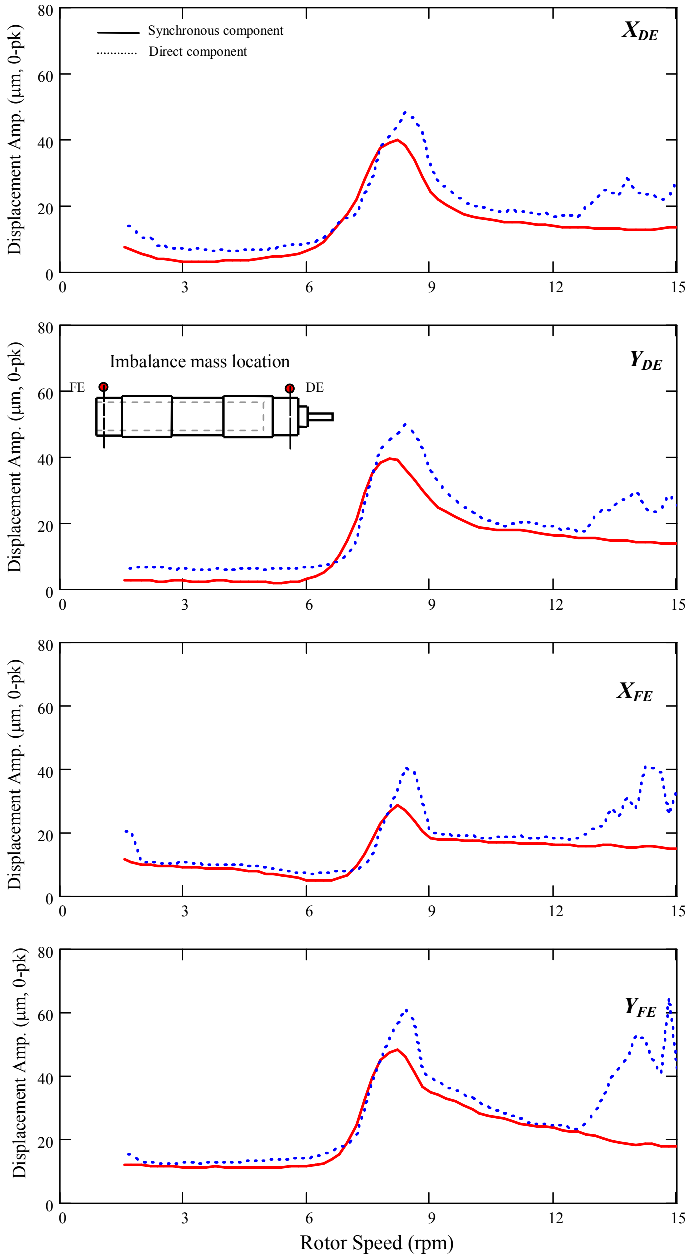

Figure D1 Direct and synchronous rotor response for an imbalance u = 9.5 µm (in phase, Test A2). Air pressure at 34.4 kPa [5 psig]

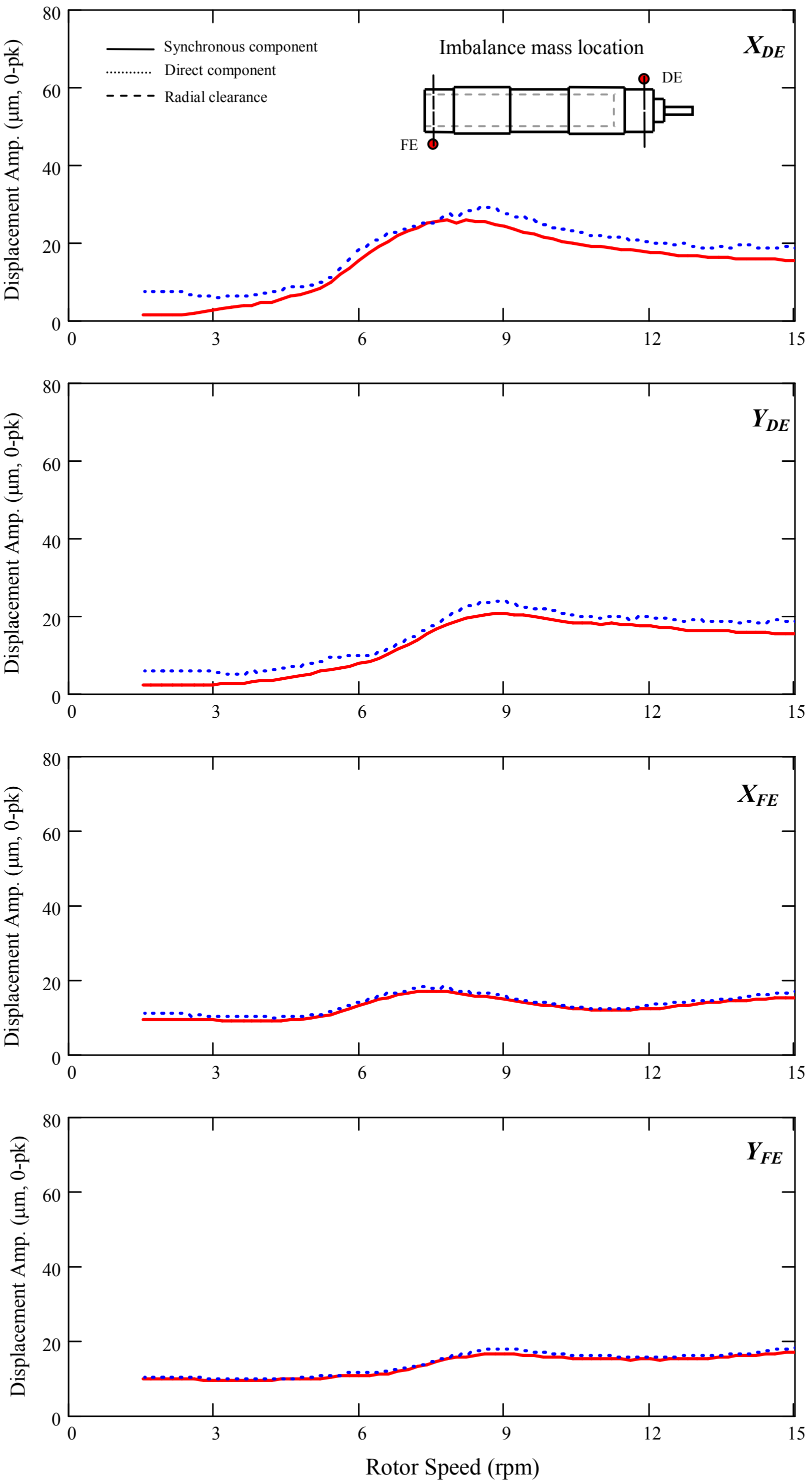

Figure D2 Direct and synchronous rotor response for an imbalance u = 3.7 µm (out of phase, Test B1). Air pressure at 34.4 kPa [5 psig]

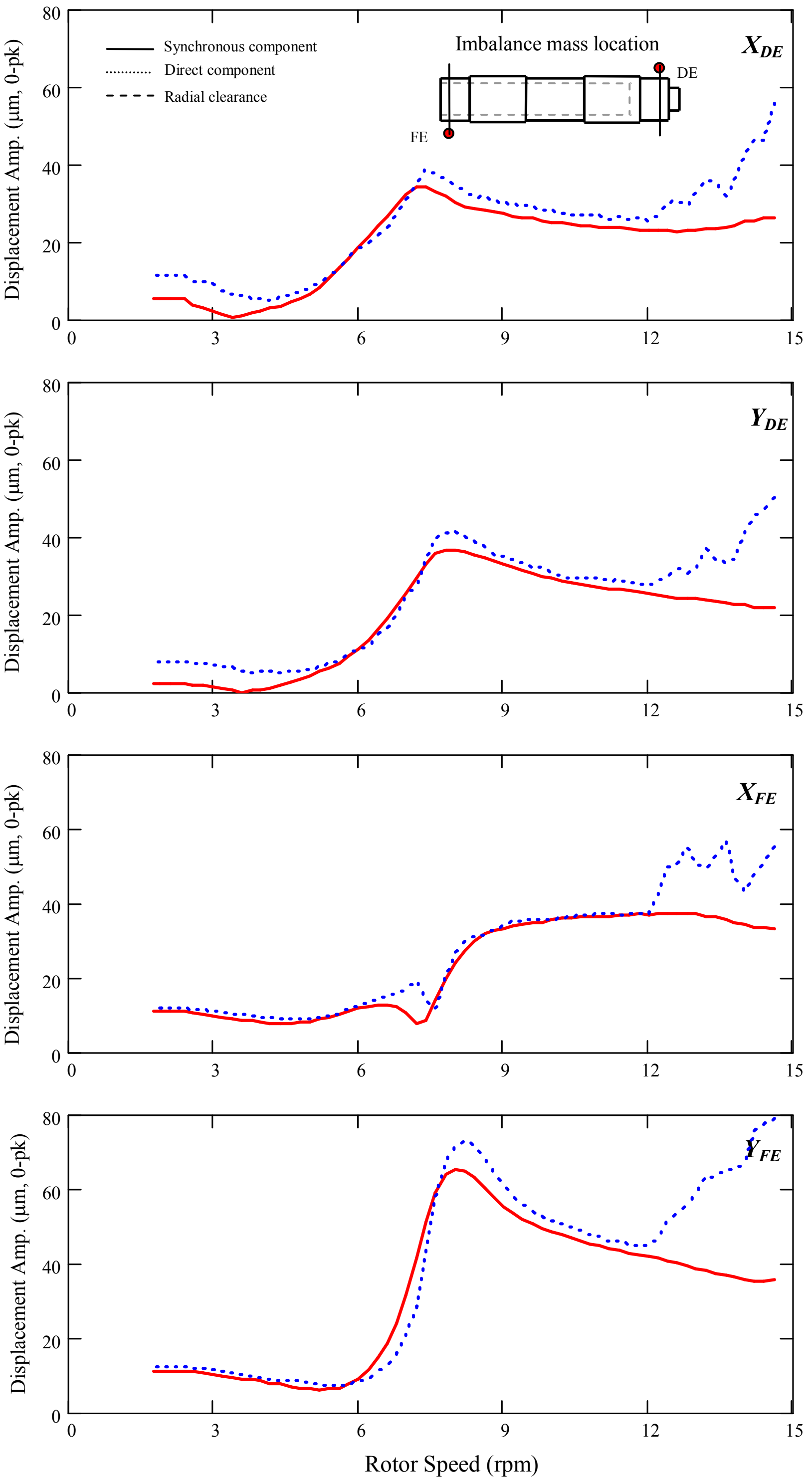

Figure D3 Direct and synchronous rotor response for an imbalance u = 7.4 µm (out of phase, Test B3). Air pressure at 34.4 kPa [5 psig]

APPENDIX E

SYNCHRONOUS RESPONSE AND PHASE ANGLE FOR IMBALANCE TESTS A IN THE VERTICAL DIRECTION AT THE DRIVE AND FREE ROTOR ENDS

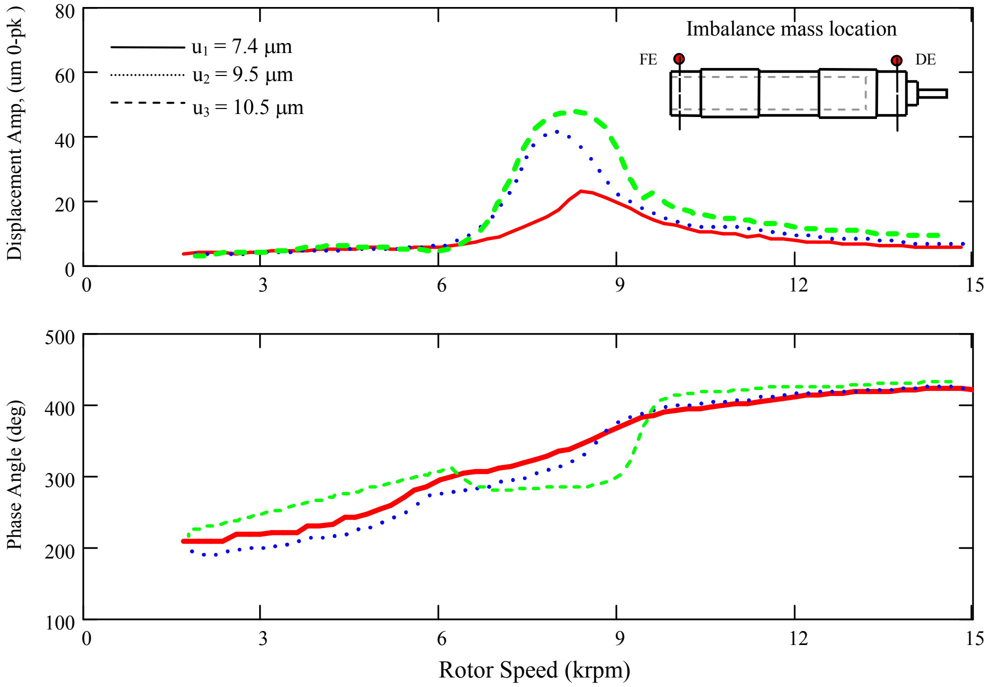

Figure E1 Synchronous rotor response and phase angle for imbalance tests A (in phase). Air pressure at 34.4 kPa [5 psig]. Measurements taken at drive end, vertical direction (Y_{DE}). With baseline subtractions

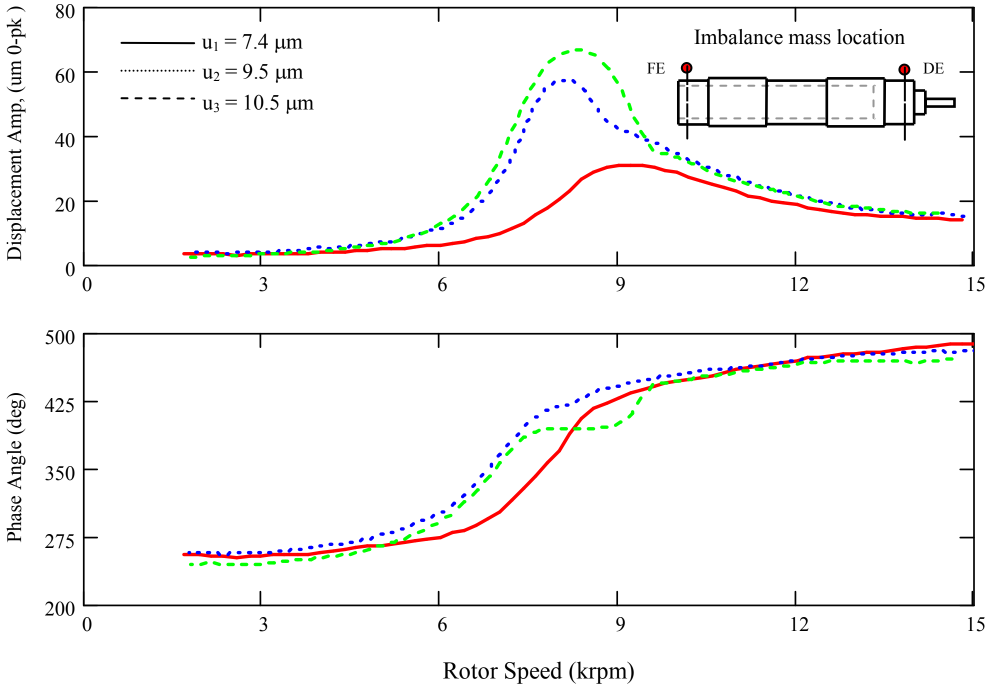

Figure E2 Synchronous rotor response and phase angle for imbalance tests A (in phase). Air pressure at 34.4 kPa [5 psig]. Measurements taken at free end, vertical direction (Y_{FE}). With baseline subtractions

APPENDIX F

SYNCHRONOUS RESPONSE AND PHASE ANGLE FOR TESTS B IN THE HORIZONTAL DIRECTION AT THE DRIVE AND FREE ROTOR ENDS

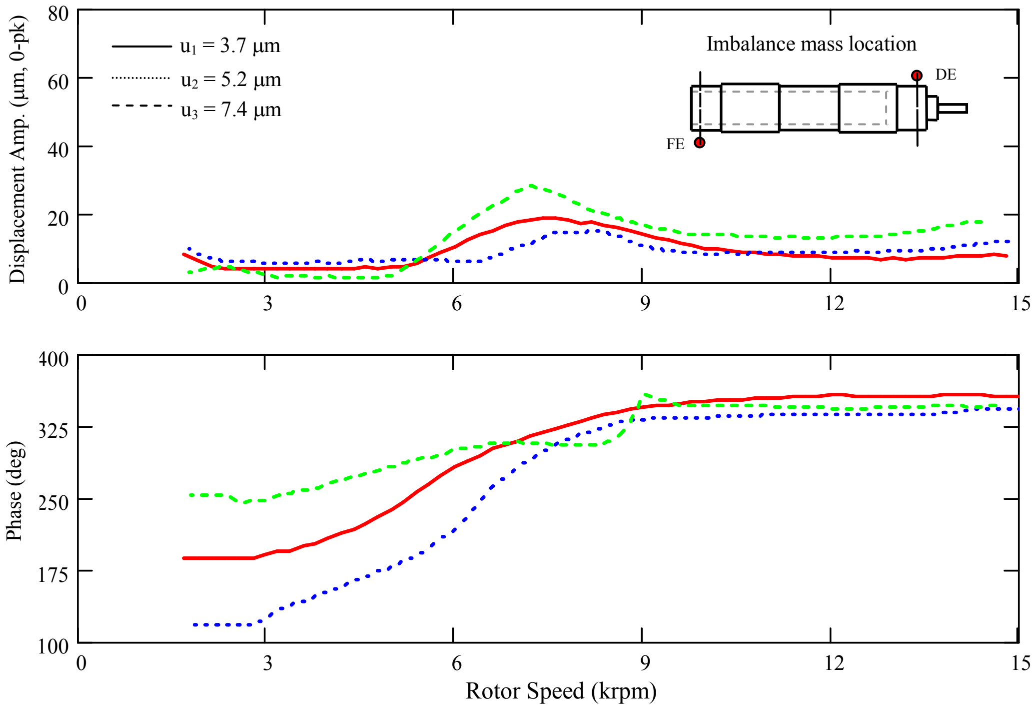

Figure F1 Synchronous rotor response and phase angle for imbalance tests B (out of phase) Air pressure at 34.4 kPa [5 psig]. Measurements taken at drive end horizontal direction (X_{DE}). With baseline subtractions

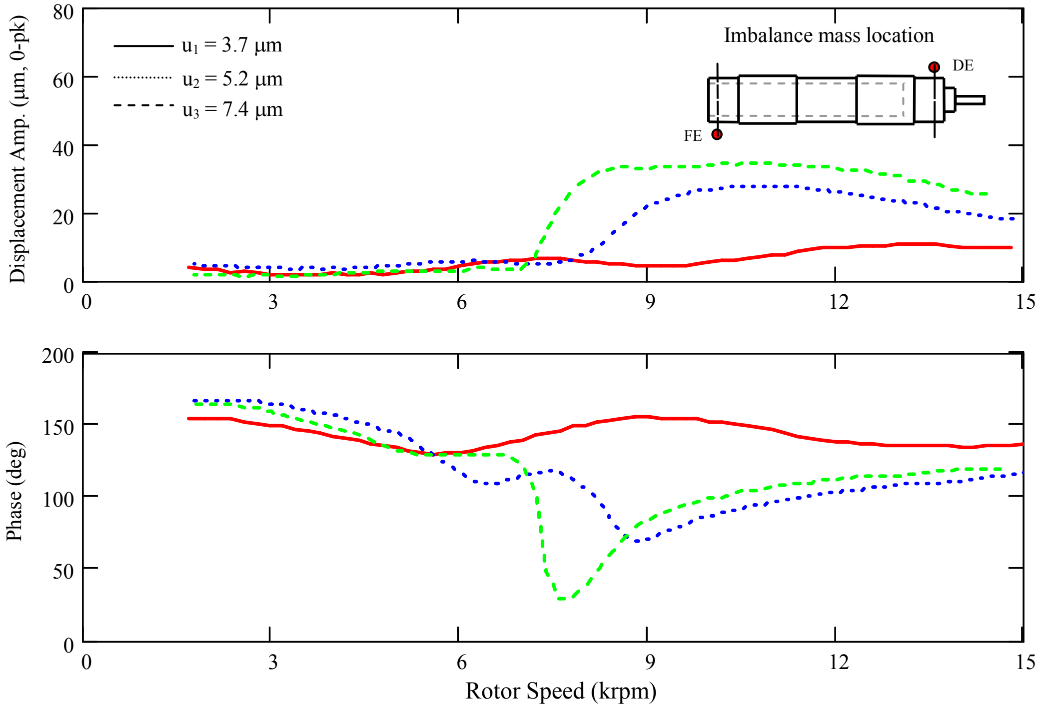

Figure F2 Synchronous rotor response and phase angle for imbalance tests B (out of phase). Air pressure at 34.4 kPa [5 psig]. Measurements taken at free end horizontal direction (X_{FE}). With baseline subtractions

APPENDIX G

AXIAL BEARING FLOW PARAMETER CALCULATION

The simple calculations to determine axial flow rate along the bearing axial length assumes laminar flow and journal center operations. The Reynolds equation of classical lubrication theory with no circumferential flow is,

$$\frac{d}{dz}\left(-\frac{\rho \cdot c^3}{12 \cdot \mu_V}\frac{dP}{dz}\right) = \frac{d}{dz}\left(\dot{M}_z\right) = 0 \tag{G1}$$

where, c is the bearing clearance, P is the pressure across the bearing axial length, μ_V is the gas viscosity, ρ is the air density, z is the axial coordinate system across the bearing length, and $\dot{M}_z$ is the mass flow rate per circumferential length.

The modified Reynolds equation for an ideal gas, using the ideal gas law[21], is

$$\frac{d}{dz}\left(-\frac{P \cdot c^3}{12 \cdot \mu_V \cdot R_g \cdot T}\frac{dP}{dz}\right) = 0 \tag{G2}$$

where, R_g is the gas constant, T is the temperature across the bearing axial length. It follows from Equation (G2) that the mass flow rate per circumferential length ($\dot{M}_z$) is constant,

$$\dot{M}_z = -\frac{P \cdot c^3}{12 \cdot \mu_V \cdot R_g \cdot T}\frac{dP}{dz} = cte \tag{G3}$$

---

[21] The ideal gas law states that $\rho = \frac{P}{R \cdot T}$

Integrating Equation (H3) along the axial length leads to,

$$\dot{M}_z \cdot L = \frac{c^3}{24 \cdot \mu_V \cdot R_g \cdot T}\left(P_s^2 - P_a^2\right) \tag{G4}$$

where, L is the bearing axial length. Therefore, the total flow rate ($\dot{m}_z$) is,

$$\dot{m}_z = \frac{\pi \cdot D \cdot c^3}{24 \cdot \mu_V \cdot R_g \cdot T}\left(\frac{P_s^2 - P_a^2}{L}\right) = \dot{M}_z \cdot \pi \cdot D \tag{G5}$$

Finally, the Reynolds number (Re_A) for axial flow is defined as,

$$Re_A = \frac{V_z \cdot \rho \cdot c}{\mu_V} = \frac{\dot{M}_z}{\mu_V} \tag{G6}$$

where, V_z is the gas velocity at the bearing exit plane ($P = P_A$).

$$V_z = \frac{\dot{M}_z}{\rho \cdot c} \tag{G7}$$

APPENDIX H

BENDING MODE SHAPES OF TEST ROTOR ALONE AND TEST ROTOR WITH THE CONNECTING SHAFT

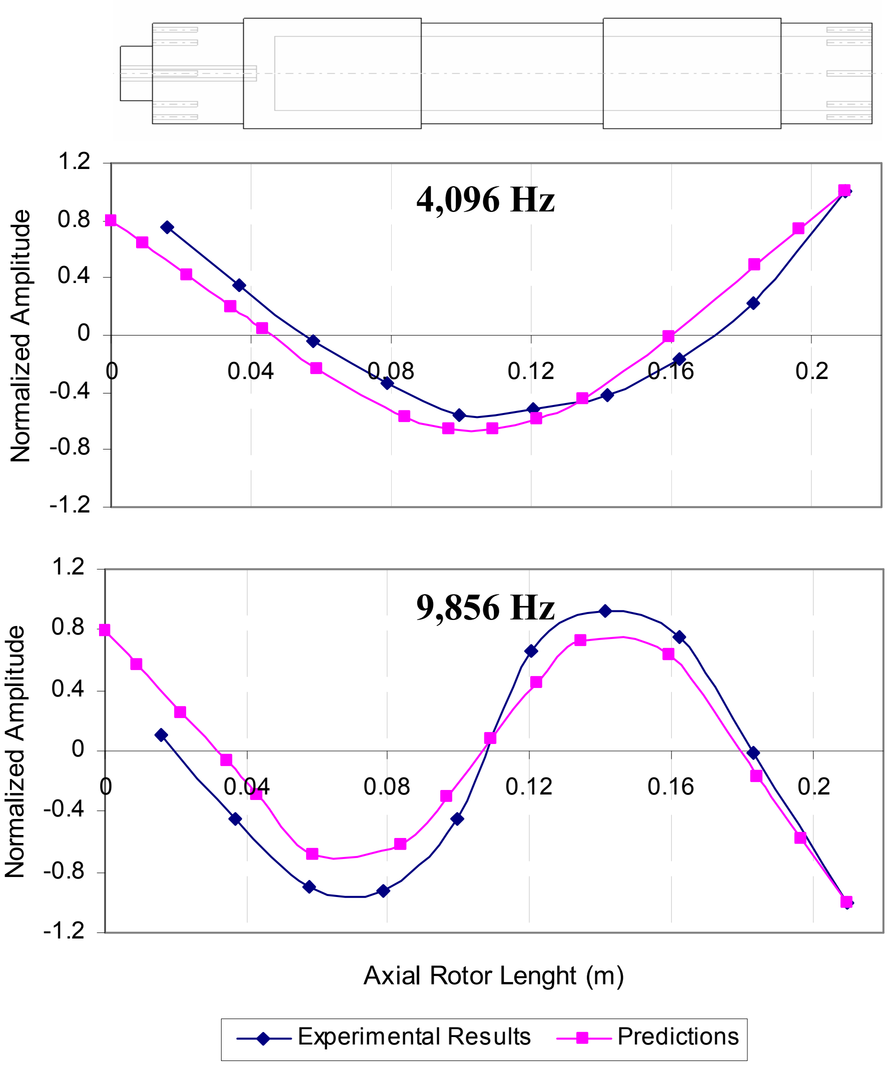

Figure H1 Measured and predicted free-free mode shapes of test rotor without the connecting shaft and flexible coupling

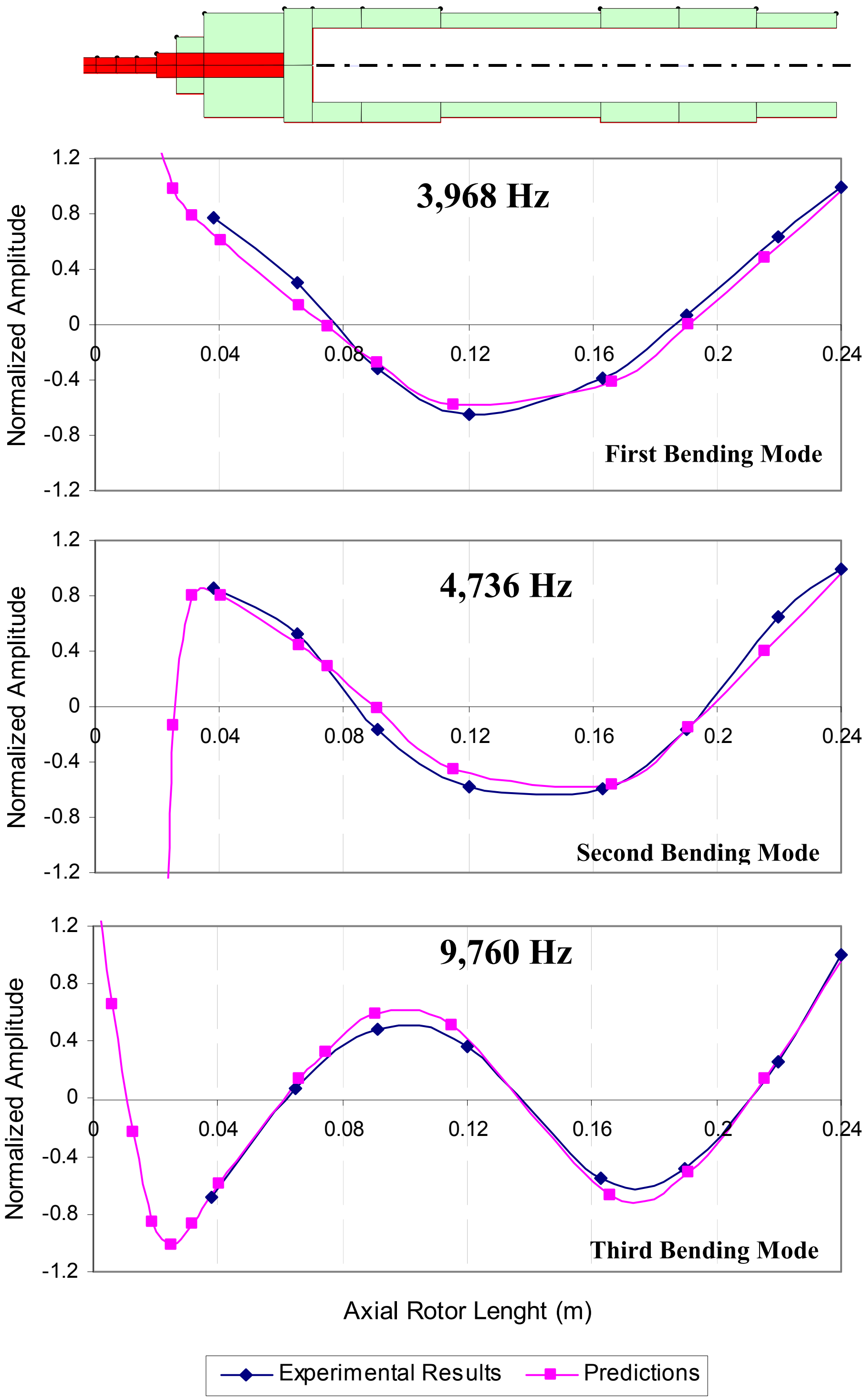

Figure H2 Measured and predicted free-free mode shapes of test rotor with connecting shaft (no flexible coupling)

APPENDIX I

DEFLECTED ROTOR SHAPES AT SELECTED SHAFT SPEEDS FOR THE LARGEST IMBALANCE MASS CONFIGURATION

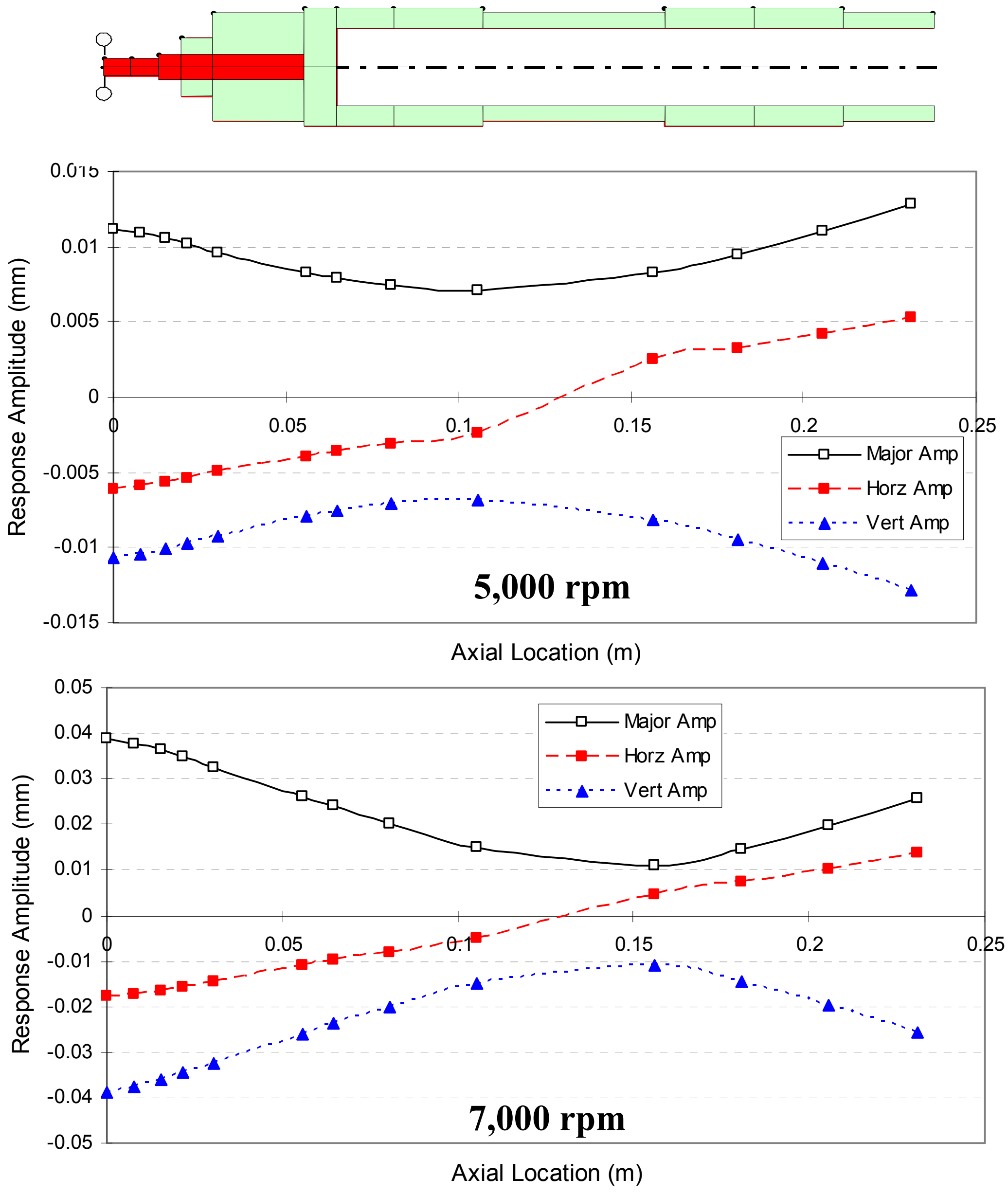

Figure I1 Deflected shapes of test rotor with connecting shaft and flexible rotor at 5,000 rpm and 7,000 rpm for an in-phase imbalance of u = 10.7 µm

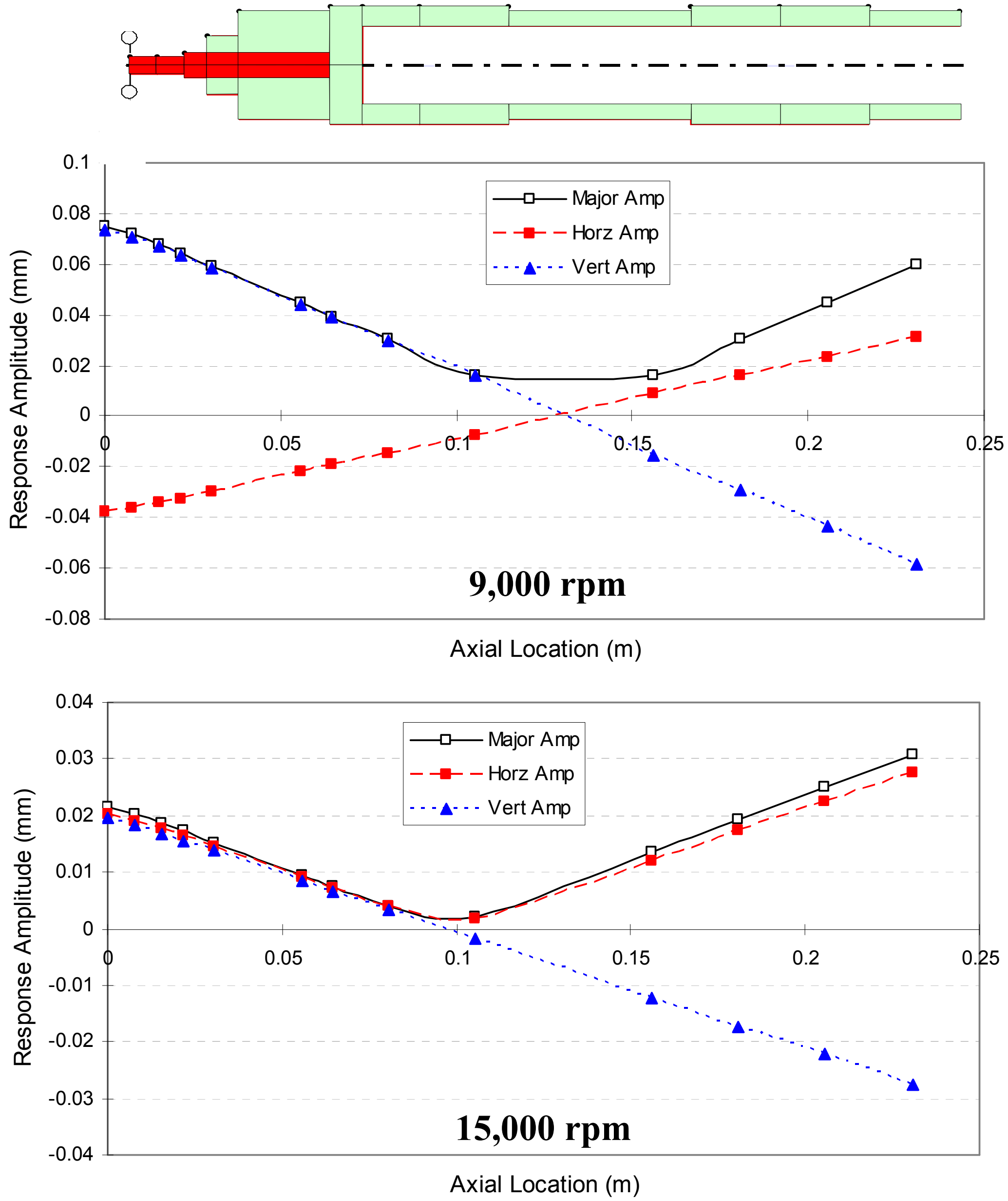

Figure I2 Deflected shapes of test rotor with connecting shaft and flexible rotor at 9,000 rpm and 15,000 rpm for an in-phase imbalance of u = 10.7 μm

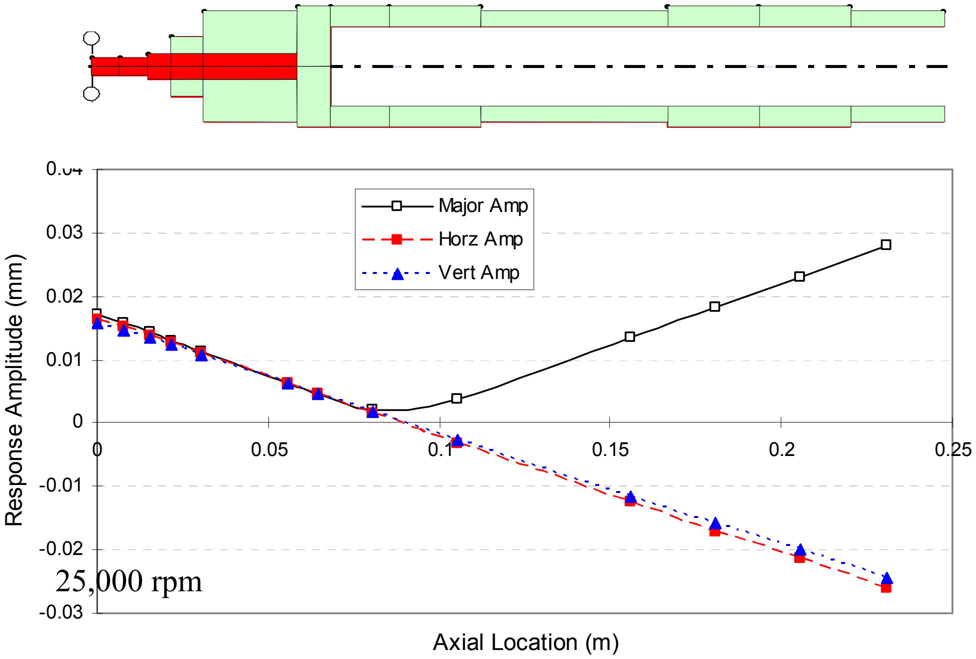

Figure I3 Deflected shapes of test rotor with connecting shaft and flexible rotor at 25,000 rpm for an in-phase imbalance of u = 10.7 μm

APPENDIX J

COMPARISON BETWEEN EXPERIMENTAL AND PREDICTED RESPONSE TO IMBALANCE FOR IMBALANCE TEST A2 AND B2

In-phase	Imbalance displacement
Experiments	u = 9.5 μm
Predictions	u = 9.5 μm

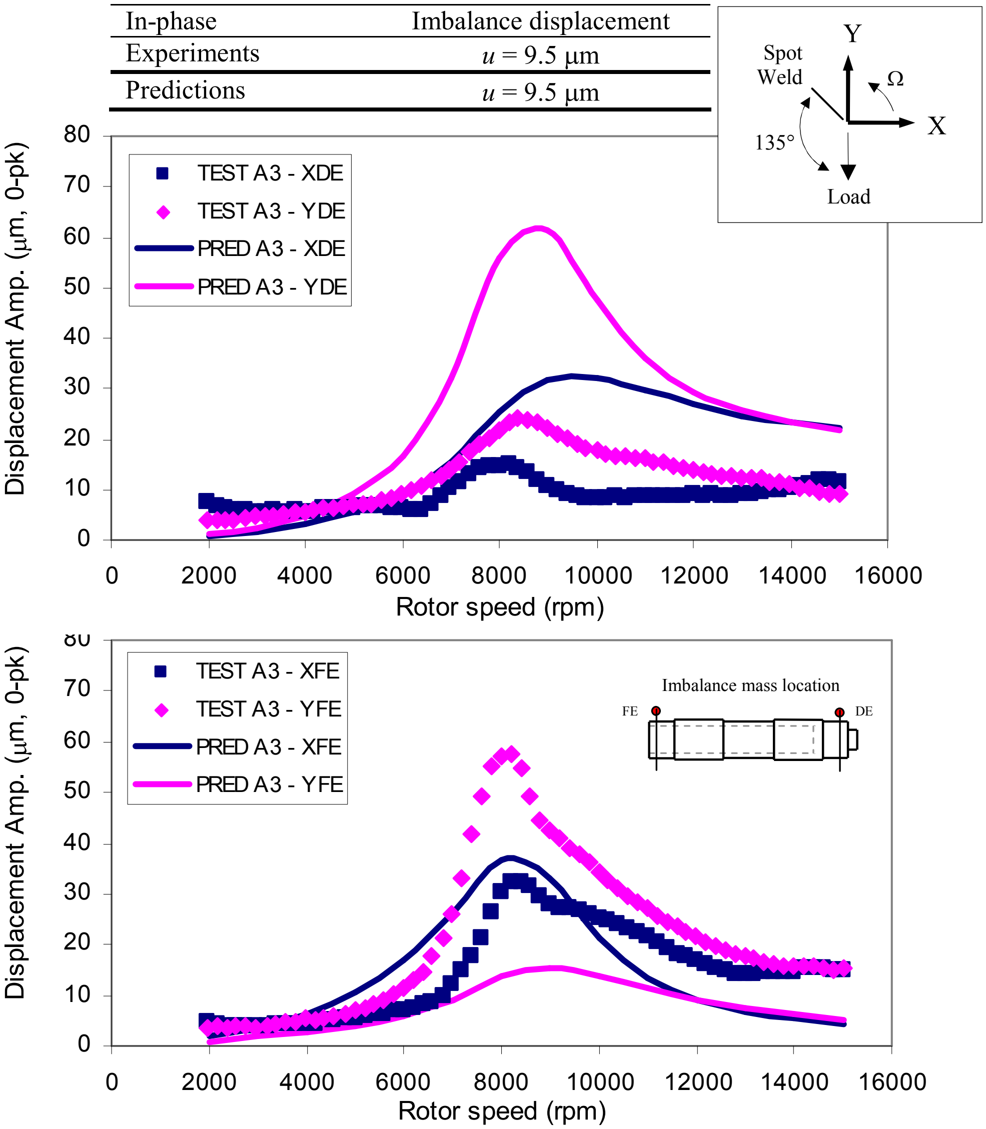

Figure J1 Predicted and experimental response to imbalance at the drive end and free end location for an imbalance of u = 9.5 μm (in phase, test A2)

Out-of-phase	Imbalance displacement
Experiments	u = 5.2 μm
Predictions	u = 5.2 μm

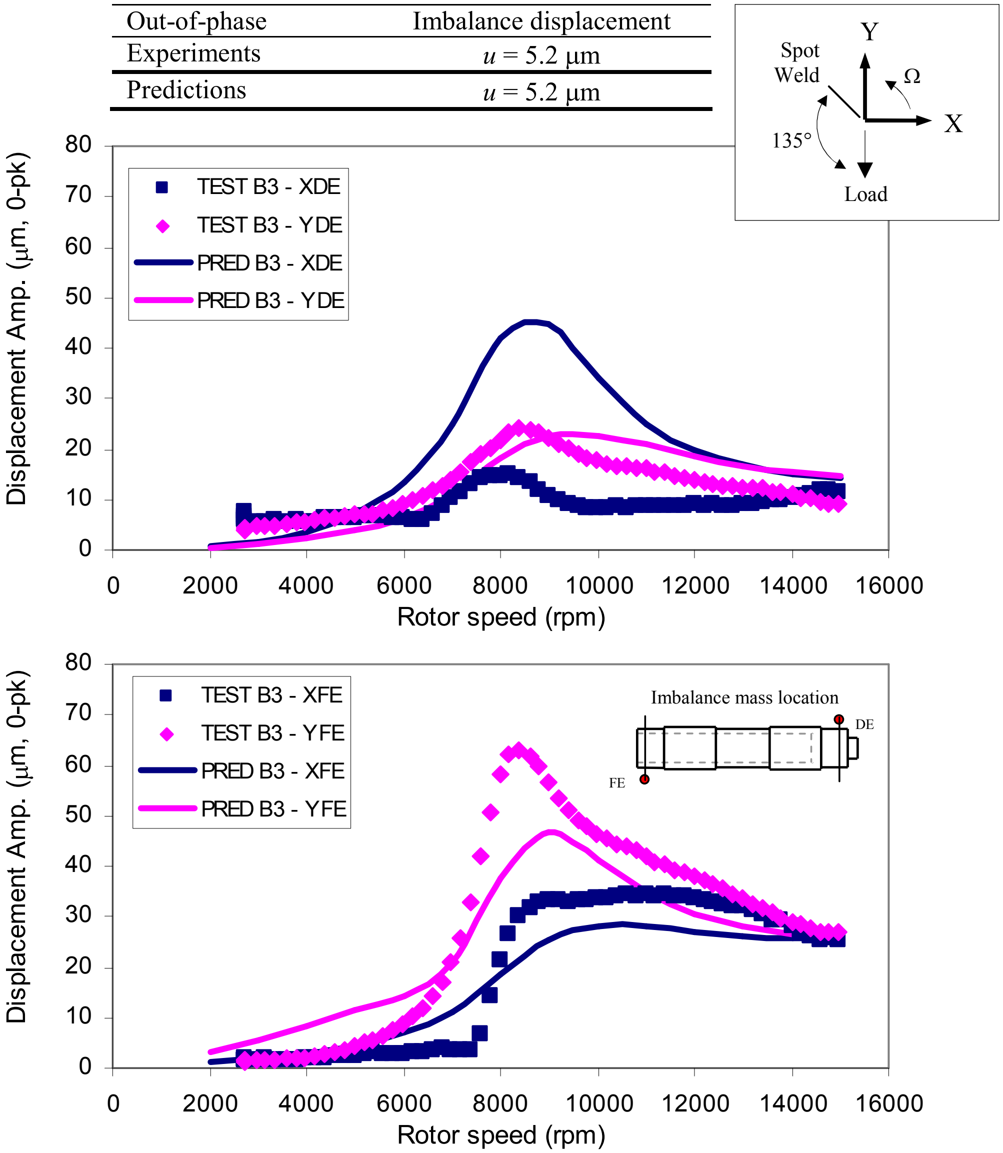

Figure J2 Predicted and experimental response to imbalance at the drive end and free end location for an imbalance of u = 5.2 μm (out-of-phase, test B2)

VITA

Name: Dario Rubio Tabares

Address: Department of Mechanical Engineering, 3123, TAMU, College Station, Texas, USA.

Email: dariorubio10@hotmail.com

Education: B.S., Mechanical Engineering, Universidad Simon Bolivar, Venezuela, 2003
M.S., Mechanical Engineering, Texas A&M University,
USA, 2005